TECHNISCHE UNIVERSITÄT WIEN
Vienna University of Technology

Spin-motion coupling of nanofiber-trapped atoms and its applications

DISSERTATION

zur Erlangung des akademischen Grades

Doktor der Naturwissenschaften

eingereicht von

Yijian Meng
Matrikelnummer 1528759
Wendenschloßstraße 137, Berlin

an der
Fakultät für Physik der Technischen Universität Wien

Betreuung: Prof. Dr. Arno Rauschenbeutel, HU Berlin

Diese Dissertation haben begutachtet:

(Prof. Dr. Christian Kurtsiefer) (Prof. Dr. Kali Prasanna Nayak)

Wien, 18.12.2020

(Yijian Meng)

Die approbierte gedruckte Originalversion dieser Dissertation ist an der TU Wien Bibliothek verfügbar.
The approved original version of this doctoral thesis is available in print at TU Wien Bibliothek.
TU Bibliothek Your knowledge hub WIEN

Die approbierte gedruckte Originalversion dieser Dissertation ist an der TU Wien Bibliothek verfügbar.
The approved original version of this doctoral thesis is available in print at TU Wien Bibliothek.

TECHNISCHE UNIVERSITÄT WIEN
Vienna University of Technology

Spin-motion coupling of nanofiber-trapped atoms and its applications

DISSERTATION

submitted in partial fulfillment of the requirements for the degree of

Doktor der Naturwissenschaften

by

Yijian Meng
Registration Number 1528759
Wendenschloßstraße 137, Berlin

to the Faculty of Physics
at the Vienna University of Technology

Advisor: Prof. Dr. Arno Rauschenbeutel, HU Berlin

The dissertation has been reviewed by:

(Prof. Dr. Christian Kurtsiefer)

(Prof. Dr. Kali Prasanna Nayak)

Wien, 18.12.2020

(Yijian Meng)

Die approbierte gedruckte Originalversion dieser Dissertation ist an der TU Wien Bibliothek verfügbar.
The approved original version of this doctoral thesis is available in print at TU Wien Bibliothek.
TU Bibliothek Your knowledge hub WIEN

Die approbierte gedruckte Originalversion dieser Dissertation ist an der TU Wien Bibliothek verfügbar.
The approved original version of this doctoral thesis is available in print at TU Wien Bibliothek.

Abstract

Cold atom-nanophotonic systems constitute a powerful research platform for the exploration of new regimes of light-matter interaction. The guided light in nanophotonic systems are tightly confined, and often used to trap and manipulate cold atoms at subwavelength distance away from the surface. While the initialization of atomic internal degrees of freedom in these systems has been achieved, a full control of the atomic quantum state also requires manipulating and preparing the atomic motional state at the quantum level.

In this thesis, we explore and characterize the coupling between motional and spin degrees of freedom in nanofiber-trapped atoms. This coupling originates from the strong polarization gradient which occurs naturally in spatially confined light fields, i.e., the guided light field in a nanophotonic system. We demonstrate that the spin-motion coupling can be utilized to implement degenerate Raman cooling and prepare atoms close to the three-dimensional motional ground state. We obtain mean numbers of motional quanta of nanofiber-trapped atoms using heterodyne fluorescence spectroscopy. Building on this work, we then use the spin-motion coupling for nanofiber-trapped atoms to realize a mechanical analogue of the Dicke model. We infer the energy spectrum of the system from transitions observed in the fluorescence spectrum. We show that our system reaches the ultrastrong coupling regime. Moreover, we demonstrate that the coupling strength can be readily tuned using an additional nanofiber-guided light field.

Furthermore, we achieve imaging of single nanofiber-trapped atoms. Taking advantage of degenerate Raman cooling, we cool atoms near the motional ground state while collecting atom-scattered light using a camera. We show single atoms can be detected by imaging at an integration time far less than the trapping lifetime. To demonstrate the potential of this technique, we perform two proof of principle experiments. First, we measure the extinction of a nanofiber-guided light atom by atom, and verify the Beer-Lambert Law in the few atoms regime. Second, we detect the atom-scattered light that is coupled to the nanofiber. We observe interference of scattered light fields as a function of the distance between two trapped atoms.

By controlling atomic motional states and imaging single atoms, our work in this thesis adds to the toolbox for manipulating and detecting cold atoms interfaced to nanophotonic systems, and paves the way for realizing the bottom-up approach to explore new regimes of light-matter interaction atom by atom.

Die approbierte gedruckte Originalversion dieser Dissertation ist an der TU Wien Bibliothek verfügbar.
The approved original version of this doctoral thesis is available in print at TU Wien Bibliothek.
TU Bibliothek Your knowledge hub WIEN

Die approbierte gedruckte Originalversion dieser Dissertation ist an der TU Wien Bibliothek verfügbar.
The approved original version of this doctoral thesis is available in print at TU Wien Bibliothek.

List of Publications

In the process of working on this thesis, the following articles have been published in peer-reviewed journals or will be published soon:

- Y. Meng, C. Liedl, S.Pucher, A. Rauschenbeutel, and P. Schneeweiss.
  Imaging and localizing individual atoms interfaced with a nanophotonic waveguide
  Phys. Rev. Lett., 125(5): 053603, 2020.

- J. Wilson, S. Saskins , Y. Meng, S. Ma, A. Burger, and J. Thompson
  Trapped arrays of alkaline earth Rydberg atoms in optical tweezers
  arXiv.org, arXiv:1912.08754, 2020.

- A. Dareau, Y. Meng, P. Schneeweiss, and A. Rauschenbeutel.
  Observation of ultrastrong spin-motion coupling for cold atoms in optical microtraps
  Phys. Rev. Lett., 121(25):253603, 2018.

- Y. Meng, A. Dareau, P. Schneeweiss, and A. Rauschenbeutel.
  Near-ground-state cooling of atoms optically trapped 300 nm away from a hot surface
  Phys. Rev. X, 8(3):031054, 2018.

- B. Albrecht, Y. Meng, C. Clausen, A. Dareau, P. Schneeweiss, and A. Rauschenbeutel.
  Fictitious magnetic-field gradients in optical microtraps as an experimental tool for interrogating and manipulating cold atoms
  Phys. Rev. A., 94(6):061401, 2016.

Die approbierte gedruckte Originalversion dieser Dissertation ist an der TU Wien Bibliothek verfügbar.
The approved original version of this doctoral thesis is available in print at TU Wien Bibliothek.
TU Bibliothek Your knowledge hub WIEN

Die approbierte gedruckte Originalversion dieser Dissertation ist an der TU Wien Bibliothek verfügbar.
The approved original version of this doctoral thesis is available in print at TU Wien Bibliothek.

Contents

1 Introduction **1**

2 Optical nanofiber based light-atom interface **5**
2.1 Experimental setting for nanofiber-based optical dipole trap 6
2.2 Nanofiber-guided mode 7
2.3 Interaction between atoms and nanofiber-guided light 10
2.4 Nanofiber-based two-color trapping potential 12
2.5 Measuring the optical density of nanofiber-trapped atoms via transmission spectroscopy 13

3 Spin-motion coupling of nanofiber-trapped atoms **17**
3.1 Fictitious magnetic field 17
3.2 Origin of spin-motion coupling for nanofiber-trapped atoms 18

4 Introduction to fluorescence spectroscopy **23**
4.1 Overview 23
4.2 Rate equation approach 24
4.3 Fluorescence spectrum of nanofiber-trapped atoms 27
4.4 Master equation approach 28
4.5 Heterodyne fluorescence spectroscopy 32

5 Ground state cooling of atoms 300 nm away from a nanofiber **35**
5.1 Principle of degenerate Raman cooling 36
5.2 Experimental procedure 38
5.3 Trapping lifetime during degenerate Raman cooling 38
5.4 Optimization of degenerate Raman cooling based on minimizing atom loss . . 40
5.5 Heterodyne fluorescence spectroscopy during degenerate Raman cooling 42
5.6 Discerning and preparing atoms on only one side of the nanofiber 46
5.7 Summary and outlook 49

6 Ultra-strong spin-motion coupling of nanofiber-trapped atoms **51**
6.1 Simulating quantum Rabi model and Dicke model with nanofiber-trapped atoms 52
6.2 Fluorescence spectroscopy and 2D spectrum 54
6.3 Tuning the coupling strength 56

Die approbierte gedruckte Originalversion dieser Dissertation ist an der TU Wien Bibliothek verfügbar.
The approved original version of this doctoral thesis is available in print at TU Wien Bibliothek.
TU Bibliothek Your knowledge hub WIEN

6.4 Exploration of the USC regime at higher coupling strengths 58
6.5 Summary and outlook 61

7 Imaging of individual nanofiber-trapped atoms **63**
7.1 Experimental method 64
7.2 Raw atom images using an external or nanofiber-guided excitation light field . . 65
7.3 Atom detection scheme 68
7.3.1 Modeling photon count histogram and false atom detection probability in the presence of atom loss 71
7.3.2 Atom detection probability as a function of detection threshold 76
7.3.3 Determine atom positions with sub-pixel resolution 78
7.3.4 Atom detection error due to nearby atoms 79
7.3.5 Position dependence of single-atom signal 80
7.4 Resonant transmission through nanofiber-coupled atoms 82
7.5 Scattering of light by atoms into the nanofiber-guided mode 85
7.6 Summary and outlook 91

8 Conclusion & Outlook **93**

9 Appendix **95**
9.1 Heating mechanisms of nanofiber-trapped atoms 95
9.1.1 Off-resonant scattering of the trapping laser fields by the atoms 95
9.1.2 Raman scattering in the fiber 96
9.1.3 Blackbody radiation and Johnson–Nyquist noise 96
9.1.4 Mechanical modes of the nanofiber and their coupling to guided light fields 96
9.1.5 Brillouin scattering in the fiber 100

Bibliography **103**

Die approbierte gedruckte Originalversion dieser Dissertation ist an der TU Wien Bibliothek verfügbar.
The approved original version of this doctoral thesis is available in print at TU Wien Bibliothek.
TU Bibliothek Your knowledge hub WIEN

Die approbierte gedruckte Originalversion dieser Dissertation ist an der TU Wien Bibliothek verfügbar.
The approved original version of this doctoral thesis is available in print at TU Wien Bibliothek.

CHAPTER 1

Introduction

In the past few decades, the field of cold atoms has undergone a tremendous development that enables unprecedented control over complex quantum systems [1–7]. Almost in parallel, the field of nanophotonics, i.e., the study of the behavior of light on the nanometer scale and the interaction between light and nanometer-scale objects, has benefited from the increasing industrial and research capabilities to provide evermore control of light fields at the subwavelength level [8–10]. Nanophotonics-based cold atom systems represent a natural marriage between these two fields [11–16], and constitutes as a promising platform for engineering strong light-matter coupling and realizing potentially scalable systems for quantum information processing [17–20]. Such systems utilize the unique properties of light in nanophotonic devices to interact with localized atoms on the quantum level. In particular, by engineering the nanophotonic mode structure, e.g., by introducing bandgaps or reducing the mode volume, the interaction between the atoms and the mode can be modified and enhanced [21].

Nanophotonics-based cold atom systems have flourished in the last decade, and one of the primary examples is the nanofiber-based atom trap. The nanofiber-based atom trap was proposed in the works by Fam [22], and was first experimentally demonstrated in our group [11]. Here, atoms are interfaced using the evanescent field of the nanofiber-guided light. The atoms can be trapped $\sim$300 nm away from the fiber surface. The nanofiber-interfaced atoms form two one-dimensional arrays parallel to the nanofiber. The coupling of individual atoms and the nanofiber-guided light is largely constant at different trap positions on the fiber, thereby thousands of atoms can be homogeneously coupled to the nanofiber-guided light. The coherence properties of the trapped atoms have been investigated using Ramsey spectroscopy. The ground state coherence time of the trapped atoms can reach on the order of milliseconds [23]. The nanofiber is realized as the waist of a tapered optical fiber. The guided light fields in a standard optical fiber can be efficiently coupled into and out of the nanofiber section.

The nanofiber-guided light is strongly confined in the transverse direction, resulting in an efficient coupling between trapped atoms and the nanofiber-guided light, i.e., an optical density on the order of 10 can be realized with just a few hundred atoms. Another consequence of this confinement is the direction-dependent polarization of the nanofiber-guided field. Taking

advantage of this property, chiral coupling between light and nanofiber-guided modes has been observed [24, 25]. As an application, the chiral coupling has been used to realize an optical diode [26].

The nanofiber-based light-atom interface can enable observation of collective phenomena. The heralded creation of a single collective spin excitation of atom arrays coupled to a nanofiber has been demonstrated [27]. Furthermore, under the Bragg condition, nanofiber-trapped atoms can be used as an atomic mirror for a fiber-guided light [28–30]. Moreover, if an external light field fulfills the Bragg condition, the nanofiber-trapped atoms can be used to efficiently scatter light into the nanofiber-guided mode.

In recent years, there have been increasing interests to control nanofiber-guided atom's motional states. Besides the fundamental interest to gain access to the atom's full quantum state, understanding and manipulating the atomic motional state can add extra degrees of freedom for certain quantum protocols. The heating rate in the nanofiber-based trap has typically been exceeding those in comparable free-space optical microtraps by $\sim$3 orders of magnitude. Due to the excessive heating, the trapping lifetime is only $\sim 50\,\mathrm{ms}$, far shorter than the limit imposed by the collision rate with the background gas. Both the high heating rate and short lifetime are roadblocks for the implementation of certain protocols and devices. In particular, the thermal motion of atoms in the trapping potential leads to fluctuation of the coupling strength between the atoms and the nanofiber-guided light. The inhomogeneity of the atom-waveguide coupling is detrimental to the performance of experiments which utilize the collective excitation of atoms, e.g., atomic Bragg mirrors, quantum memories [28, 29, 31, 32]. In this thesis, we will address this problem by preparing atoms close to the motional ground state using degenerate Raman cooling. Our cooling scheme relies on the coupling between motion and spin degrees of freedom of the trapped atoms, which arises from the properties of the nanofiber-guided trapping light fields. This coupling enables control of the atom's motional states through manipulation of its spin states. We utilize fluorescence spectroscopy to measure the atomic temperature in three motional degrees of freedom.

In addition, we show that the Hamiltonian describing the spin-motion coupling in nanofiber-trapped atoms matches that of the Dicke model. In particular, the bosonic mode in the Dicke model is represented by the motional states of the trapped atoms. We show that the eigenenergy of the Hamiltonian can be read out using fluorescence spectroscopy, and the corresponding parameters in the Dicke model are readily tunable in the ultrastrong coupling regime.

Finally, we demonstrate imaging of single trapped atoms by collecting the atom-scattered light in the degenerate Raman cooling scheme. Atom imaging is an enabling technique in cold-atom systems that allows the possibility of postselection and possible feedback schemes. Compared to free space atom traps, imaging atoms interfaced to a nanophotonic device presents different challenges, e.g., high background signal due to scattering of the excitation light by the nearby nanophotonic structure. Hence, until now imaging of single atoms has been elusive for such systems. The degenerate Raman cooling scheme extends the trapping lifetime of atoms and thereby allows us to perform imaging of single atoms with a sufficient signal to noise ratio. To demonstrate the versatility enabled by imaging single atoms in the nanofiber-based trap, we carry out two proof-of-principle experiments: First, we measure the extinction of a nanofiber-guided probe light as a function of number of atoms detected by imaging. In this measurement, we test

Die approbierte gedruckte Originalversion dieser Dissertation ist an der TU Wien Bibliothek verfügbar.
The approved original version of this doctoral thesis is available in print at TU Wien Bibliothek.
TU Bibliothek Your knowledge hub WIEN

the Beer-Lambert's law in the few-atoms regime. Second, we study the scattering of light by atoms into the nanofiber-guided mode. Conditioned on the imaging detection of two atoms, we observe the interference of atom-scattered light fields as a function of the inter-atomic distance determined by atom images.

The thesis is structured in the following way: In chapter 2, the nanofiber-based atom-light interface will be introduced. The properties of the nanofiber-guided mode will be described, in particular, the intensity and polarization pattern of its evanescent field. In addition, the trapping potential formed by nanofiber-guided light will be introduced. In chapter 3, we will introduce the fictitious magnetic field and show how it enables the coupling of the spin and motional degrees of freedom. In chapter 4, fluorescence spectroscopy of trapped cold atoms will be introduced. We will show how this technique can be implemented in the nanofiber-atom interface and how it enables the detection of atomic motional states. In chapter 5, we will describe the cooling of nanofiber-trapped atoms close to the motional ground state using a degenerate Raman cooling scheme. We will characterize the cooling efficiency using fluorescence spectroscopy and trapping lifetime measurements. In chapter 6, we will show that the spin-motion coupling for nanofiber-guided atoms can be used to simulate the Dicke model in the ultrastrong coupling regime. We will demonstrate that the coupling strength can be read out through fluorescence spectroscopy. In chapter 7, we will demonstrate imaging of single trapped atoms. We will characterize the atom detection efficiency based on imaging. Finally, we will demonstrate two textbook-like experiments: one tests Beer-Lambert's law in the few-atoms regime, and one studies the interference between two atom-scattered light fields as a function of the inter-atomic distance.

Die approbierte gedruckte Originalversion dieser Dissertation ist an der TU Wien Bibliothek verfügbar.
The approved original version of this doctoral thesis is available in print at TU Wien Bibliothek.
TU Bibliothek Your knowledge hub WIEN

Die approbierte gedruckte Originalversion dieser Dissertation ist an der TU Wien Bibliothek verfügbar.
The approved original version of this doctoral thesis is available in print at TU Wien Bibliothek.

Die approbierte gedruckte Originalversion dieser Dissertation ist an der TU Wien Bibliothek verfügbar.
The approved original version of this doctoral thesis is available in print at TU Wien Bibliothek.

CHAPTER 2

Optical nanofiber based light-atom interface

The invention of optical fibers has revolutionized communication on a global scale [33]. Information can be encoded into pulses of light and transmitted through optical fibers across the globe. Most common optical fibers are made from silica glass, and are consist essentially of a cylindrical core surrounded by a cladding layer with a lower refractive index. Due to the change in the refractive index at the boundary between core and cladding, the fiber-guided light propagates along the path defined by the fiber via total internal reflection in the fiber core. For a high-quality single-mode fiber, the loss rate can be as low as 0.2 dB per kilometer in the $1550\,\mathrm{nm}$ wavelength region [34].

In contrast to a conventional optical fiber, a nanofiber has a core diameter of less than a micrometer. In addition, a nanofiber has no cladding layer, and the nanofiber-guided light is directly exposed to the environment. For the light fields involved in our experiment, their wavelengths are comparable to the typical diameter of a nanofiber, thereby a large portion of the nanofiber-guided light's intensity is in the evanescent component. Using a red-detuned light field and a blue-detuned light field that are nanofiber-guided, trapping of atoms near a nanofiber can be realized.

The nanofiber-guided light is continuously focused while propagating in the nanofiber section, which typically has a length on the order of $1\,\mathrm{cm}$. In conjunction with the tight confinement and low transmission loss, nanofiber-guided light can be used to interact homogeneously and efficiently with an ensemble of trapped atoms.

In this chapter, we describe the experimental setup for the nanofiber-based light-matter interface. In particular, we discuss the properties of the nanofiber-guided mode, i.e., its polarization and intensity pattern. Moreover, we describe the interaction between a far-detuned nanofiber-guided light field and a cesium atom in the electronic ground state. We show how trapping potential can be formed using the configuration of two-color guided light fields. Furthermore, We explain a nanofiber-based transmission measurement which is routinely used for probing and monitoring the trapped atom's optical density.

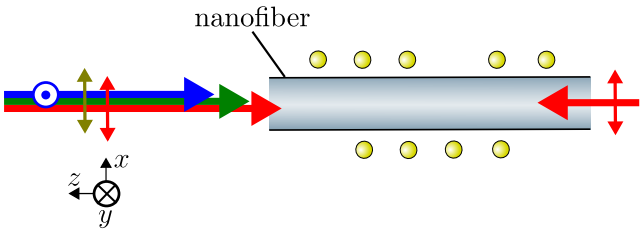

Figure 2.1: Illustration of a nanofiber-based atom trap. The blue arrow represents the blue-detuned light field at 783 nm which is quasi-linearly polarized along the y-axis. The red arrows represent the red-detuned light fields at 1064 nm which are quasi-linearly polarized along the x-axis. The two counter-propagating red-detuned light fields form a standing wave, resulting in two lattices of trapping potentials at two sides of the nanofiber. The trapped atoms are depicted by yellow circles.

2.1 Experimental setting for nanofiber-based optical dipole trap

To interface atoms with nanofiber-guided light at a constant coupling strength, atoms need to be spatially confined near the nanofiber. For this purpose, we utilize the nanofiber-guided light's evanescent fields to trap atoms at a sub-wavelength distance away from the nanofiber surface. The trapping light consist of two components: A red-detuned standing light field and a blue-detuned running light field. We choose trapping light fields that are far detuned, i.e., of a frequency that is more than $\sim$30 THz away from the D_1 and D_2 transitions of a neutral cesium atom. Hence, the occupation of the electronic excited state is negligible. For the experiments shown in chapters 5 and 6, the wavelengths of the red and blue-detuned light fields are 1064 nm and 783 nm, respectively. The blue- and red-detuned trapping light fields have mutually orthogonal quasi-linear polarizations. They form two diametric one-dimensional lattices of trapping potentials along the nanofiber, see Fig. 2.1. We describe the expected trapping potential in section 2.2.

The nanofiber is realized as a waist region of an adiabatically-tapered optical fiber. The nanofiber was produced in a heat-and-pull process [35]. The final diameter of the fiber waist is $\sim$500 nm and the single-mode transmission is $\sim$ 97% for the wavelengths of 1064 nm and 783 nm used for trapping [11]. To minimize the loss of trapped atoms due to collision with the background gas, we place the nanofiber in a high vacuum environment, i.e., a vacuum chamber evacuated by a turbo-molecular pump and an ion getter pump. The pressure inside the vacuum chamber is kept at $\sim 3 \times 10^{-9}$ mbar [24], corresponding to a collision-limited trapping lifetime of $\sim$1 s. The nanofiber-guided light fields enter the vacuum chamber through a Teflon feed-through. We apply an electric current between 3 A and 7 A to a cesium dispenser to heat out cesium atoms into the vacuum chamber.

We first prepare a cold atom cloud in the vicinity of the nanofiber using a magnetic optical trap (MOT). The magnetic field for the MOT is in the anti-Helmholtz configuration and is provided by two main coils, one placed above and one below the vacuum chamber. The vacuum chamber is made from stainless steel and does not shield the experiment from stray magnetic

Die approbierte gedruckte Originalversion dieser Dissertation ist an der TU Wien Bibliothek verfügbar.
The approved original version of this doctoral thesis is available in print at TU Wien Bibliothek.
TU Bibliothek Your knowledge hub WIEN

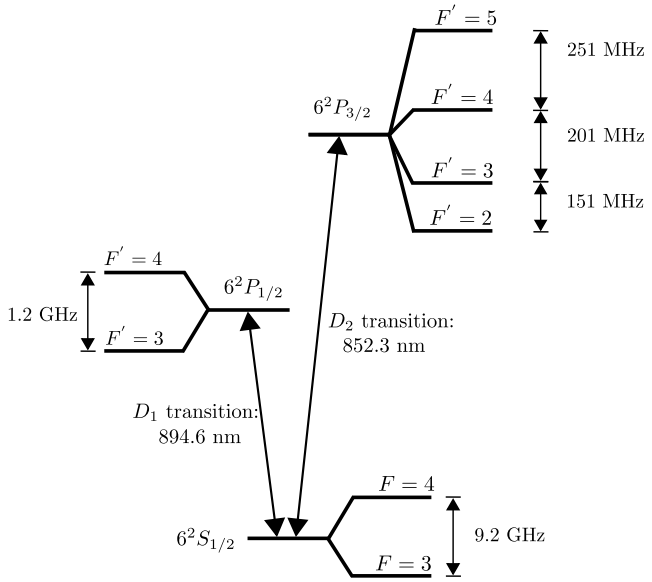

Figure 2.2: Energy level diagram for a cesium atom. The two main transitions are D_1 ($6^2S_{1/2} \rightarrow 6^2P_{1/2}$) and D_2 ($6^2S_{1/2} \rightarrow 6^2P_{3/2}$). The splitting between the two hyperfine states $F = 4$ and $F = 3$ of the $6^2S_{1/2}$ electronic ground state is $9.2\,\mathrm{GHz}$.

fields and Earth's magnetic field. Moreover, stainless steel might even be the source of a stray magnetic field. We use two additional pairs of magnetic coils to compensate magnetic fields orthogonal to the one generated by the main coil pair. The atoms are cooled by three pairs of counter-propagating light fields red-detuned to the D_2-cycling transition of the cesium atom. We denote these light fields as the cooling light in this section. We use a pair of D_2 light on the $F = 3$ to $F' = 4$ hyperfine transition to pump atoms out of the $F = 3$ hyperfine state which is a dark state for the cooling light. The cesium D_2 transition hyperfine structure is shown in Fig. 2.2. During the MOT stage, the cesium atoms in the vacuum chamber form a cold atom cloud near the nanofiber. In the experiments described in this thesis, the MOT stage lasts between $1\,\mathrm{s}$ and $2\,\mathrm{s}$. In order to load atoms into the nanofiber-based optical trap, we perform polarization gradient cooling and to further reduce atoms' motional energy. For polarization gradient cooling, we ramp down the magnetic field to $0\,\mathrm{G}$ and gradually sweep the frequency of the cooling light further away from the atomic resonance. Once the atom's kinetic energy is less than the depth of the trapping potential, atoms are gradually loaded into the nanofiber-based optical traps. Due to the collisional blockage effect, each trapping site contains at most one atom and the filling factor of all trapping sites is lower than 0.5.

2.2 Nanofiber-guided mode

For the experiments described in this thesis, we use a nanofiber with a diameter of $500\,\mathrm{nm}$. As the nanofiber is mounted in a high vacuum environment, the refractive index drops to 1 at

Die approbierte gedruckte Originalversion dieser Dissertation ist an der TU Wien Bibliothek verfügbar.
The approved original version of this doctoral thesis is available in print at TU Wien Bibliothek.
TU Bibliothek Your knowledge hub WIEN

the glass-vacuum boundary of the waveguide. The wave equation for the electric field in this configuration can be derived from Maxwell's equation. The detailed derivation of the nanofiber-guided mode can be found in the literature [36, 37]. For the nanofiber in our experimental setup, only the fundamental HE_{11} mode is guided at wavelengths between $780\,\mathrm{nm}$ and $1064\,\mathrm{nm}$.

A simple expression of the mode profile function can be found for quasi-circularly polarized guided light. Here we provide the expression for the evanescent field part of the electric field mode, i.e., when the radial distance r from the center of the nanofiber is larger than the nanofiber's radius a:

$$\begin{aligned} e_r &= i\left[(1-s)K_0(qr) + (1+s)K_2(qr)\right], \\ e_\varphi &= -\left[(1-s)K_0(qr) - (1+s)K_2(qr)\right], \\ e_z &= \frac{2q}{\beta}K_1(qr), \end{aligned} \tag{2.1}$$

where K_0, K_1, and K_2 are modified Bessel functions of the second kind, β is the longitudinal propagation constant of the nanofiber-guided mode, and s is defined as:

$$s = \left(\frac{1}{h^2a^2} + \frac{1}{q^2a^2}\right)\left(\frac{J_1'(ha)}{haJ_1(ha)} + \frac{K_1'(qa)}{qaK_1(qa)}\right)^{-1}, \tag{2.2}$$

where J_1 is a Bessel function of the first kind, and h and q are defined as:

$$h = (n_1^2k^2 - \beta^2)^{1/2}, \tag{2.3}$$

$$q = (\beta^2 - n_2^2k^2)^{1/2}. \tag{2.4}$$

The parameter h depends on the refractive index of the core, n_1, and q depends on the refractive index of outside the nanofiber which is vacuum, i.e., $n_2 = 1$. We show the effective refractive indices for the nanofiber-guided light in Fig. 2.3.

Now we show the solution for a nanofiber-guided light that is quasi-linearly polarized along the y-axis. The solution equals to the superposition of two quasi-circularly polarized light fields of opposite rotation. For convenience, the electric field is expressed in the Cartesian components whereas its position is written in the cylindrical coordinate:

$$\begin{aligned} \boldsymbol{E_1} = A_1[&\hat{\boldsymbol{e}}_{\boldsymbol{x}}(e_r + ie_\varphi)\sin(\varphi)\cos(\varphi) + \hat{\boldsymbol{e}}_{\boldsymbol{y}}(e_r\sin^2(\varphi) - ie_\varphi\cos^2(\varphi)) \\ &+ \hat{\boldsymbol{e}}_{\boldsymbol{z}}e_z\sin\varphi]e^{i(\beta z - \omega t)} + c.c., \end{aligned} \tag{2.5}$$

where φ is the azimuthal angle with respect to the x-axis (see Fig. 2.4(a)), A_1 is the electric field amplitude, $\hat{\boldsymbol{e}}_{\boldsymbol{x}}$, $\hat{\boldsymbol{e}}_{\boldsymbol{y}}$, and $\hat{\boldsymbol{e}}_{\boldsymbol{z}}$ are unit vectors in the direction along the x, y, and z axes, respectively.

In Fig. 2.4, we show the intensity distribution of the evanescent part of a nanofiber-guided light that is quasi-linearly polarized. The nanofiber orients along the z-axis and the light has a main direction of polarization along the y-axis. We show in panel (a) the cross-section of

Die approbierte gedruckte Originalversion dieser Dissertation ist an der TU Wien Bibliothek verfügbar.
The approved original version of this doctoral thesis is available in print at TU Wien Bibliothek.

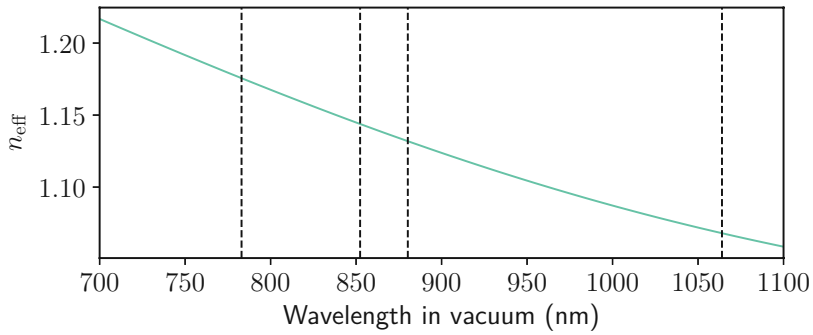

	783 nm ('blue')	852.35 nm (D2)	880.25 nm	1064 nm ('red')
n_{eff}	1.453617	1.452462	1.45204	1.449631

Figure 2.3: Effective refractive index for the nanofiber-guided light, n_{eff}, as a function of wavelength in vacuum.

the intensity distribution in the xy-plane. Due to the quasi-linear polarization, the intensity distribution breaks the rotation symmetry and the intensity is stronger along the polarization axis. We plot the intensity of the evanescent field at $1\,\text{nm}$ from the nanofiber surface in panel (b). The highest intensity occurs along the polarization axis or $\varphi = 90°$, which is 4.8 times compared to the minimum at $\varphi = 0°$. For this calculation, we use a nanofiber diameter of $500\,\text{nm}$, a nanofiber-guided light with wavelength of $783\,\text{nm}$ and power of $1\,\text{mW}$.

The nanofiber-guided light has a longitudinal component that is $\frac{\pi}{2}$ out of phase with respect to the transverse component. As a result, the electric field of the evanescent field has a large component of circular polarization, see Fig. 2.5. The photon associated with this circular polarization has a transverse spin angular momentum, i.e., the direction of the spin angular momentum is perpendicular to the propagation direction. This is a direct consequence of the tight confinement of nanofiber-guided light in the transverse direction. The green arrow in Fig. 2.5 represents a nanofiber-guided light field that is quasi-linearly polarized along the x-axis. Since the gradient of the electric field has opposite signs at the two sides of the nanofiber, a quasi-linearly polarized nanofiber-guided light has opposite transverse circular polarization at the two sides of the nanofiber.

In addition, the electric field of two counter-propagating light waves that are both quasi-linearly polarized along the x-axis is the following:

$$\begin{aligned}\boldsymbol{E_2} = A_2\{&[\hat{\boldsymbol{e}}_{\boldsymbol{x}}(e_r\cos^2(\varphi) - ie_r\sin^2(\varphi)) + \hat{\boldsymbol{e}}_{\boldsymbol{y}}(e_r + ie_\varphi)\sin(\varphi)\cos(\varphi)]\cos(\beta z)\\ &+ i\hat{\boldsymbol{e}}_{\boldsymbol{z}}e_z\cos(\varphi)\sin(\beta z)\}e^{-i\omega t} + c.c..\end{aligned} \tag{2.6}$$

The two counter-propagating light fields form a standing wave. The longitudinal component goes to zeros at nodes $\beta z = \pi m$, where m is an integer.

Die approbierte gedruckte Originalversion dieser Dissertation ist an der TU Wien Bibliothek verfügbar.
The approved original version of this doctoral thesis is available in print at TU Wien Bibliothek.
TU Bibliothek Your knowledge hub WIEN

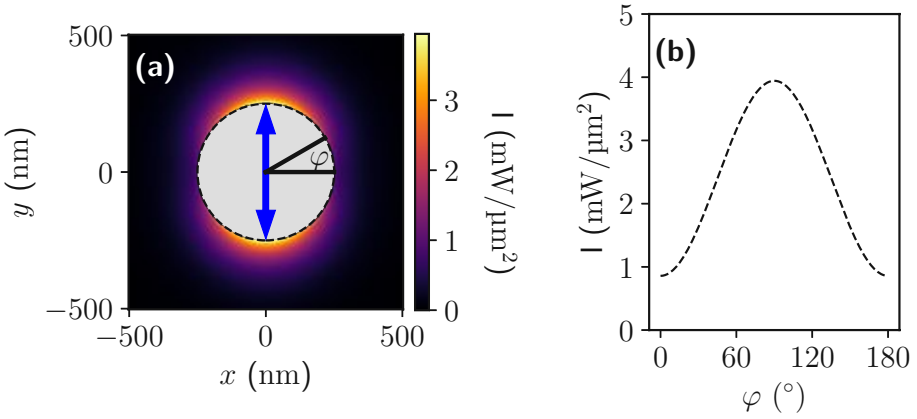

Figure 2.4: Intensity distribution in the evanescent field of a nanofiber-guided light field that is quasi-linearly polarized along the y-axis. (a) Intensity distribution in the xy-plane. The power of this light field is $1\,\mathrm{mW}$, and it has a wavelength of $783\,\mathrm{nm}$. (b) Intensity of the evanescent field at $1\,\mathrm{nm}$ away from the nanofiber surface. We indicate the corresponding positions in panel (a) by the dashed circular line.

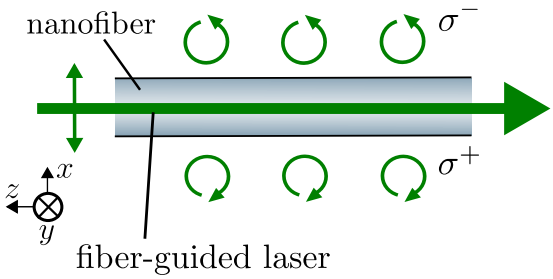

Figure 2.5: A nanofiber-guided light field that is quasi-linearly polarized along the x-axis. The evanescent field exhibits large component of σ^- (σ^+) polarization at the position with $x > 0$ ($x < 0$), i.e., above (below) the nanofiber in the illustration. Therefore, the field carries spin angular momentum which has a transverse component. The direction of the transverse spin is orthogonal to the propagation direction of the light. This is a feature originating from the tight transverse confinement of the nanofiber-guided light.

2.3 Interaction between atoms and nanofiber-guided light

For light that is far detuned compared to the cesium hyperfine splitting, its interaction with a cesium atom in the electronic ground state can be described by the light-shift operator:

$$\hat{V}_{A_L} = -\frac{1}{4}\alpha_s(\omega)\,|\boldsymbol{E}|^2 + i\frac{1}{8F}\alpha_v(\omega)(\boldsymbol{E}^* \times \boldsymbol{E})\cdot\hat{\boldsymbol{F}}, \tag{2.7}$$

Die approbierte gedruckte Originalversion dieser Dissertation ist an der TU Wien Bibliothek verfügbar.
The approved original version of this doctoral thesis is available in print at TU Wien Bibliothek.
TU Bibliothek Your knowledge hub WIEN

where F is the quantum number of the total angular momentum $\hat{\boldsymbol{F}}$, α_s is the scalar component of polarizability, and α_v is the vector component of polarizability.

The first term in equation 2.7 describes the scalar light shift which is proportional to the intensity of the light field. The second term describes the vector light shift which depends additionally on the polarization of the electric field, i.e., it is zero (maximum) when the electric field is linearly (circularly) polarized. The vector light shift dependents on atom's m_F substates. For our experimental setting, the light shift is on the order of kHz or MHz, which is small compared to the hyperfine structure splitting of 9 GHz for $6^2S_{1/2}$. Therefore, F is a good quantum number, and in this case, the scalar and vector component of the polarizabilities are given by:

$$\alpha_s = \frac{1}{\sqrt{3(2J+1)}}\alpha_{nJ}^{(0)} \tag{2.8}$$

$$\alpha_v = -(-1)^{J+I+F}\sqrt{\frac{2F(2F+1)}{(F+1)}}\begin{Bmatrix} F & 1 & F \\ J & I & J \end{Bmatrix}\alpha_{nJ}^{(1)}, \tag{2.9}$$

where $I = 7/2$ and $J = 1/2$ for $6^2S_{1/2}$, the last expressions in the curly bracket denotes the Wigner $6j$ symbol. The reduced dynamical scalar polarizability $\alpha_{nJ}^{(1)}$ and vector polarizability $\alpha_{nJ}^{(2)}$ are given by:

$$\begin{aligned}\alpha_{nJ}^{(K)} = (-1)^{K+J+1}\sqrt{2K+1}\sum_{n'J'}(-1)^{J'}\begin{Bmatrix} 1 & K & 1 \\ J & J' & J \end{Bmatrix}\left|\langle n'J'|\,|\mathbf{d}|\,|nJ\rangle\right|^2 \\ \times\frac{1}{\hbar}\mathrm{Re}\left(\frac{1}{\omega_{n'J'}-\omega_{nJ}-\omega-i\gamma_{n'J'nJ}/2}+\frac{(-1)^K}{\omega_{n'J'}-\omega_{nJ}+\omega+i\gamma_{n'J'nJ}/2}\right).\end{aligned} \tag{2.10}$$

where $\hbar$ is the reduced Planck constant, $\gamma_{n'J'nJ}$ stands for the linewidth of the transition between the fine-structure levels $|nJ\rangle$ and $|nJ\rangle$, $|\langle n'J'|\,|\mathbf{d}|\,|nJ\rangle|$ is the reduced dipole moment and is related to the transition probability coefficients:

$$A_{n'J'nJ} = \frac{(\omega_{n'J'}-\omega_{nJ})^3}{3\pi\epsilon_0\hbar c^2}\frac{1}{2J+1}\left|\langle n'J'|\,|\mathbf{d}|\,|nJ\rangle\right|^2, \tag{2.11}$$

where c is the speed of light, ϵ_0 is the vacuum permittivity.

The polarizability of the cesium ground state $6^2S_{\frac{1}{2}}$ is shown in Fig. 2.6. The nanofiber-guided trapping light fields at 783 nm and 1064 nm are blue- and red-detuned from the D_1 and D_2 transitions, respectively. Therefore the scalar polarizabilities at these two wavelengths have opposite signs. It is worth noting that at ∼880 nm, the scalar component of the polarizability vanishes, but its vector component remains significant. Thus, we can use a light field at ∼880 nm to add a light shift that is proportional to the m_F number, which imitates the effect of a magnetic field.

Die approbierte gedruckte Originalversion dieser Dissertation ist an der TU Wien Bibliothek verfügbar.
The approved original version of this doctoral thesis is available in print at TU Wien Bibliothek.
TU Bibliothek Your knowledge hub WIEN

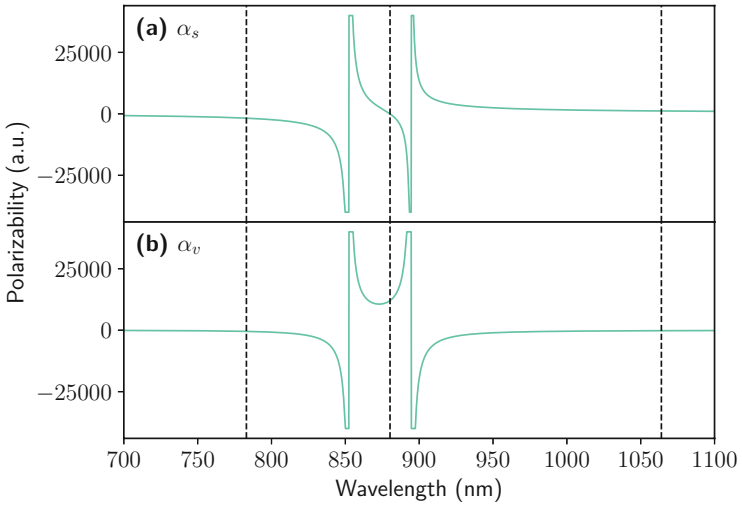

	783 nm ('blue')	880.2524 nm	1064 nm ('red')
α_s (a.u.)	-1761.6	0.0	1164.0
α_v (a.u.)	-480.0	12031.1	-198.6

Figure 2.6: Scalar (a) and vector (b) components of the polarizability of the ground state $6^2S_{\frac{1}{2}}$ of atomic cesium for vacuum wavelength from 700 nm to 1100 nm. The scalar polarizability has a sign change near the D_2 and D_1 transition lines at $852\,\mathrm{nm}$ and $895\,\mathrm{nm}$, respectively. The scalar polarizability crosses zero at $\sim$880 nm, where the contributions from the D_2 and D_1 transitions cancel out. The values here are compiled from the published paper by Fam et al. [38].

2.4 Nanofiber-based two-color trapping potential

A typical trapping configuration is mentioned previously in section 2.1, where we use a combination of a $783\,\mathrm{nm}$ running light and a pair of $1064\,\mathrm{nm}$ laser fields to form a standing wave. The total trapping potential is given by the sum of the light shifts originating from the trapping light fields, U_{LS}, and the surface-induced Van der Waals potential, U_s. The light-shift potential can be approximated using only the scalar component of the polarizability, while the Van der Waals potential can be approximated by $U_s = -C_3/(r-a)^3$, where $C_3 = 2\pi\hbar \times 1.16\,\mathrm{kHz}\,\mu\mathrm{m}^3$ for the electronic ground state of cesium $6S_{1/2}$ [39]. For the trapping configurations in the thesis, the contribution of the surface-induced potential is negligible as the trap minimum is more than $200\,\mathrm{nm}$ away from the surface. The total trapping potential is shown in Fig. 2.7. Here, the standing wave and running wave have a power of $2.88\,\mathrm{mW}$ and $17.8\,\mathrm{mW}$, respectively. Fig. 2.7(a) shows the potential in the x (radial)-direction. The red-detuned trapping light field gives an attractive potential while the blue-detuned trapping light field gives a repulsive potential. As the decay length of the evanescent field is longer for the light with the larger wavelength, the red- and blue-detuned light fields form a trap minimum in the x-direction that is $\sim$280 nm from the surface of the nanofiber. Since the red- and blue-detuned trapping fields have orthogonal quasi-

Die approbierte gedruckte Originalversion dieser Dissertation ist an der TU Wien Bibliothek verfügbar.
The approved original version of this doctoral thesis is available in print at TU Wien Bibliothek.
TU Bibliothek Your knowledge hub WIEN

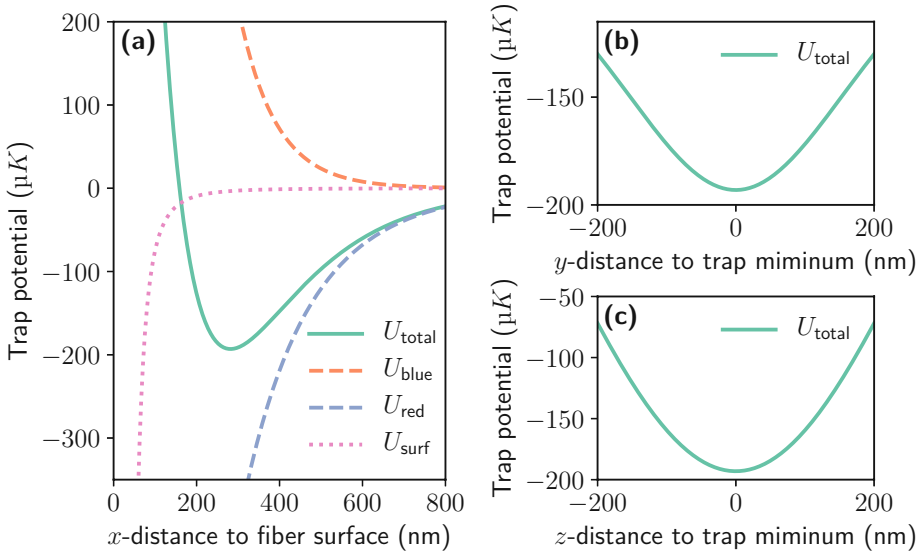

Figure 2.7: Nanofiber-based trapping potential for neutral cesium atoms. (a) Trapping potential in the x-direction (solid black line). The trapping potential is the sum of the scalar light shift induced by the red-detuned light field U_{red} (red-dashed line) and by the blue-detuned light field U_{blue} (red-dashed line), and the Van der Waals potential induced by the nanofiber. Here, potential minimum is $\sim$280 nm away from the surface of the nanofiber. (b) Trapping potential in the y-direction. (c) Trapping potential in the z-direction. Both potentials, along the y- and z-directions are symmetric and close to harmonic near the trap minimum. The origins in panels (b) and (c) correspond to the location of the trap minimum.

linearly polarizations, the rotational symmetry of the trapping potential is broken, and the atoms are confined in the y (azimuthal)-direction (see Fig. 2.1). The confinement in the z (axial)-direction is realized by a standing wave formed by a pair of counter-propagating red-detuned light fields. The atoms are trapped at the node positions of the standing wave. The potential near the trap minimum is close to harmonic in the x- and y-directions.

2.5 Measuring the optical density of nanofiber-trapped atoms via transmission spectroscopy

A simple way to characterize the nanofiber-trapped atoms is to measure their optical density (OD) via transmission spectroscopy. We carry out the transmission measurement in the weak saturation regime using a probing light field with a few pW power. We perform this measurement at 0 G of external magnetic field to avoid Zeeman splitting of m_F substates. The probe light field propagates in the $-z$ direction (see Fig. 2.5). When the probe light is on resonance, the amplitude transmission coefficient is given by [25]:

$$t_- = 1 - 2\beta_-, \tag{2.12}$$

Die approbierte gedruckte Originalversion dieser Dissertation ist an der TU Wien Bibliothek verfügbar.
The approved original version of this doctoral thesis is available in print at TU Wien Bibliothek.
TU Bibliothek Your knowledge hub WIEN

where β_- is the directional β factor and is defined as follows:

$$\beta_- = \frac{\gamma_-}{\gamma_+ + \gamma_- + \Gamma_{\text{om}}}, \tag{2.13}$$

where $\gamma_\pm$ is the spontaneous emission rate into the $\pm z$ mode and Γ_{om} is the emission rate into other modes. Both Γ_{om} and $\beta_\pm$ can be computed using an *ab initio* simulation [40].

The intensity transmission coefficient with N trapped atoms is given by:

$$T_- = |t|^{2N} = |1 - 2\beta_-|^{2N}. \tag{2.14}$$

For our experimental setting $0 < \beta_- << 1$, we can rewrite equation 2.14 as follows:

$$T_- = \exp(\ln(1 - 2\beta_-))^{2N} \approx \exp(2N \ln(1 - 2\beta_-)) = \exp(-4\beta_- N). \tag{2.15}$$

The definition of OD for a resonant light field is $T_- = \exp(-\text{OD})$. Therefore, the OD for a resonant light field in the weakly saturated regime is $4\beta_- N$.

However, measuring OD with a resonant light light field can be challenging as the transmitted signal decreases exponentially, e.g., at OD$= 10$, the T_- for a resonant light field is $\sim 5 \times 10^{-5}$. To have a more robust way of determining OD, we measure the transmission spectra of nanofiber-trapped atoms. The OD can be inferred from the transmission dip in the spectra, i.e., the larger OD increases the amplitude and the width of the dip. To acquire a transmission spectrum, we scan the frequency of the probe laser field over a 100 MHz window that is centered on the $F = 4$ to $F^{'} = 5$ transition of the D_2-line. This scan is performed at a constant rate and within a 5 ms duration. We record the transmitted light with a single photon counting module (SPCM). We bin the acquired data at 10 µs, which results in a histogram shown in Fig. 2.8.

The probe light field is quasi-linearly polarized along the x-direction. The probe light exhibits a large component of σ^- (σ^+) polarization at the trapping sites on the $x > 0$ ($x < 0$) side of the nanofiber (see Fig. 2.5). During the transmission measurement, the probe light field quickly pumps the atoms to the two outermost Zeeman substates. Therefore, we can make the simplification to assume that the probing light field drives only the outermost cycling transitions $F = 4, m_F = \pm 4$ to $F^{'} = 5, m_F = \pm 5$ during the transmission measurement. The atoms in the two outermost Zeeman substates experience the same tensor light shift exerted by the trapping light fields, resulting in the shift of the resonant frequency. We infer the OD of the trapped atoms by fitting the transmission spectra as a function of the laser detuning:

$$I(\Delta) = \exp\left(-\text{OD}\frac{\frac{1}{4}\Gamma^2}{\frac{1}{4}\Gamma^2 + (\omega_l - \omega_{re})^2}\right), \tag{2.16}$$

where ω_l is the detuning of the laser frequency. The resonance frequency ω_{re} is set to be a free parameter in the fit to account for the tensor shift exerted by the trapping light fields. We use the natural linewidth of the cesium D_2 transition for Γ.

We show an example of the transmission spectra in Fig. 2.8. The first red shaded area (starting from bin 50) indicates the transmission spectrum H_0 of the atoms initially loaded in the trap. Each bin corresponds to a frequency interval of $\sim$0.2 MHz. After a sequence of atom preparation and manipulation, we measure another transmission spectrum H_1 (red shaded area starting

Die approbierte gedruckte Originalversion dieser Dissertation ist an der TU Wien Bibliothek verfügbar.
The approved original version of this doctoral thesis is available in print at TU Wien Bibliothek.
TU Bibliothek Your knowledge hub WIEN

from bin 760). In all measurements, we acquire a reference transmission H_{ref} (blue shaded area) in the absence of trapped atoms to account for the frequency-dependent variation of the input power. In addition, we also acquire the background transmission signal H_{bng} (green shaded area) without probing light to account for the long drift of the background noise. The background at $\sim$4 counts per bin originates mainly from the remaining Raman scattering of the blue-detuned trap laser. We compute the histogram corrected by the background and the reference signal:

$$H_n^{\text{corr}} = \frac{H_n - H_{\text{ref}}}{H_{\text{ref}} - H_{\text{bng}}}. \tag{2.17}$$

The number of loaded atoms to the nanofiber fluctuates from run to run. In addition to statistical variation, the initial atom number can also fluctuate due to change of experimental condition, e.g., the variation of MOT density before loading, the drift of cooler laser's frequency. The fluctuation of the atom number is detrimental when we want to compare the experimental results across different experimental runs. To mitigate this effect, we compute the ratio of the optical density before (OD_0) and after (OD_1) atom preparation and manipulation in each experimental run. Using the fit function 2.16, we infer OD_0 and OD_1 from H_n^{corr} and H_n^{corr}, respectively.

Die approbierte gedruckte Originalversion dieser Dissertation ist an der TU Wien Bibliothek verfügbar.
The approved original version of this doctoral thesis is available in print at TU Wien Bibliothek.

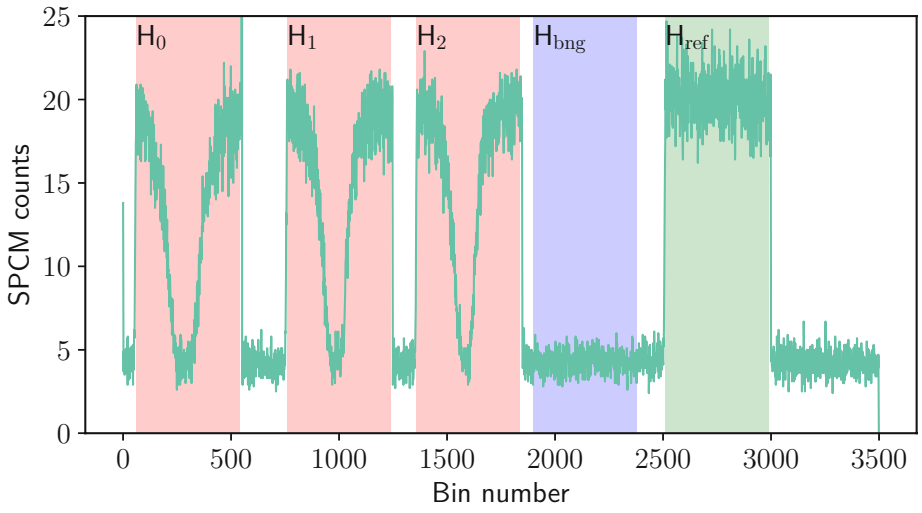

Figure 2.8: SPCM counts during transmission measurements of the nanofiber-trapped atoms. For each transmission measurement, we scan the frequency of the nanofiber-guided probe laser over a 100 MHz interval that is centered on the $F = 4 \rightarrow F' = 5$ transition of the D_2 line. The SPCM counts detected during this frequency scan correspond to the transmission spectrum, of which we use to infer the OD of the trapped atoms. We first measure the transmission spectrum H_0 after the atoms are initially loaded into the trap. After atom preparation and manipulation, we measure the spectrum again, see H_1 and H_2. We use H_1 for most of our experimental analysis and H_2 to monitor atom loss after measuring H_1. The two transmission spectrum H_{bng} and H_{ref} correspond to the background signal in the absence of the probing beam and the probe signal in the absence of atoms, respectively. Each bin has a 10 µs duration.

Die approbierte gedruckte Originalversion dieser Dissertation ist an der TU Wien Bibliothek verfügbar.
The approved original version of this doctoral thesis is available in print at TU Wien Bibliothek.

CHAPTER 3

Spin-motion coupling of nanofiber-trapped atoms

For nanofiber-trapped atoms, the phenomenon of 'killing' B-field was observed: when atoms were initially prepared in the $6S_{1/2}, F = 4$ hyperfine state, they became untrapped after being optically pumped from $6S_{1/2}, F = 4$ to $6S_{1/2}, F = 3$ at an offset magnetic field of $\sim$0.5 G [24]. In contrast, atoms remained trapped when the same operation was carried out at an offset magnetic field of 0 G. Since the trap depth is mostly independent of the magnetic field, the large increase of atoms' motion energy to escape the trapping potential has to originate from the larger Zeeman splitting. Later, the mechanism for the exchange of energy between spin and motional degrees of freedom (DOF) was discovered, namely the spin-motion coupling. In this chapter, we introduce the fictitious magnetic field which originates from the trapping light fields and show how it enables the spin-motion coupling of nanofiber-trapped atoms.

3.1 Fictitious magnetic field

As shown in chapter 2, the vector light shift depends on the total angular momentum operator $\hat{F}$. When an atom is in an eigenstate with respect to one of the components of $\hat{F}$, the vector light shift is proportional to m_F. Thereby, the vector light shift can be equivalent to the Zeeman energy splitting in a magnetic field. Thus, we can treat the vector light shift as an effective Zeeman interaction with a fictitious magnetic field [41]:

$$\hat{V}_{A_L}^{\text{vec}} = g_{nJF}\mu_B \boldsymbol{B}_{\text{fict}} \cdot \hat{\boldsymbol{F}}, \tag{3.1}$$

where μ_B is the Bohr magneton, g_{nJF} is the Landé factor for the level of hyperfine structure nJF, and the fictitious magnetic field $\boldsymbol{B}_{\text{fict}}$ is:

$$\boldsymbol{B}_{\text{fict}} = \frac{i\alpha_v}{8g_{nJF}\mu_B F}(\boldsymbol{E}^* \times \boldsymbol{E}). \tag{3.2}$$

Die approbierte gedruckte Originalversion dieser Dissertation ist an der TU Wien Bibliothek verfügbar.
The approved original version of this doctoral thesis is available in print at TU Wien Bibliothek.
TU Bibliothek Your knowledge hub WIEN

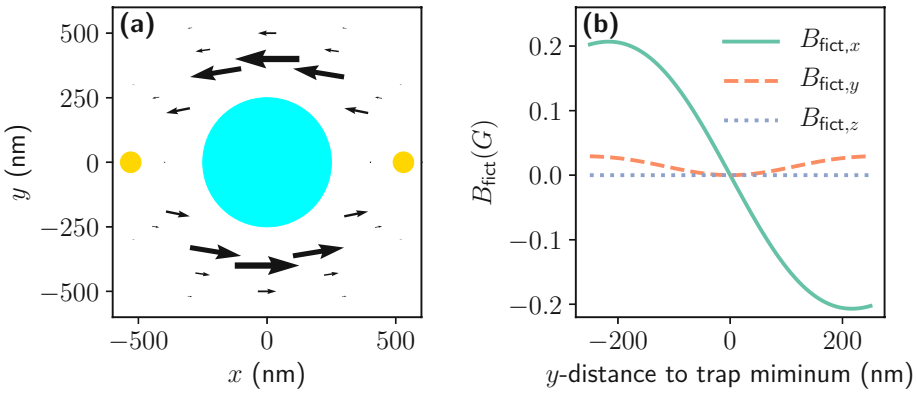

Figure 3.1: (a) Fictitious magnetic field of a nanofiber-guided light that is quasi-linearly polarized along the y-axis. Here we show the evanescent component in the xy-plane (shown as the black arrows). The fictitious magnetic field is maximum at $+y$ and $-y$ side of the nanofiber. The yellow circles represent the position of the trapped atoms, whereas the blue circle represents the cross-section of a nanofiber. (b) The gradient of the fictitious magnetic field along the y-axis. The origin is the position of the trapping potential minimum. The gradient is the largest in the x component of the fictitious magnetic field. The trapping configuration used for panels (a)-(b) can be found in the main text.

The fictitious magnetic field generated by the trapping light is depicted in Fig. 3.1. In panel (a), we see the fictitious magnetic field vector in the xy-plane. The trapping sites are indicated by the two yellow circles, and the blue circle represents the cross-section of the nanofiber. Since the longitudinal components of the two counter-propagating red-detuned light fields cancels out, the main contribution of the fictitious magnetic field comes from the blue-detuned light field that is quasi-linearly polarized along the y-axis. The fictitious magnetic field is maximum above and below the nanofiber, where it points in the $\pm x$-direction. As shown in Fig. 3.1(a), the amplitude of fictitious magnetic field decays near exponentially along the radial direction.

In Fig. 3.1(b), we see Cartesian components of the fictitious magnetic field as a function of the distance from the trap minimum along the y-axis. Near the trap minimum, the fictitious magnetic field can be approximated by its x component and as a linear gradient along the y-axis. Therefore, in the xy-plane, the fictitious magnetic field near the trapping site can be modeled as:

$$\boldsymbol{B}_{\text{fict}} \approx b_y y e^{-\frac{x}{l}} \hat{\mathbf{e}}_x, \tag{3.3}$$

where $b_y = 1.6\,\text{G}/\mu\text{m}$ and $l = 78\,\text{nm}$ in a typical trapping configuration,.

3.2 Origin of spin-motion coupling for nanofiber-trapped atoms

In this section, we show how fictitious magnetic field gradients can enable the coupling of the spin and motional DOF of nanofiber-trapped atoms. By approximating the trapping potential to

Die approbierte gedruckte Originalversion dieser Dissertation ist an der TU Wien Bibliothek verfügbar.
The approved original version of this doctoral thesis is available in print at TU Wien Bibliothek.

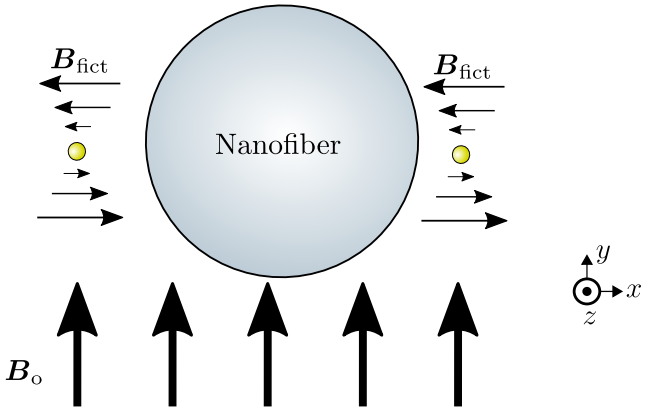

Figure 3.2: Schematic diagram for coupling between spin and y motional DOF. The fictitious magnetic field near the trapped atoms can be approximated as a linear gradient along y-axis and with its direction in x. An offset magnetic field is added along the y-axis. The atoms are indicated by the yellow circles.

be harmonic, the Hamiltonian of an atom in an external magnetic field is as follows:

$$\hat{H} = \sum_{i=x,y,z} \hbar\omega_i \hat{a}_i^\dagger \hat{a}_i + g_{nJF}\mu_B(\boldsymbol{B}_{\text{o}} + \boldsymbol{B}_{\text{fict}}) \cdot \hat{\boldsymbol{F}}), \tag{3.4}$$

where $\hat{a}_i$ and $\hat{a}_i^\dagger$ are the ladder operators of the motional state in the i DOF.

For simplicity, we now consider only the y DOF, and we use an approximation that the fictitious magnetic field has a linear gradient along the y-direction, see Fig. 3.2. By taking these simplifications into account, we have the following Hamiltonian of the nanofiber-trapped atom in an offset magnetic field in the y-direction:

$$\hat{H} = \hbar\omega_y \hat{a}_y^\dagger \hat{a}_y + g_{nJF}\mu_B(B_o \hat{F}_y + b_y y \hat{F}_x), \tag{3.5}$$

where the first term corresponds to the harmonic oscillator for y motional DOF, the second term represents the Zeeman interaction with the offset magnetic field and the fictitious magnetic field gradient along the y-direction.

Since the offset magnetic field is in the y-direction, it is convenient to use y as the quantization axis. We can replace the x-component of the angular momentum operator F_x with the ladder operators in the y-basis, $F_x = \frac{1}{2}(\hat{F}_+ + \hat{F}_-)$, and quantize the y motional DOF, $\hat{y} = y_0(\hat{a}_y + \hat{a}_y^\dagger)$, where y_0 is the RMS center-of-mass position of the y-motional ground state. After these substitutions, the Hamiltonian in 3.5 becomes:

$$\hat{H} = \hbar\omega_y \hat{a}_y^\dagger \hat{a}_y + \hbar\alpha_F B_0 \hat{F}_y + \hbar\frac{\Omega_y}{2}(\hat{a}_y + \hat{a}_y^\dagger)(\hat{F}_+ + \hat{F}_-), \tag{3.6}$$

where $\Omega_y = g_{nJF}\mu_B b_y y_0$, $\alpha_F = g_{nJF}\mu_B$, and Ω_y is the coupling strength between the spin and y motional DOF.

Die approbierte gedruckte Originalversion dieser Dissertation ist an der TU Wien Bibliothek verfügbar.
The approved original version of this doctoral thesis is available in print at TU Wien Bibliothek.
TU Bibliothek Your knowledge hub WIEN

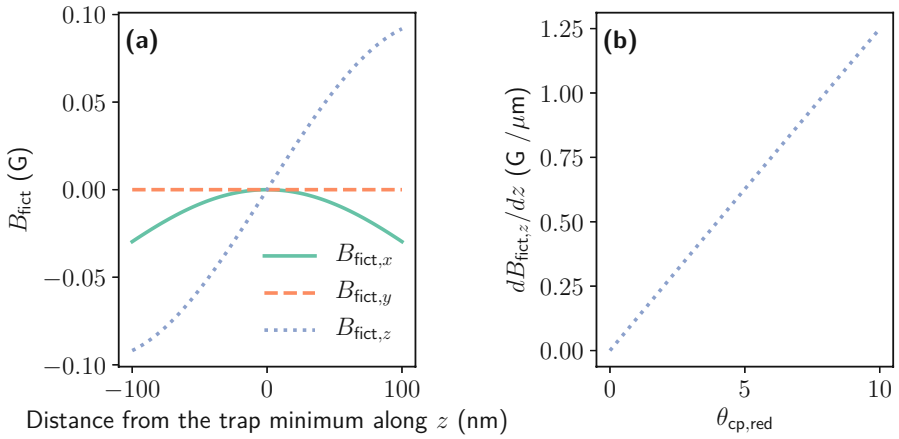

Figure 3.3: (a) Cartesian components of the fictitious magnetic field at different positions in the z-direction. The origin corresponds to the trap minimum. (b) Gradient of the fictitious magnetic field along the z-direction as a function of the angle $\theta_{cp,red}$ between the polarization axis of the two quasi-linearly polarized red-detuned trapping light fields.

In addition, the coupling between the spin and x motional DOF can be found by Taylor expanding the equation of fictitious magnetic field shown in 3.3:

$$B_{\text{fict}} \approx b_y y + b_y y(-\frac{x}{l}) + b_y y(\frac{x^2}{2l^2}) + O(x^3). \tag{3.7}$$

We now substitute the first three terms of the Taylor series in equation 3.4:

$$\begin{aligned}\hat{H} &= \sum_{i=x,y,z} \hbar\omega_i \hat{a}_i^\dagger \hat{a}_i + \hbar\alpha_F B_0 \hat{F}_y + g_{nJF}\mu_B(b_y\hat{y} + b_y\hat{y}(-\frac{\hat{x}}{l}) + b_y\hat{y}(\frac{\hat{x}^2}{2l^2}))\hat{F}_x \\ &= \sum_{i=x,y,z} \hbar\omega_i \hat{a}_i^\dagger \hat{a}_i + \hbar\alpha_F B_0 \hat{F}_y + \hbar\frac{\Omega_y}{2}(\hat{a}_y + \hat{a}_y^\dagger)(\hat{F}_+ + \hat{F}_-) \\ &\quad - \hbar\frac{\Omega_{xy}}{2}(\hat{a}_x + \hat{a}_x^\dagger)(\hat{a}_y + \hat{a}_y^\dagger)(\hat{F}_+ + \hat{F}_-) + \hbar\frac{\Omega_{xxy}}{2}(\hat{a}_x + \hat{a}_x^\dagger)^2(\hat{a}_y + \hat{a}_y^\dagger)(\hat{F}_+ + \hat{F}_-),\end{aligned} \tag{3.8}$$

where $\Omega_{xy} = by_0x_0/l$, $\Omega_{xxy} = by_0x_0^2/(2l^2)$.

We see from equation 3.8 that the 1st Taylor polynomial results in the coupling of the spin and y motional DOF, which corresponds to the Hamiltonian in equation 3.5. In contrast, the higher-degree Taylor polynomials result in the coupling between the spin and both the x and y motional DOF.

A direct coupling between the spin and z motional DOF can occur when there's an angle between the polarization axes of the two counter-propagating red-detuned trapping light fields.

Die approbierte gedruckte Originalversion dieser Dissertation ist an der TU Wien Bibliothek verfügbar.
The approved original version of this doctoral thesis is available in print at TU Wien Bibliothek.
TU Bibliothek Your knowledge hub WIEN

This angle gives rise to a linear gradient of the fictitious magnetic field along the z-direction. In Fig. 3.3 (a), the Cartesian components of the fictitious magnetic field are plotted as a function of the distance from the trap minimum in the z-direction. In Fig. 3.3 (b), the gradient of the fictitious magnetic field is plotted against the angle between the polarizations of the two counter-propagating red-detuned light fields. In analogy to the coupling shown in equation 3.6, this gradient gives rise to the coupling between spin and z motional DOF:

$$\hat{H} = \hbar\omega_z \hat{a}_z^\dagger \hat{a}_z + g_{nJF}\mu_B(B_o\hat{F}_y + b_z z\hat{F}_z), \tag{3.9}$$

where b_z is the fictitious magnetic field gradient along the z-direction.

Similarly to the derivation of the coupling between spin and y motional DOF, we can express spin operators in the y basis, $F_z = -\frac{i}{2}(\hat{F}_+ - \hat{F}_-)$, and quantize the z DOF, $\hat{z} = z_0(\hat{a_z} + \hat{a_z}^\dagger)$. We substitute these expressions in equation 3.9:

$$\hat{H} = \hbar\omega_z \hat{a}_z^\dagger \hat{a}_z + \hbar\alpha_F B_0 \hat{F}_y + \hbar\frac{i\Omega_z}{2}(\hat{a}_z + i\hat{a}_z^\dagger)(\hat{F}_- - \hat{F}_+). \tag{3.10}$$

As a summary, we list the relevant parameters including the calculated spin-motion coupling strengths in the following table:

$P_{1063\,\mathrm{nm}}$	$2.88\,\mathrm{mW}$
$P_{783\,\mathrm{nm}}$	$17.8\,\mathrm{mW}$
ω_x	$2\pi\times136\,\mathrm{kHz}$
ω_y	$2\pi\times83\,\mathrm{kHz}$
ω_z	$2\pi\times215\,\mathrm{kHz}$
Ω_y	$2\pi\times12\,\mathrm{kHz}$
Ω_{xy}	$2\pi\times2.6\,\mathrm{kHz}$
Ω_{xxy}	$2\pi\times0.28\,\mathrm{kHz}$
Ω_z $(\theta_{cp,red} = 5°)$	$2\pi\times1.4\,\mathrm{kHz}$

Table 3.1: Table of parameter values. The trapping laser powers are taken from experimental values (see chapters 5 and 6). The trap frequencies and spin-motion coupling strengths are inferred from an *ab initio* calculation.

Die approbierte gedruckte Originalversion dieser Dissertation ist an der TU Wien Bibliothek verfügbar.
The approved original version of this doctoral thesis is available in print at TU Wien Bibliothek.
TU Bibliothek Your knowledge hub WIEN

Die approbierte gedruckte Originalversion dieser Dissertation ist an der TU Wien Bibliothek verfügbar.
The approved original version of this doctoral thesis is available in print at TU Wien Bibliothek.

CHAPTER 4

Introduction to fluorescence spectroscopy

4.1 Overview

Resonance fluorescence is a textbook example of quantum optics. In particular, the fluorescence spectrum from optically-trapped cold atoms provides important insight into atoms' internal and external states [42–45]. In this thesis, fluorescence spectra are used to obtain atom's mean motional quanta (see chapter 5) as well as to investigate the coupling between atom's internal and external degrees of freedom (DOF) (see chapter 6). To understand the characteristics of fluorescence spectra, we cover the essential theoretical framework for resonant fluorescence and its experimental implementation with nanofiber-trapped atoms. In particular, we discuss resonance fluorescence in the case of the interaction between a single mode light field and a two-level system, using both the rate equation approach and the quantum master equation approach. Finally, we show how fluorescence spectroscopy can be utilized as a thermometer for the nanofiber-trapped atoms, and how we measure the fluorescence spectrum using heterodyne spectroscopy.

An intuitive understanding of the fluorescence spectrum can be obtained by considering a harmonically-bounded atom which acts as a pointlike scatterer. For simplicity, the atom is confined in a one-dimensional harmonic potential along the z-direction, see Fig. 4.1. The motion of the atom along the z-axis is $z(t) = z_a \sin(\omega_z t)$, where z_a is the amplitude of the oscillation along the z-axis, ω_z is the trap frequency in the z DOF. Here, the incident light field is treated as a plane wave. The plane wave is a valid assumption when the variation of the incident light field's intensity or polarization is negligible in the spatial extent of atom's center-of-mass trajectory. The wavevectors of the incident photon $\boldsymbol{k}_\mathrm{I}$ and of the scattered photon $\boldsymbol{k}_\mathrm{S}$ give a net change of the wavevector to the atom. The wavevector change along the z-axis is $\Delta k_z = (\boldsymbol{k}_\mathrm{I} - \boldsymbol{k}_\mathrm{S}).\boldsymbol{e}_z$, where $\boldsymbol{e}_z$ is the unit vector in the z-axis. The motion of the atom modifies the phase of the scattered light field:

$$E_s(t) = E_0 \exp(-i(\omega_L t + \Delta k z(t))). \tag{4.1}$$

Die approbierte gedruckte Originalversion dieser Dissertation ist an der TU Wien Bibliothek verfügbar.
The approved original version of this doctoral thesis is available in print at TU Wien Bibliothek.
TU Bibliothek Your knowledge hub WIEN

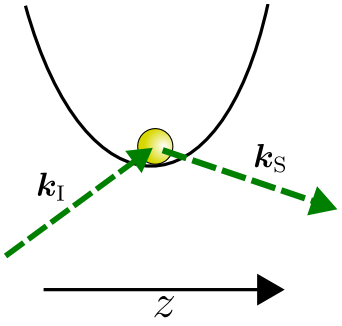

Figure 4.1: Illustration of light scattered by a trapped atom. The wavevectors of the incident and scattered light field are denoted by $\boldsymbol{k}_\mathrm{I}$ and $\boldsymbol{k}_\mathrm{S}$, respectively.

The normalized power spectrum $S(\omega)$ of $E_s(t)$ is defined as the Fourier transformation of the normalized first-order correlation function:

$$S(\omega) = \mathrm{Re}\left\{\frac{1}{2\pi}\int_0^\infty \frac{\langle E_s^*(t+\tau)E_s(t)\rangle}{\langle E_s^*(t)E_s(t)\rangle}\mathrm{e}^{-i\omega\tau}\,d\tau\right\}. \tag{4.2}$$

Substituting equation 4.1 into equation 4.2, we have [45]:

$$S(\omega) = \sum_{n=\infty}^{n=-\infty} J_n(\Delta k z_a)^2 \delta(\omega - \omega_L + n\omega_z), \tag{4.3}$$

where J_n is the nth order Bessel function.

From equation 4.3, we see that the motional sidebands at frequecies of $\omega_L \pm n\omega_z$ arise from the motion of the atom in a harmonic well. The amplitude ratio between the sum of the first-order sidebands, $S(\omega_L - \omega_z) + S(\omega_L + \omega_z)$, and the carrier transition $S(\omega_L)$ is:

$$\frac{S(\omega_L - \omega_z) + S(\omega_L + \omega_z)}{S(\omega_L)} = \frac{J_n(\Delta k z_a)^2 + J_n(\Delta k z_a)^2}{J_n(\Delta k z_a)^2} = \frac{(\Delta k z_a)^2}{2} = (\Delta k z_\mathrm{RMS})^2, \tag{4.4}$$

where z_RMS is the root mean square extent of the atom position, and $z_\mathrm{RMS} = z_a/\sqrt{2}$.

4.2 Rate equation approach

The full quantum calculation of the fluorescence spectrum can be cumbersome as the computation complexity grows exponentially with the number of atomic states considered. Hence, rate equations are often used to approximate the fluorescence spectrum. In the low saturation limit where the excited state is scarcely populated, we can use second-order perturbation theory for the transition rate between the two motional states n_i and n_f of the atom in its electronic ground state $|g\rangle$ [46]:

$$\Gamma_{n_i \to n_f} = \frac{\gamma_c}{4\pi}\int_\Omega \left|\sum_j \langle n_f|\, e^{-i\boldsymbol{k}_\mathrm{S}\cdot\boldsymbol{z}}\,|e_j\rangle\,\langle e_j|\, e^{i\boldsymbol{k}_\mathrm{I}\cdot\boldsymbol{z}}\,|n_i\rangle\right|^2 d\Omega, \tag{4.5}$$

Die approbierte gedruckte Originalversion dieser Dissertation ist an der TU Wien Bibliothek verfügbar.
The approved original version of this doctoral thesis is available in print at TU Wien Bibliothek.
TU Bibliothek Your knowledge hub WIEN

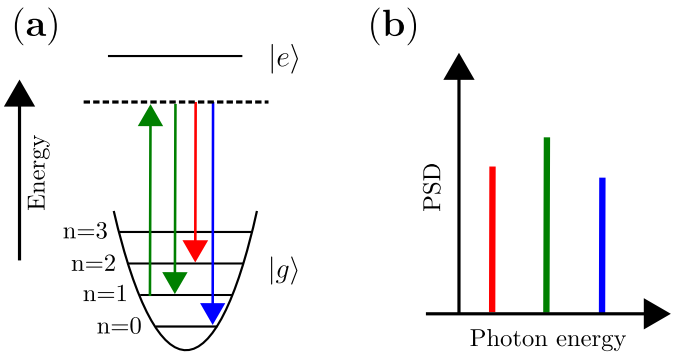

Figure 4.2: (a) Schematic diagram of resonance fluorescence of a trapped two-level atom. The motion of atom in the electronic ground state $|g\rangle$ is bound by a harmonic potential. The incident excitation light field is far-detuned from the atomic transition and the excited state has a negligible population. The up-arrow represents the incident light field, and the three down-arrows represent the atom-emitted light fields. (b) Fluorescence spectrum corresponding to the transitions indicated in panel (a). The central peak corresponds to the carrier transition where the motional state is unchanged. The left (right) peak corresponds to the first-order red (blue) sideband transition where one motional quantum is gained (lost) after scattering.

where γ_c is the rate of the carrier transition, $|e_j\rangle$ is an electronic excited state. Here, we abbreviate $|g, n\rangle$ to $|n\rangle$. The transition rate is integrated over all solid angle.

Since the sum of the excited states $\sum_j |e_j\rangle \langle e_j|$ form a complete set, equation 4.5 can be simplified to:

$$\Gamma_{n_i \to n_f} = \frac{\gamma_c}{4\pi} \int_\Omega \left| \langle n_f | \, e^{-i(\boldsymbol{k}_S - \boldsymbol{k}_I)\cdot \boldsymbol{z}} \, | n_i \rangle \right|^2 d\Omega. \tag{4.6}$$

Let's consider a subset of the atom-scattered light propagating within a small solid angle $\delta\Omega_{\mathrm{fg}}$, and is coupled to a nanofiber-guided mode. Equation 4.6 becomes:

$$\gamma_{n_i \to n_f} = \frac{\gamma_c}{4\pi} \left| \langle n_f | \, e^{-i(\boldsymbol{k}_S - \boldsymbol{k}_I)\cdot \boldsymbol{z}} \, | n_i \rangle \right|^2 \delta\Omega_{\mathrm{fg}}. \tag{4.7}$$

The resonance fluorescence for a two-level atom is depicted in Fig. 4.2(a). The atom in the electronic ground state $|g\rangle$ experiences a one-dimensional potential along the z-axis. Fig. 4.2(b) depicts the corresponding fluorescence spectrum for the transitions shown in Fig. 4.2(a). The combination of incident light field and scattered light field can alter the motion states of the atoms. For example, the Stokes (anti-Stokes) transition that increases (lowers) one motional quantum corresponds to the first-order red- (blue-) motional sideband shown in panel (b). The center line in panel (b) corresponds to the carrier transition where the motional state is unchanged. An important parameter in the fluorescence spectrum is the ratio between the area of the red- and blue-motional sidebands. Since the anti-Stokes transition is not available for atoms in the motional ground state, the larger asymmetry of the sidebands indicates the lower temperature of the atom. The ratio between the first-order sidebands is:

Die approbierte gedruckte Originalversion dieser Dissertation ist an der TU Wien Bibliothek verfügbar.
The approved original version of this doctoral thesis is available in print at TU Wien Bibliothek.
TU Bibliothek Your knowledge hub WIEN

$$\frac{S_{\Delta-1}}{S_{\Delta 1}} = \frac{\sum_{n=1}^{\infty} \pi_n \gamma_{n\to n-1}}{\sum_{n=0}^{\infty} \pi_n \gamma_{n\to n+1}} = \frac{\sum_{n=0}^{\infty} \pi_{n+1} \gamma_{n+1\to n}}{\sum_{n=0}^{\infty} \pi_n \gamma_{n\to n+1}}, \tag{4.8}$$

where π_n denotes the population of the atom in $|g, n\rangle$.

For atoms that are thermalized, the population of the motional state π_n follows the Boltzmann distribution:

$$\pi_n = (1-q)q^n, \tag{4.9}$$

where q is the Boltzmann factor:

$$q = \exp(-\frac{\hbar\omega_z}{k_B T}), \tag{4.10}$$

where $\hbar\omega_z$ is a motional quantum, T is the temperature, and k_B is the Boltzmann constant.

By substituting the expression 4.9 for π_n into equation 4.8, we see that the ratio between the two first-order motional sidebands equals to the Boltzmann factor:

$$\frac{S_{\Delta-1}}{S_{\Delta 1}} = q. \tag{4.11}$$

Furthermore, there is a fixed relationship between the mean number of motional quanta $\langle n\rangle$ and the Boltzmann factor:

$$\langle n\rangle = \frac{\sum_{n=0}^{\infty} \pi_n n}{\sum_{n=0}^{\infty} \pi_n} = \frac{q}{1-q}. \tag{4.12}$$

Although the harmonic potential well considered here has infinite depth, we see from equation 4.12 that this relationship remains unchanged when the motional states are truncated, i.e., summing over a finite number of the trapped states.

In addition, we can look at the ratio between the carrier transition and the sideband transitions. The exponential function in the transition rate equation 4.7 can be rewritten as a Taylor series:

$$e^{-i(\boldsymbol{k}_S - \boldsymbol{k}_I)\cdot \boldsymbol{z}} = e^{-i(\Delta \boldsymbol{k})\cdot \boldsymbol{z}} = 1 - i\Delta k_z z + O(z^2), \tag{4.13}$$

where z is the magnitude of the vector $\boldsymbol{z}$, Δk_z is the change of the wavevector along the z-axis.

We can quantize the z DOF and substitute z in equation 4.13 with the operator $\hat{z} = z_0(\hat{a}_z + \hat{a}_z^\dagger)$, where $\hat{a}_z^\dagger$ ($\hat{a}_z$) is the raising (lowering) operator, and z_0 is the root mean square extent of the motional ground state. Equation 4.7 then becomes:

$$\gamma_{n_i\to n_f} = \frac{\gamma_c}{4\pi} \left| \langle n_f | \left(1 - i\Delta k_z(\hat{a}_z + \hat{a}_z^\dagger)\right) | n_i\rangle \right|^2 \delta\Omega_{\text{fg}}. \tag{4.14}$$

The rate for the carrier transition is:

$$\gamma_{n\to n} = \frac{\gamma_c}{4\pi} |\langle n| 1 |n\rangle|^2 \delta\Omega_{\text{fg}} = \frac{\delta\Omega_{\text{fg}}}{4\pi}\gamma_c, \tag{4.15}$$

Die approbierte gedruckte Originalversion dieser Dissertation ist an der TU Wien Bibliothek verfügbar.
The approved original version of this doctoral thesis is available in print at TU Wien Bibliothek.
TU Bibliothek Your knowledge hub WIEN

and the rates for the first-order sideband transitions are:

$$\begin{aligned}\gamma_{n\to n+1} &= \frac{\gamma_c}{4\pi}\left|\langle n+1| - i\Delta k_z z_0(\hat{a}_z + \hat{a}_z^\dagger)\,|n\rangle\right|^2 \delta\Omega_{\text{fg}} = (\Delta k_z z_0)^2(n+1)\frac{\gamma_c}{4\pi}\delta\Omega_{\text{fg}},\\ \gamma_{n\to n-1} &= \frac{\gamma_c}{4\pi}\left|\langle n-1| - i\Delta k_z z_0(\hat{a}_z + \hat{a}_z^\dagger)\,|n\rangle\right|^2 \delta\Omega_{\text{fg}} = (\Delta k_z z_0)^2 n\frac{\gamma_c}{4\pi}\delta\Omega_{\text{fg}}.\end{aligned} \tag{4.16}$$

From equations 4.15 and 4.16, we compute the ratio between areas of the two first-order sideband transitions $S_{\Delta 1} + S_{\Delta -1}$ and the carrier transition S_0:

$$\frac{S_{\Delta 1} + S_{\Delta -1}}{S_0} = \frac{\sum_{n=0}^{\infty}\pi_n\gamma_{n\to n+1} + \sum_{n=0}^{\infty}\pi_{n+1}\gamma_{n+1\to n}}{\sum_{n=0}^{\infty}\pi_n\gamma_{n\to n}}. \tag{4.17}$$

Using equations 4.15 and 4.16, we find the ratio between $S_{\Delta 1}$ and S_0:

$$\frac{S_{\Delta 1}}{S_0} = \frac{q(\Delta k_z z_o)^2}{1-q}. \tag{4.18}$$

Combining equations 4.12, 4.11, and 4.18, we have:

$$\frac{S_{\Delta 1} + S_{\Delta -1}}{S_o} = \frac{(q+1)(\Delta k_z z_0)^2}{(1-q)}. \tag{4.19}$$

For a thermal distribution, the root mean square extent of the center of mass position z_{RMS} is:

$$z_{\text{RMS}} = z_0\sqrt{2\langle n\rangle + 1} = z_0\sqrt{\frac{q+1}{1-q}}. \tag{4.20}$$

Therefore, equation 4.19 can be rewritten as:

$$\frac{S_{\Delta 1} + S_{\Delta -1}}{S_0} = z_{\text{RMS}}^2\Delta k_z^2 = (2\langle n\rangle + 1)\Delta k_z^2 {z_0}^2. \tag{4.21}$$

We see equation 4.21 matches equation 4.4 that is derived from a simple classical model.

4.3 Fluorescence spectrum of nanofiber-trapped atoms

So far, we have discussed the fluorescence spectrum limited to one motional DOF. In this section, we show how the fluorescence spectrum of nanofiber-trapped atoms can give information on all three motional DOF. For this discussion, we consider the experimental configuration in our setup, see Fig. 4.6. Here, the incident light field can be approximated as a plane wave that propagates in the $+y$-direction, and we observe the atom emission coupled into the nanofiber-guided mode.

At the position of the trapped atoms, we approximate the electric field of the nanofiber-guided mode as an exponential decay in the x-direction, i.e., the x-axis is normal to the surface of the nanofiber and intersects the position of the trapped atoms (see chapter 3): $E_{FG} \propto e^{-x/L}$, where L is the decay length of the fiber-guided light. We denote k_{nf} as the wavenumber of the nanofiber-guided mode and k_0 as the wavenumber of the excitation light field in free space.

Die approbierte gedruckte Originalversion dieser Dissertation ist an der TU Wien Bibliothek verfügbar.
The approved original version of this doctoral thesis is available in print at TU Wien Bibliothek.
TU Bibliothek Your knowledge hub WIEN

Similar to equation 4.6, we can write down the transition amplitude for the nanofiber-trapped atoms:

$$\gamma_{n_i \to n_f} = \frac{\gamma_c}{4\pi} \left| \langle n_f^x, n_f^y, n_f^z | \, e^{-x/L} e^{-ik_{fg}z} e^{ik_0 y} \, | n_i^x, n_i^y, n_i^z \rangle \right|^2 \delta\Omega_{\text{fg}}, \tag{4.22}$$

where $e^{ik_0 y}$ originates from the incident light field which propagates in y-direction, $e^{-ik_{fg}z}e^{-x/L}$ originates from the scattered light field that is coupled into the nanofiber-guided mode and propagates in the $+z$-direction.

The two exponential functions $e^{ik_0 y}$ and $e^{-ik_{fg}z}$ introduce spatial phase modulations in the y-direction and the z-direction, respectively. The phase modulations in the two directions result in the non-zero transition amplitude between the adjacent motional states which correspond to motional sidebands of the y and z DOF. Furthermore, the rate equation has a contribution from the amplitude gradient of the electric field in the x direction. By Taylor expanding $e^{-x/L}$ in x, we see the 1st Taylor polynomial results in the coupling between adjacent motional states in the x DOF, which leads to motional sidebands of the x DOF. For atoms trapped close to the motional ground state, the three motional DOF are separable. We can rewrite 4.22 as:

$$\gamma_{n_i \to n_f} = \frac{\gamma_c}{4\pi} \left| \langle n_f^x | \, e^{-x/L} \, | n_i^x \rangle \, \langle n_f^z | \, e^{-ik_{fg}z} \, | n_i^z \rangle \, \langle n_f^y | \, e^{ik_{fs}y} \, | n_i^y \rangle \right|^2 \delta\Omega_{\text{fg}}. \tag{4.23}$$

From this equation, we can see the expected first-order sideband amplitudes for the z, y, x DOF are proportional to $z_0 k_{fg}\sqrt{n_i^z}$, $y_0 k_{fs}\sqrt{n_i^z}$, and $x_0/L\sqrt{n_i^x}$, respectively. For an atom initially in the motional ground state in three DOF, we expect the ratio between the intensity of the first-order red x, y, z sidebands and the carrier transition to be 0.035, 0.025, 0.0096, respectively.

In conclusion, by collecting atom emission into the nanofiber-guided mode, motional sidebands in three DOF can be observed through a combination of phase and amplitude modulations. This allows us to simultaneously measure $\{\langle n_x \rangle, \langle n_y \rangle, \langle n_z \rangle\}$ of the nanofiber-trapped atoms.

4.4 Master equation approach

In this section we describe an alternative approach to simulate fluorescence spectra using master equations. The Hamiltonian for a two-level atom interacting with a laser is:

$$H = \hbar\omega_0 \, |e\rangle \langle e| + \frac{\hbar}{2}(\Omega_r \sigma^+ + \Omega_r^* \sigma^-), \tag{4.24}$$

where ω_{eg} is the energy of the two-level atom, Ω_r is the Rabi frequency.

The time evolution of an atom can be described by the master equation of Lindblad form [47]:

$$\dot{\rho} = \mathcal{L}\rho = -i[H, \rho] + \sum_i \frac{\Gamma_i}{2}(2\hat{c}_i \rho \hat{c}_i^\dagger - \{\hat{c}_i^\dagger \hat{c}_i, \rho\}) \tag{4.25}$$

where the last term is the Lindblad dissipator and $\hat{c}_i$ is a jump operator. For a two-level system, the jump operator $\hat{c}_i$ is a Pauli operator $\hat{\sigma}_- = |g\rangle \langle e|$.

Die approbierte gedruckte Originalversion dieser Dissertation ist an der TU Wien Bibliothek verfügbar.
The approved original version of this doctoral thesis is available in print at TU Wien Bibliothek.
TU Bibliothek Your knowledge hub WIEN

The time evolution of a driven two-level system can be derived from the master equation 4.25 and written as the Optical Bloch equations:

$$\frac{d}{dt}\begin{pmatrix}\langle\hat{\sigma}_-\rangle\\ \langle\hat{\sigma}_+\rangle\\ \langle\hat{\sigma}_z\rangle\end{pmatrix} = \begin{pmatrix} i\Delta_L - \frac{\Gamma}{2} & 0 & i\frac{\Omega_r}{2}\\ 0 & -i\Delta_L - \frac{\Gamma}{2} & -i\frac{\Omega_r^*}{2}\\ +i\Omega_r^* & -i\Omega_r & -\Gamma\end{pmatrix}\begin{pmatrix}\langle\hat{\sigma}_-\rangle\\ \langle\hat{\sigma}_+\rangle\\ \langle\hat{\sigma}_z\rangle\end{pmatrix} + \begin{pmatrix}0\\0\\\Gamma\end{pmatrix}, \tag{4.26}$$

where Δ_L is the laser detuning from the atomic transition frequency, Γ is the natural decay rate of the electronic excited state, $\hat{\sigma}_+ = |e\rangle\langle g|$, and $\hat{\sigma}_z = 0.5(|e\rangle\langle e| - |g\rangle\langle g|)$.

At the steady state, the solutions are:

$$\langle\hat{\sigma}_z\rangle_0 = -1 + \frac{s}{s+1} \tag{4.27}$$

and

$$\langle\hat{\sigma}_-\rangle_0 = \langle\hat{\sigma}_+\rangle_0^* = \frac{(\Delta_L + i\Gamma/2)}{\Omega}\frac{s}{s+1}, \tag{4.28}$$

where s is the saturation parameter:

$$s = \frac{2\Omega^2/\Gamma^2}{1 + 4{\Delta_L}^2/\Gamma^2}. \tag{4.29}$$

When the system is strongly driven, $s \gg 1$, $\langle\hat{\sigma}_z\rangle_0 \to 0$, meaning the excited state and the ground state are equally populated, whereas for a weakly driven system with $s \ll 1$, $\langle\hat{\sigma}_z\rangle_0 \to -1$, indicating the atom is in the ground state. The total scattering rate is [48]:

$$\gamma_s = \Gamma\frac{s}{2(s+1)}. \tag{4.30}$$

A fraction of the scattered light is coherent, and the coherent scattering rate is given by [48]:

$$\gamma_s^{coh} = \Gamma\,|\hat{\sigma}_-|^2 = \Gamma\frac{s}{2(s+1)^2}. \tag{4.31}$$

We see for $s \ll 1$, the two equations 4.30 and 4.31 coincide, meaning for a weakly driven system almost all scattering events are coherent processes. When $s > 1$, incoherent scattering becomes dominant.

The radiated spectra of incoherent scattering processes have spectral widths on the same order of magnitude as the natural linewidth, which is $2\pi \times 5.22\,\mathrm{MHz}$ for the cesium D_2 cycling transition $F = 4 \to F' = 5$. In contrast, the radiated spectrum of coherent scattering processes have spectral widths that are much narrower, e.g., for a two-level system excited by a monochromatic excitation light, its radiated spectrum is a delta function. To spectrally resolve the motional sidebands that are typically on the order of $100\,\mathrm{kHz}$, the coherent part of the scattering process should dominate. Therefore, the saturation parameter s should be kept small. In this case, the excited state is not populated and can be adiabatically eliminated. The corresponding Hamiltonian for an atom in a one-dimensional harmonic potential along the y-direction is:

$$H = \hbar\omega_y\hat{a}^\dagger\hat{a}. \tag{4.32}$$

Die approbierte gedruckte Originalversion dieser Dissertation ist an der TU Wien Bibliothek verfügbar.
The approved original version of this doctoral thesis is available in print at TU Wien Bibliothek.
TU Bibliothek Your knowledge hub WIEN

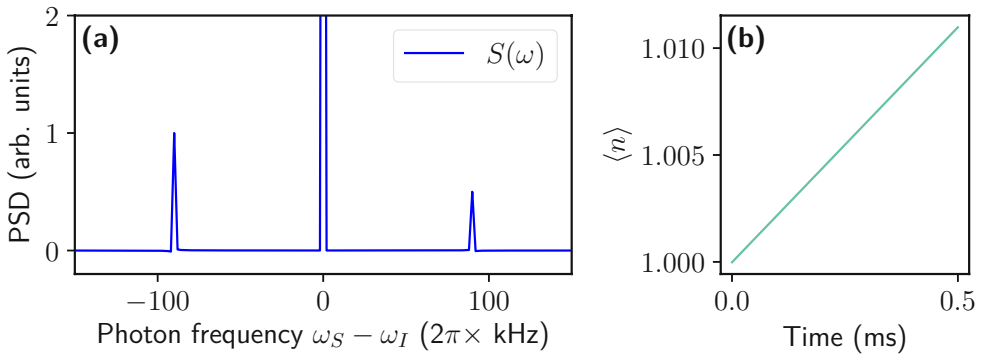

Figure 4.3: Simulated fluorescence spectrum using master equation. (a) Fluorescence spectrum with an initial mean excitation of 1. The time of evolution for the simulation is 0.5 ms. (b) Time evolution of the mean excitation $\langle n \rangle$. The heating rate of this process is linear.

The Lindblad dissipator for this system is $\hat{c} = \sqrt{\gamma}(1 + \sqrt{\eta}(\hat{a}^\dagger + \hat{a}))$, where $\sqrt{\eta}(\hat{a}^\dagger + \hat{a})$ corresponds to recoil heating from photon scattering. We can compute the spectrum with:

$$S(\omega) = \mathrm{Re}(\int_0^\infty e^{i\omega\tau}\langle\hat{c}^\dagger(\tau)\hat{c}(0)\rangle d\tau) \tag{4.33}$$

Note that an underlying assumption for equation 4.37 is that the system is in a stationary state, thus the computed spectrum is constant with respect to any chosen initial time.

We use QuTiP to numerically simulate the evolution of the trapped atom in discrete time steps using the master equation [49]. We assume atom's initial motional states to be thermally populated and the mean motional excitation $\langle n \rangle$ to be 1. We show the resulting spectrum in Fig. 4.3(a). From the ratio between the areas of two first-order motional sidebands, we infer $\langle n \rangle = 1.0$ quanta, within 1% agreement with the $\langle n \rangle$ averaged over the time evolution, $\langle \bar{n} \rangle$. In addition, we can also infer the $\langle n \rangle$ from the ratio of the carrier and the sum of the two first-order sidebands, which yields a similar value of 1.0 quanta. The discrepancy here originates from the fact that the system is not in a stationary state which is assumed for equation 4.37. Since there is no cooling process in the simulation to counteract recoil heating of the atom, the mean motional state excitation increases with time, see Fig. 4.3(b). In this simulation, we use parameters similar to our experimental setup: trap frequency of 90 kHz, η of 0.035.

In additional, we can simulate the spectrum when the Hamiltonian has a spin-motion coupling term (see chapter 3):

$$\hat{H} = \hbar\omega_y\hat{a}_y^\dagger\hat{a}_y + \hbar\alpha_F B_0\hat{F}_y + \hbar\frac{g_y}{2}(\hat{a}_y + \hat{a}_y^\dagger)(\hat{F}_+ + \hat{F}_-). \tag{4.34}$$

For simplicity, we consider only Zeeman substates $m_F = -4$ and $m_F = -3$ of the $F = 4$ hyperfine state of cesium's electronic ground state. This is a suitable model for many of our experimental settings, where we use a σ^- polarized excitation light field and atoms are populated at the lowest Zeeman substates.

Die approbierte gedruckte Originalversion dieser Dissertation ist an der TU Wien Bibliothek verfügbar.
The approved original version of this doctoral thesis is available in print at TU Wien Bibliothek.
TU Bibliothek Your knowledge hub WIEN

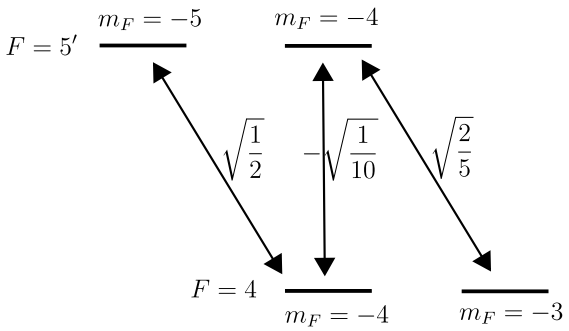

Figure 4.4: Cesium D_2 dipole matrix elements for transitions between the two lowerest m_F substates in $F = 4$ and $F^{'} = 5$.

When the excitation light field is σ^- polarized, the relevant transition operators are [50]:

$$\hat{J}_- = \sqrt{\frac{1}{2}} |e_{-4}\rangle \langle e_{-5}| + \sqrt{\frac{2}{5}} |e_{-3}\rangle \langle e_{-4}| ,$$
$$\hat{J}_0 = \sqrt{\frac{1}{10}} |g_{-4}\rangle \langle g_{-4}| . \tag{4.35}$$

The subscripts in $|e_n\rangle$ and $|g_n\rangle$ indicate the m_F substates. The dipole matrix elements between the m_F substates are taken into account in equation 4.35, see Fig. 4.4 [51]. The relevant jump operators are:

$$\hat{c}_- = \sqrt{\gamma} J_- J_-^\dagger (1 + \sqrt{\eta}(\hat{a}_y^\dagger + \hat{a}_y)),$$
$$\hat{c}_0 = \sqrt{\gamma} J_0 J_-^\dagger (1 + \sqrt{\eta}(\hat{a}_y^\dagger + \hat{a}_y)). \tag{4.36}$$

To calculate this spectrum we use:

$$S(\omega) = \mathrm{Re}\left(\int_0^\infty e^{i\omega\tau} \langle \hat{c}_-^\dagger(\tau) \hat{c}_-(0) \rangle d\tau\right) \tag{4.37}$$

The simulated spectrum is shown in Fig. 4.5. Due to spin-motion coupling, we no longer see the bare states in the spectrum, but rather the dressed states which are superpositions of the bare states, e.g., the bare states with a total of one excitation: $|m_F = -4, n = 1\rangle$ and $|m_F = -3, n = 0\rangle$. For this simulation, we set the atom initially close to the motional ground state. Hence, we expect to observe the transition from $|m_F = -4, n = 0\rangle$ to the pair of dressed states with one excitation, and also the transition between the dressed states of one and two excitations. The expected frequencies of these transitions (indicated by the vertical lines) match well with simulated peak positions.

Die approbierte gedruckte Originalversion dieser Dissertation ist an der TU Wien Bibliothek verfügbar.
The approved original version of this doctoral thesis is available in print at TU Wien Bibliothek.
TU Bibliothek Your knowledge hub WIEN

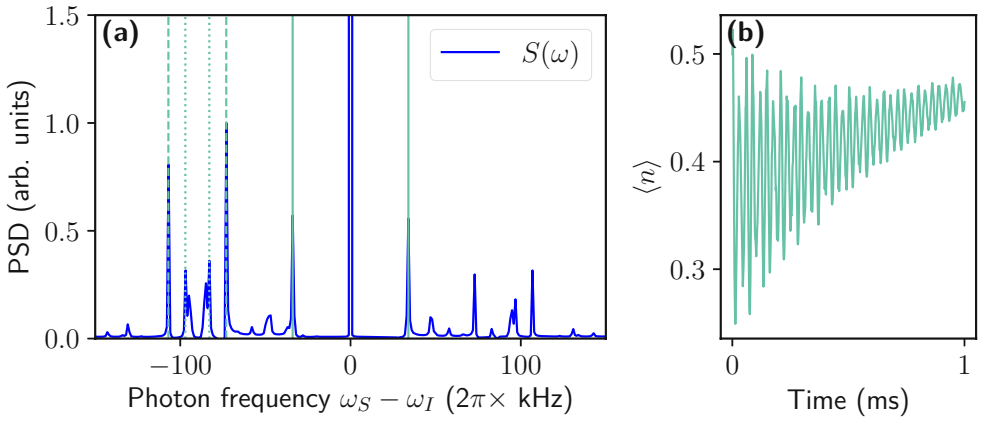

Figure 4.5: (a) Simulated fluorescence spectrum using master equation. The two vertical dashed lines indicate the expected frequency of the transition between $|m_F = -4, n = 0\rangle$ and the pair of dressed states which are superpositions of $|m_F = -4, n = 1\rangle$ and $|m_F = -3, n = 0\rangle$. The two dotted lines indicate the expected frequency of the transition between two pairs of dressed states, i.e., superpositions of $|m_F = -4, n = 1\rangle$ and $|m_F = -3, n = 0\rangle$ and of $|m_F = -4, n = 2\rangle$ and $|m_F = -3, n = 1\rangle$. For this simulation, $\omega_t = 2\pi \times 90\,\mathrm{kHz}$, $\Omega_y = 2\pi \times 34\,\mathrm{kHz}$, the scattering rate of the outermost cycling transition is $2\pi \times 2\,\mathrm{kHz}$. (b) Mean motional quanta as a function of time. The fast oscillation in panel (b) corresponds the energy exchange between spin and motional DOF.

4.5 Heterodyne fluorescence spectroscopy

We use heterodyne detection for fluorescence spectroscopy. We are interested in probing the motional sidebands that are on the order of 100 kHz away from the carrier transition. The atom-emitted light field has a frequency on the order of 300 THz, many orders of magnitude larger than the upper bandwidth limit of a photodetector. A common solution is to use heterodyne measurement, i.e., mixing the atomic fluorescence signal with a local oscillator which serves as a frequency reference. By measuring the beat frequency between the atomic signal and the local oscillator, we shift the relevant atomic signal from a few 100 THz to the MHz range, where it can be read out using a photodetector, e.g., a photodiode or an SPCM. The local oscillator can be realized using a reference light field that has a fixed frequency difference from the excitation light field. We can tune the frequency of the reference light with acoustic-optic modulators or electro-optic modulators. This way, we can set the beat frequency far from DC noise or other low-frequency noises.

The experimental setup is shown in Fig. 4.6. We split the input light field into two beams: One beam is used as the excitation light field for the nanofiber-trapped atoms. A part of the atom scattered light field is coupled into the nanofiber-guided mode and is denoted as E_s. The other beam is used as the local oscillator E_{LO}, which is frequency shifted from the input light field by 10 MHz. We generate this frequency shift using a pair of acoustic optical modulators. To observe the beating between E_s and E_{LO}, we match their polarization at the SPCM using a

Die approbierte gedruckte Originalversion dieser Dissertation ist an der TU Wien Bibliothek verfügbar.
The approved original version of this doctoral thesis is available in print at TU Wien Bibliothek.
TU Bibliothek Your knowledge hub WIEN

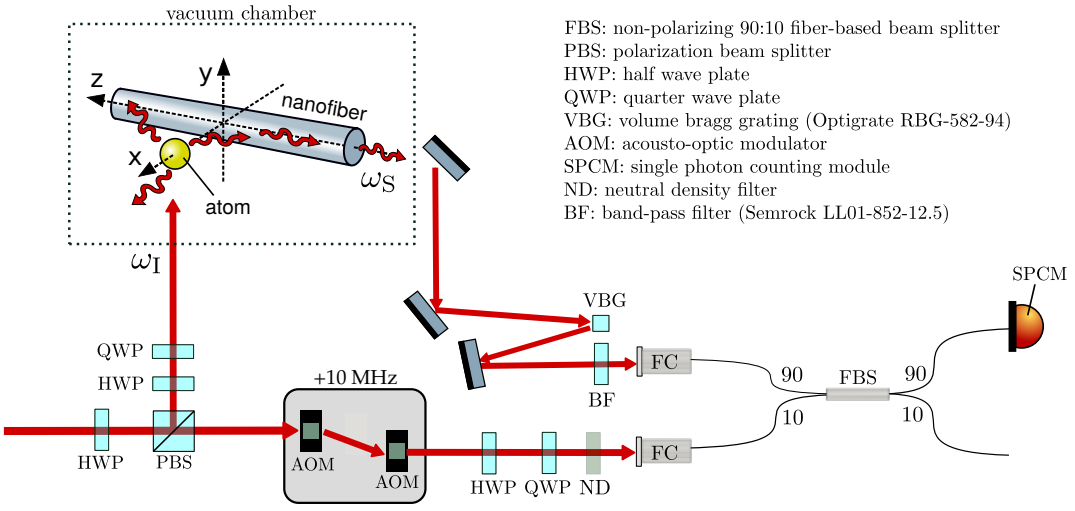

Figure 4.6: Experimental setup. Individual cesium atoms are trapped near the surface of an optical nanofiber. They are exposed to a near-resonant excitation light field (frequency ω_I), propagating along the $+y$-direction. A fraction of the atomic fluorescence is coupled into the guided mode of the nanofiber (frequency ω_S). This light field is superposed with a local oscillator that is derived from the excitation light and is frequency-shifted by $+10\,\mathrm{MHz}$. We record the combined light field with a single photon counting module (SPCM). Fourier analysis of the resulting signal yields the fluorescence spectrum, which grants access to the energy spectrum of the trapped atoms. The black dotted line indicates the vacuum chamber which encloses the nanofiber.

combination of a quarter waveplate and a half waveplate in the beam path of the local oscillator. The fiber-guided trapping light fields introduce Raman scattering processes that generate broadband Stokes photons in the signal beam path. To reduce detection of the background signals, i.e., the Stokes photons and trapping light, we employ a volume Bragg grating and a band-path filter before the SPCM. The Bragg grating and the band-path filter have center wavelength at $\sim$852 nm, and exhibit FWHM of 12.5 nm and 0.12 nm, respectively. The resulting background counts detected by the SPCM is $\sim$4 counts/10 µs for a typical trapping configuration (see chapter 2).

We now discuss how to retrieve the power spectrum from the heterodyne measurement. We can approximate the local oscillator with a single frequency component: $E_{\mathrm{LO}}(t) = E^0_{\mathrm{LO}} e^{i\omega_{\mathrm{LO}} t}$, where E^0_{LO} and ω_{LO} are the amplitude and the frequency of the local oscillator, respectively. In the heterodyne detection, we measure the intensity of the combined field $I_t = cn\epsilon_0 E_t E_t^*/2$, where $E_t = E_{\mathrm{LO}} + E_s$, c is the speed of light, n is the refractive index, ϵ_0 is the vacuum permittivity. The intensity correlation function is [52]:

$$G^1_t(\tau) = \langle I_t(t) I_t(t+\tau) \rangle_t \,, \tag{4.38}$$

Die approbierte gedruckte Originalversion dieser Dissertation ist an der TU Wien Bibliothek verfügbar.
The approved original version of this doctoral thesis is available in print at TU Wien Bibliothek.
TU Bibliothek Your knowledge hub WIEN

where $\langle ... \rangle_t$ denotes the time average, $I_t(t)$ is:

$$\begin{aligned} I_t(t) &= \frac{cn\epsilon_0}{2}(E_{\mathrm{LO}}(t) + E_s(t))(E_{\mathrm{LO}}(t)^* + E_s(t)^*) \\ &= I_{\mathrm{LO}} + I_s(t) + \frac{cn\epsilon_0}{2}(E^*_{\mathrm{LO}}(t)E_s(t) + c.c.). \end{aligned} \tag{4.39}$$

The local oscillator has a single frequency component, therefore its intensity $I_{\mathrm{LO}} = \frac{cn\epsilon_0}{2}|E_{\mathrm{LO}}|^2$ is time independent. By substituting equation 4.39 into 4.38, we have:

$$\begin{aligned} G^1_t(\tau) = &\ \langle I_t(t)I^*_t(t+\tau)\rangle_t \\ &= I^2_{\mathrm{LO}} + \langle I_s(t)I_s(t+\tau))\rangle_t + 2I_{\mathrm{LO}}\bar{I}_s + 2I_{\mathrm{LO}}\frac{cn\epsilon_0}{2}\langle E^*_{\mathrm{LO}}(t)E_s(t) + c.c.\rangle_t \\ &+ \frac{cn\epsilon_0}{2}\langle I_s(t)(E^*_{\mathrm{LO}}(t+\tau)E_s(t+\tau) + c.c.)\rangle_t + \frac{cn\epsilon_0}{2}\langle I_s(t+\tau)(E^*_{\mathrm{LO}}(t)E_s(t) + c.c.)\rangle_t \\ &+ \frac{c^2n^2\epsilon_0^2}{4}\langle (E^*_{\mathrm{LO}}(t)E_s(t) + c.c.)(E^*_{\mathrm{LO}}(t+\tau)E_s(t+\tau) + c.c.)\rangle_t . \end{aligned} \tag{4.40}$$

When the frequency of the local oscillator is far from any Fourier components of the atomic signal, the terms which include the product of the two fields, e.g., $E^*_{\mathrm{LO}}(t)E_s(t)$, have time averaged value of zero. In addition, the terms that include $e^{i2\omega_{\mathrm{LO}}t}$ or $e^{-i2\omega_{\mathrm{LO}}t}$ oscillate much faster than any Fourier components of $E_s(t)$ and $I_s(t)$, also have time average of zero. Equation 4.40 then simplifies to:

$$\begin{aligned} G^1_t(\tau) &= I^2_{\mathrm{LO}} + \langle I_s(t)I_s(t+\tau))\rangle_t + 2I_{\mathrm{LO}}\bar{I}_s + \frac{c^2n^2\epsilon_0^2}{4}\langle E^*_{\mathrm{LO}}(t)E_{\mathrm{LO}}(t+\tau)E_s(t)E^*_s(t+\tau) + c.c.\rangle_t \\ &= I^2_{\mathrm{LO}} + \langle I_s(t)I_s(t+\tau))\rangle_t + 2I_{\mathrm{LO}}\bar{I}_s + (e^{i\omega_{\mathrm{LO}}\tau}\frac{cn\epsilon_0}{2}I_{\mathrm{LO}}\langle E_s(t)E^*_s(t+\tau)\rangle_t + c.c.), \end{aligned} \tag{4.41}$$

where $\bar{I}_s = \langle I_s(t)\rangle_t$.

Now we perform Fourier transformation on equation 4.41:

$$\begin{aligned} \int G^1_t(\tau)e^{-i\omega\tau}d\tau &= \delta(0)(I^2_{\mathrm{LO}} + 2I_{\mathrm{LO}}\bar{I}_s) + \int \langle I_s(t)I_s(t+\tau))\rangle_t e^{-i\omega\tau}d\tau \\ &+ \frac{cn\epsilon_0}{2}(\int \langle E_s(t)E^*_s(t+\tau)\rangle_t e^{i(\omega_{\mathrm{LO}}-\omega)\tau}d\tau + \int \langle E^*_s(t)E_s(t+\tau)\rangle_t e^{-i(\omega_{\mathrm{LO}}+\omega)\tau}d\tau) \\ &= \delta(0)(I^2_{\mathrm{LO}} + 2I_{\mathrm{LO}}\bar{I}_s) + \int \langle I_s(t)I_s(t+\tau))\rangle_t e^{-i\omega\tau}d\tau \\ &+ \frac{cn\epsilon_0}{2}I_{\mathrm{LO}}(S_s(\omega-\omega_{\mathrm{LO}}) + S_s(\omega+\omega_{\mathrm{LO}})). \end{aligned} \tag{4.42}$$

The last two terms in equation 4.42 correspond to the shifted spectra which are centered at $\pm 10\,\mathrm{MHz}$. In our experimental analysis, we look at the shifted spectra at $+10\,\mathrm{MHz}$. The frequency of the local oscillator ω_{LO} is chosen such that the shifted spectrum $S_s(\omega - \omega_{\mathrm{LO}})$ has no overlap with the other terms in equation 4.42 in the frequency domain.

Die approbierte gedruckte Originalversion dieser Dissertation ist an der TU Wien Bibliothek verfügbar.
The approved original version of this doctoral thesis is available in print at TU Wien Bibliothek.
TU Bibliothek Your knowledge hub WIEN

CHAPTER 5

Ground state cooling of atoms 300 nm away from a nanofiber

With applications ranging from high precision spectroscopy to quantum simulation, atom cooling is an enabling technique which has pushed the frontier of quantum science since its invention [53–56]. For free-space atom traps, various schemes, e.g., Sisyphus cooling and Raman sideband cooling, have been realized to cool atoms down to sub-Doppler temperature and into the motional ground state of the trapping potential. In the past decade, nanophotonic-based cold atom traps have emerged to realize efficient coupling between light and atoms.

However, cooling atoms at sub-wavelength distances away from the nanophotonic structure presents different challenges compared to free-space setups. First, the atoms' motional degrees of freedom (DOF) are coupled to the mechanical modes of the nanophotonic structure, resulting in orders of magnitude higher heating rate in nanophotonic-based traps than comparable free-space optical traps [57]. Moreover, the excitation light in atom cooling schemes produces stray light by scattering off the nanophotonic structures. The stray light can interfere with the excitation light, thereby introducing unwanted polarization or intensity variations at the atom positions and reducing the efficiency of cooling. One of the previous results in this context is the microwave sideband cooling of nanofiber-trapped atoms [58]. Using this technique, atoms can be cooled close to the motional ground state of the y (azimuthal) DOF. In addition, the heating rate along the y DOF can be measured. However, thus far, this cooling scheme is limited to one DOF since simultaneously cooling the x (radial) and z (axial) DOF have not been realized. As a consequence, microwave sideband cooling in the y DOF does not extend the trapping lifetime since atoms can be heated out via the two other motional DOF, as experimentally observed in [58]. In another work, Raman sideband cooling of the x DOF was employed [59]. While it was observed that the trapping lifetime was extended in this scheme, the average motional quantum number in the x DOF remained significantly above 1.

The discussion in this chapter closely follows the published manuscript [60]. In this chapter, we demonstrate degenerate Raman cooling (DRC) of nanofiber-trapped atoms in all three DOF close to the motional ground states. By cooling the trapped atoms continuously, the trapping

Die approbierte gedruckte Originalversion dieser Dissertation ist an der TU Wien Bibliothek verfügbar.
The approved original version of this doctoral thesis is available in print at TU Wien Bibliothek.
TU Bibliothek Your knowledge hub WIEN

lifetime becomes limited by background gas collisions and increases ∼20-fold compared to the passive lifetime. Finally, we perform heterodyne fluorescence spectroscopy to extract the temperature of atoms.

5.1 Principle of degenerate Raman cooling

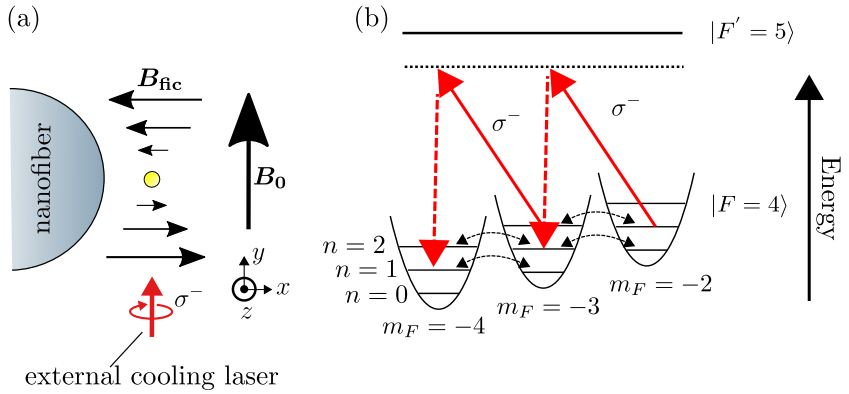

Figure 5.1: Schematic diagram for DRC. (a) Fictitious magnetic field $\boldsymbol{B}_{\text{fic}}$ near the nanofiber-trapped atom (yellow circle). We approximate $\boldsymbol{B}_{\text{fic}}$ as a field which points parallel to $\hat{x}$ and varies along the y-coordinate. The gradient of $\boldsymbol{B}_{\text{fic}}$ enables coupling between spin and motional DOF of the trapped atoms. In the DRC scheme, the excitation light field or the cooling laser is σ^- polarized and propagates in the $+y$ direction. The offset magnetic field $\boldsymbol{B}_0$ is orientated in the $+y$ direction and its magnitude is adjusted such that the energy splitting between the adjacent Zeeman substates is close to one motional quantum. (b) In a cooling cycle, the atoms in the lower Zeeman substates can lose one motional quantum in exchange for a higher Zeeman state due to spin-motion coupling. The cooling light (red arrows) then pumps the atoms to energetically lower Zeeman substates while mostly preserving their motional states, resulting in a loss of one motional quantum in a cooling cycle.

First, we explain the experimental scheme for DRC. The trapping configuration used for DRC is detailed in chapter 2. We show the schematic diagram for DRC of the nanofiber-trapped atoms in Fig. 5.1. As shown in chapter 2, the tight confinement of nanofiber-guided trapping light gives rise to the coupling between spin and motional DOF. For simplicity, we first consider only the y motional DOF. Near the trap minimum, we can approximate $\boldsymbol{B}_{\text{fict}}$ as a linearly gradient which its magnitude varies along y and direction points along the x-axis. The magnitude of the gradient changes its sign at $y = 0$, i.e., the position of the trapped atom. We apply an offset magnetic field $\boldsymbol{B_0} = B_0\hat{\boldsymbol{e}}_{\boldsymbol{y}}$ along the y-axis such that the states $|m_F = -4, n\rangle$ and $|m_F = -3, n-1\rangle$ are close to be energy degenerate. The resulting Hamiltonian is (see equation 3.6 in chapter 2):

$$\hat{H} = \hbar\omega_y\hat{a}_y\hat{a}_y + \hbar\alpha_F B_0\hat{F}_y + \hbar\frac{\Omega_y}{2}(\hat{a}_y + \hat{a}_y^\dagger)(\hat{F}_+ + \hat{F}_-). \tag{5.1}$$

Die approbierte gedruckte Originalversion dieser Dissertation ist an der TU Wien Bibliothek verfügbar.
The approved original version of this doctoral thesis is available in print at TU Wien Bibliothek.
TU Bibliothek Your knowledge hub WIEN

The spin-motion coupling term $\hbar\frac{\Omega_y}{2}(\hat{a}_y + \hat{a}_y^\dagger)(\hat{F}_+ + \hat{F}_-)$ enables us to control the y motional DOF through manipulation of the internal spin DOF. For our trap configuration, we expect the coupling strength $\Omega_y = 2\pi \times 12$ kHz (see chapter 3). By multiplying out this term, we have $\hbar\frac{\Omega_y}{2}(\hat{a}_y\hat{F}_+ + \hat{a}_y^\dagger\hat{F}_- + \hat{a}_y\hat{F}_- + \hat{a}_y^\dagger\hat{F}_+)$. The terms $\hat{a}_y\hat{F}_+$ and $\hat{a}_y^\dagger\hat{F}_-$ cause atom to precess between adjacent Zeeman states while conserving the number of excitations. As the atom goes to a higher (lower) Zeeman state, one quantum in y-motional DOF is removed (added). Hence, the states $|m_F = -4, n\rangle$ and $|m_F = -3, n-1\rangle$ are coupled. Both $\hat{a}_y\hat{F}_-$ and $\hat{a}_y^\dagger\hat{F}_+$ are the counter-rotating terms. Their effects can be neglected since they are far-off resonant and the coupling strength is small compared to ω_y and $\alpha_F B_0$.

To achieve cooling, we utilize a σ^- polarized light field that is near-resonant to the D_2 cycling transition ($6^2S_{1/2}, F = 4 \rightarrow 6^2P_{3/2}, F' = 5$) to pump atoms to the lower Zeeman sub-states continuously. We denote it as the cooling laser or the excitation light field. The excitation light field can either propagate in free space or be guided by the nanofiber. In the former case, the excitation light field propagates in the $+y$ direction and impinges on the trapped atoms, see panel (a) in Fig. 5.1. We approximate the external light field as a Gaussian beam. The $1/e^2$-diameter of this light field is $1.4\,\mathrm{mm}$, which is enough to cover the entire region of the trapped atoms. In the latter case, the nanofiber-guided light field is quasi-linearly polarized along x-axis and its local polarization on one side of the nanofiber is predominantly σ^-. Thus the nanofiber-guided light acts as the cooling light for atoms on one side of the nanofiber. Using an *ab initio* calculation with the experimental parameters, the trap frequency in the x, y, z motional DOF are expected to be $\{\omega_x, \omega_y, \omega_z\}/2\pi = \{136, 83, 215\}$ kHz. Since the excitation light's photon has a recoil frequency of $\sim$2 kHz, two orders of magnitude lower than the calculated trap frequencies, the nanofiber-trapped atoms are in the Lamb-Dicke regime where optical pumping is likely to preserve their motional states. Without considering heating, most atoms accumulate in $|m_F = -4, n = 0\rangle$ at the end of the cooling process. The state $|m_F = -4, n = 0\rangle$ is not resonantly coupled to other states through the spin-motion coupling.

DRC in the two other DOF follows a similar idea (see chapter 3). For the x DOF, we rely on the higher-order expansion of the fictitious magnetic field gradient. For the z DOF, we rely on the fictitious magnetic field gradient along the z-axis which originates from the relative alignment between the two counterpropagating red-detuned trapping light fields. Together, we have a Hamiltonian which includes coupling between spin DOF and all three motional DOF:

$$\hat{H} = \sum_{i=x,y,z} \hbar\omega_i\hat{a}_i^\dagger\hat{a}_i + \hbar\alpha_F B_0\hat{F}_y - \hbar\frac{\Omega_y}{2}(\hat{a}_y + \hat{a}_y^\dagger)(\hat{F}_+ + \hat{F}_-) + \hbar\frac{\Omega_{xy}}{2}(\hat{a}_x + \hat{a}_x^\dagger)(\hat{a}_y + \hat{a}_y^\dagger)(\hat{F}_+ + \hat{F}_-) + \hbar\frac{i\Omega_z}{2}(\hat{a}_z + i\hat{a}_z^\dagger)(\hat{F}_- - \hat{F}_+). \quad (5.2)$$

The Ω_{xy} term has two effects: First, it can remove (add) one quantum of motional energy in the x and y DOF as the atom goes to a higher (lower) Zeeman state. Second, it can exchange one quantum between x and y DOF as the atom goes to a different Zeeman state. Both mechanisms can enable cooling in the x DOF. We expect $\Omega_{xy} = 2\pi \times 0.56$ kHz for our trap configuration. The Ω_z term behaves similarly to the Ω_y term and removes (adds) one quantum from the z motional DOF as the atom goes to a higher (lower) Zeeman state. We expect Ω_z to be significant when

Die approbierte gedruckte Originalversion dieser Dissertation ist an der TU Wien Bibliothek verfügbar.
The approved original version of this doctoral thesis is available in print at TU Wien Bibliothek.
TU Bibliothek Your knowledge hub WIEN

there's a small angle $\theta_{cp,red}$ between the polarization axes of the two counter-propagating red-detuned trapping light fields, e.g., $\Omega_z = 2\pi \times 1.4$ kHz when $\theta_{cp,red} = 5°$. Since the resonance conditions for these spin-motion coupling terms are all different from each other, the magnitude of B_0 plays an important role in optimizing the DRC for different DOF. We experimentally examine the dependency of DRC on B_0 in sections 5.4 and 5.5.

5.2 Experimental procedure

In a typical experimental sequence, we first perform molasses cooling on the nanofiber-trapped atoms at zero offset magnetic field. This procedure initializes the temperature of the trapped atoms. We measure the extinction of a weak nanofiber-guided light field on the cycling transition of the D_2 line. We denote this light field as the probe light. The probe light is quasi-linear polarized along the x-axis. Assuming the extinction per atom is a constant value at a given temperature, the extinction of the probe light is proportional the initial atom number, N_0. To perform DRC, we ramp up the offset magnetic field to a fixed value and turn on the cooling laser for a time duration. After DRC, We measure again the extinction of the probe light which is proportional to the final atom number, N_{at}. The ratio N_0/N_{at}, namely the normalized atom number, is the fraction of the atoms survived during DRC. We can make this measurement at either a zero offset magnetic field or a relatively high magnetic field, i.e., 10 to 20 G. In the latter case, the probe light, with its opposite polarization of σ^- and σ^+ on the two sides of the nanofiber, optically pumps the two diametric arrays of the trapped atoms into the two opposite outermost Zeeman substates. By measuring the extinction in a high magnetic field, the atoms in $|F = 4, m_F = -4\rangle$ and $|F = 4, m_F = +-4\rangle$ can be distinguished since their transition frequencies are separated by Zeeman splitting, i.e., the frequency difference between the $F = 4, m_F = -4 \rightarrow F^{'} = 5, m_F^{'} = -5$ transition and to the $F = 4, m_F = 4 \rightarrow F^{'} = 5, m_F^{'} = 5$ transition. This procedure enables us to measure the percentage of atoms survived after DRC on each side of the nanofiber separately, see section 5.6.

5.3 Trapping lifetime during degenerate Raman cooling

We observe the first sign of cooling by measuring the lifetime of the trapped atoms, see Fig. 5.2. Here we measure N_{at}/N_0 as a function of the cooling time. For comparison, we also measure the passive trapping lifetime without DRC. We fit all measurements with an exponential function to infer the $1/e$ time constant which is defined as the trapping lifetime. Without cooling (red squares), we find the trapping lifetime to be $\tau_{\text{ref}} = 75(1)\,\text{ms}$. When we apply DRC with an external light field as the cooling laser (blue circles), the trapping lifetime increases drastically to $\tau_{\text{DRC}}^{\text{ext}} = 1650(20)\,\text{ms}$. Similarly, we also determine the trapping lifetime during DRC using a nanofiber-guided cooling light field, which yields a value of $\tau_{\text{DRC}}^{\text{ext}} = 1750(30)\,\text{ms}$. Both measurements with DRC reach the limit of lifetime imposed by collisions with the background gas in the vacuum chamber. This is supported by an additional atom lifetime measurement in the presence of a three-dimensional polarization gradient cooling (PGC) at zero B_{off} (red triangle), which yields $\tau_{\text{PGC}} = 1560(20)\,\text{ms}$, in reasonable agreement with the lifetimes measured

Die approbierte gedruckte Originalversion dieser Dissertation ist an der TU Wien Bibliothek verfügbar.
The approved original version of this doctoral thesis is available in print at TU Wien Bibliothek.
TU Bibliothek Your knowledge hub WIEN

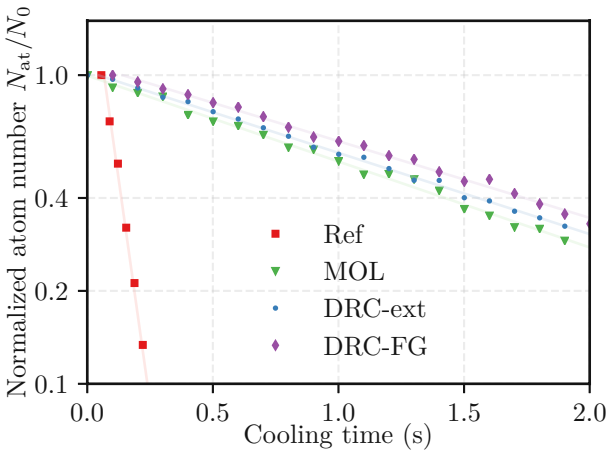

Figure 5.2: Normalized number of trapped atoms measured after a variable time, in the absence of cooling (red squares), with DRC using an external (blue circles) or a nanofiber-guided (purple diamonds) laser field, and with optical molasses (green triangles). The solid lines correspond to exponential fits.

during DRC. The difference between τ_{PGC} and $\tau_{\mathrm{DRC}}^{\mathrm{ext}}$ can be explained by the fluctuation of the background gas density and its associated collision-limited trapping lifetime.

The significant increase of lifetime during DRC indicates that this technique is efficient to counteract heating mechanism for all 3 motional DOF in the nanofiber-based atom trap. The various heating mechanisms are discussed in the appendix 9.1. Furthermore, it was shown in previous work that cooling in one dimension, namely the y motional DOF, does not extend the trapping lifetime [58]. This indicates that possible coupling between different motional DOF, i.e., resulting from the nonseparability of the trapping potential, is not sufficient to explain the increase of the trapping lifetime. Therefore, the increased trapping lifetime during DRC is the first indication that all three motional DOF are directly cooled in our method. The measurements with DRC are performed at an offset magnetic field $B_0 = 0.5\,\mathrm{G}$. The measurement using an external light field is performed with a peak intensity of $I_0 = 4.1\,I_{\mathrm{sat}}$ and a detuning of $-12\,\Gamma$, where I_{sat} and Γ denote the saturation intensity and natural linewidth of the D_2 cycling transition of cesium, respectively. The measurement using a nanofiber-guided light field is performed with an intensity of $I_0 = 0.2\,I_{\mathrm{sat}}$ at the positions of the atoms and a detuning of $-6.5\,\Gamma$.

Die approbierte gedruckte Originalversion dieser Dissertation ist an der TU Wien Bibliothek verfügbar.
The approved original version of this doctoral thesis is available in print at TU Wien Bibliothek.
TU Bibliothek Your knowledge hub WIEN

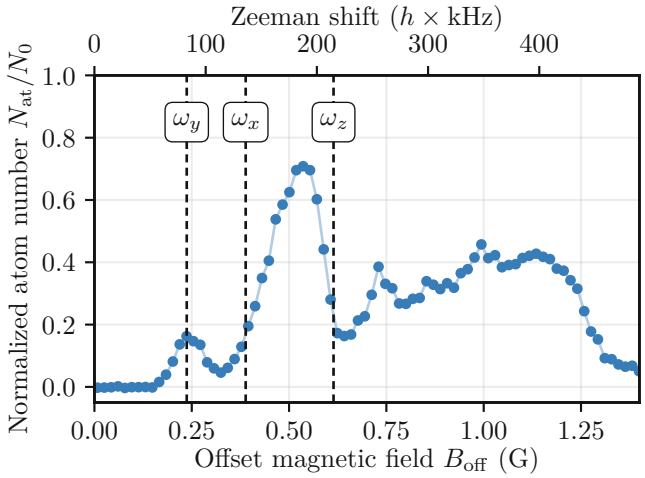

Figure 5.3: Normalized number of remaining atoms that are trapped after 500 ms of DRC as a function of B_0. The top x-axis ticks correspond to the frequency splitting between two adjacent Zeeman substates at a given B_0. We indicate the B_0 where the energy of one spin excitation matches one excitation in the y (azimuthal), x (radial), z (axial) DOF with the vertical dashed lines.

5.4 Optimization of degenerate Raman cooling based on minimizing atom loss

We now study the trapping lifetime during DRC at various B_0, shown in Fig. 5.3. The energy of one spin excitation is given by the energy splitting between the adjacent Zeeman substates in the presence of the offset magnetic field. Therefore, B_0 determines the detuning from various resonant conditions of couplings between spin and motional DOF, see equation 5.2. We measure N_{at}/N_0 as a function of B_0 for 500 ms of DRC. For reference, N_{at}/N_0 with 500 ms of waiting time is ~ 0.1 % based on the trapping lifetime measured without any cooling.

We observe pronounced local maxima which correspond to optimal combinations of cooling rates in three motional DOF. The first local maximum appears at $B_0 \approx 0.25$ G, corresponds to the resonance condition given by the simple spin-coupling model given by equation 5.1, where one excitation of the y motional DOF and one spin excitation are exchanged. The expected position of this resonance is ω_y, and is indicated by the leftmost vertical dashed line in Fig. 5.3. We use two additional vertical dashed lines to indicate the expected B_0 where the energy of one spin excitation matches one motional excitation in the x and z DOF, respectively.

To achieve efficient DRC, we systematically examine the effect of the cooling laser's parameters, i.e., power and frequency, on the trapping lifetime. In Fig. 5.4(a), we show for three different laser powers, the normalized number of atoms after 80 ms of DRC as a function of the laser detuning. The measurement is done in an offset magnetic field of 0.5 G and with an external cooling laser. For reference, we indicate the fraction of atoms left in the absence of DRC with a horizontal dashed black line. Furthermore, we do a finer scan of the cooling laser power

Die approbierte gedruckte Originalversion dieser Dissertation ist an der TU Wien Bibliothek verfügbar.
The approved original version of this doctoral thesis is available in print at TU Wien Bibliothek.
TU Bibliothek Your knowledge hub WIEN

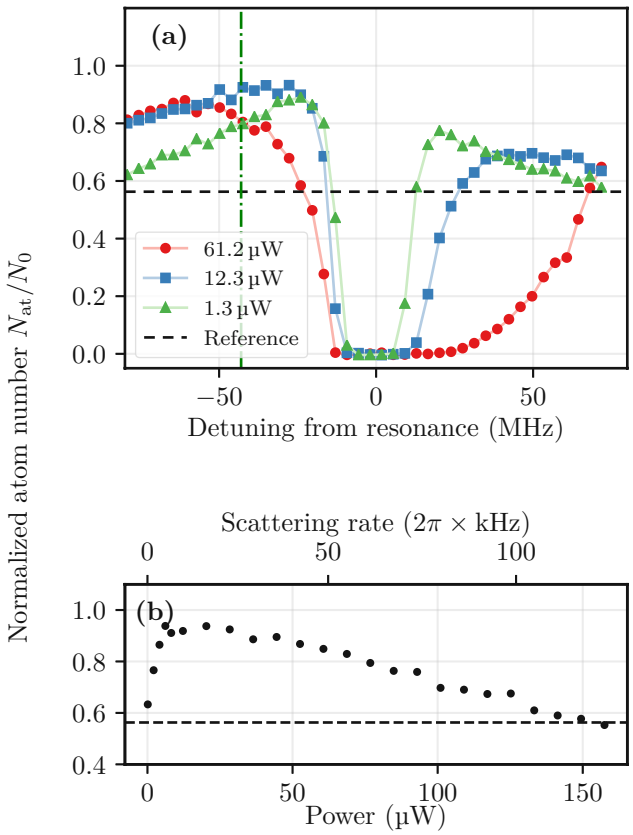

Figure 5.4: (a) Normalized number of atoms remaining in the trap after 80 ms of DRC for various detunings of the external cooling laser field. Negative (positive) detuning values correspond to a red (blue) detuning of the laser field with respect to the $(6S_{1/2}, F = 4) \rightarrow (6P_{3/2}, F' = 5)$ optical transition of the trapped cesium atoms. We repeat this measurement for different power of the external cooling laser, $P_0 = 61.2\,\mu\text{W}$ (red circles), $12.3\,\mu\text{W}$ (blue squares) and $1.3\,\mu\text{W}$ (green triangles), which correspond to peak intensities of $I_0/I_{\text{sat}} = 6.8$, 1.4 and 0.14, respectively. The horizontal black dashed line indicates the fraction of atoms remaining in the trap in the absence of DRC. (b) Normalized number of atoms remaining in the trap as a function of the cooling laser power. The top secondary x-axis indicates the expected scattering rate γ_0 for the outermost cycling transition $F = 4, m_F = -4 \rightarrow F' = 5, m_F = -5$. The measurement is taken after 80 ms of DRC and at a detuning of $-9.4\,\Gamma$ (same detuning is indicated by the vertical dash-dotted line in panel (a)). The number of atoms remaining is maximized for a power of about $15\,\mu\text{W}$ or $I_0 = 1.7\,I_{\text{sat}}$. This power corresponds to $\gamma_0 = 2\pi \times 12$ kHz, which is on the same order of magnitude as the coupling strength Ω_y.

Die approbierte gedruckte Originalversion dieser Dissertation ist an der TU Wien Bibliothek verfügbar.
The approved original version of this doctoral thesis is available in print at TU Wien Bibliothek.
TU Bibliothek Your knowledge hub WIEN

while fixing its frequency, shown in Fig. 5.4(b). We can identify two limiting regimes: At a low power or a large detuning, the scattering rate is reduced along with the cooling efficiency. On the other hand, at a high power or small detuning, the large scattering rate can have two detrimental effects on cooling. First, it leads to a high recoil heating rate which counteracts the cooling. Second, the excessive power of the cooling laser interrupts the coherent exchange between the spin and motional quanta and thereby the cooling cycle. At this limit, the DRC scheme can even lead to significant heating and atom losses.

A more subtle effect comes from the Zeeman-state-dependent ac Stark shift induced by the cooling laser. At a higher laser power or frequency closer to the atomic resonance, the cooling laser can induce significant vector light shift and modify the energy difference between the adjacent Zeeman states or the energy of one spin excitation. Moreover, depending on the laser detuning, the ac Stark shift can either increase or decrease one spin excitation's energy, thereby altering the DRC resonance condition. This is evident by the asymmetry of the cooling efficiency at positive and negative detuning in Fig. 5.4(a).

5.5 Heterodyne fluorescence spectroscopy during degenerate Raman cooling

To obtain more quantitative information on the atoms' temperature, we measure the fluorescence spectrum using a heterodyne detection scheme while performing DRC [42, 52, 61]. Under the illumination of an external cooling laser, a fraction of the light scattered by the atoms is coupled into the nanofiber-guided mode. This light is then guided to a beam splitter, where it is ~~combined~~ with a reference laser field which acts as a local oscillator. To suppress relative frequency drifts, we derive the reference laser field from the cooling laser itself with a non-~~polarization~~ beamsplitter and shift its frequency by $10\,\mathrm{MHz}$ using a pair of acoustic optical modulators. We detect the combined light field with an SPCM. As shown in section 4.5, the auto-correlation of the intensity of the combined light field can be used to calculate the effective power spectrum. Following this recipe, we analyze the SPCM signal and compute the power spectrum of the atom-scattered light field. To improve the signal to noise ratio of the spectra, we apply the Welch method with $1\,\mathrm{ms}$ window to the SPCM signal before the Fourier transformation. In the Welch method, the signal is split up into overlapping segments of $1\,\mathrm{ms}$ window. After discrete Fourier transformation, we average the squared magnitude of the computed result over all segments.

When the excitation laser power is far below the saturation intensity, the population in the excited state is negligible, and the scattering process is mostly coherent. This means the spectrum of the scattered light is much narrower than the atomic linewidth. The width of the sidebands then depends on the combination of the depopulation rates of the states (see chapter 4), the anharmonicity and the homogeneity of the trapping potential. The motion of the atoms in the 3D trapping potential modulates the scattered light field, and gives rise to sidebands at the trap frequencies, see Fig. 5.5. We can estimate the atomic ensemble's temperature based on the ratio of the areas of the sidebands. The mean number of motional state excitation is given by $\langle n_i \rangle = S^i_{-1}/(S^i_{+1} - S^i_{-1})$, where $S^i_{\pm 1}$ is the area of the sideband corresponding to the transition $n \to n \pm 1$ in i DOF (see chapter 4).

Die approbierte gedruckte Originalversion dieser Dissertation ist an der TU Wien Bibliothek verfügbar.
The approved original version of this doctoral thesis is available in print at TU Wien Bibliothek.
TU Bibliothek Your knowledge hub WIEN

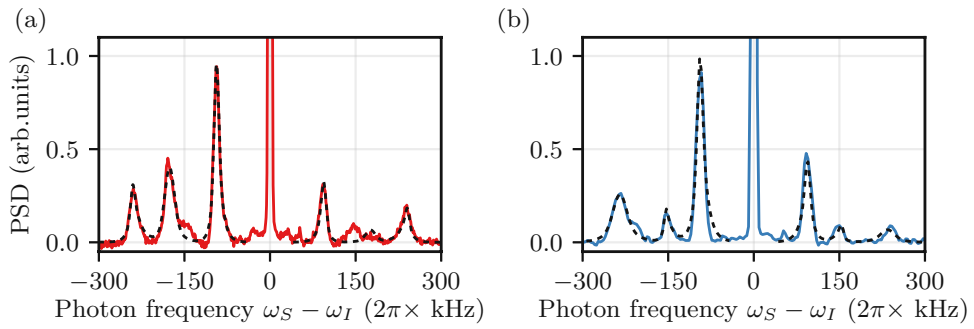

Figure 5.5: Fluorescence spectrum during DRC. (a) Power Spectral Density (PSD) of the SPCM signal for an offset magnetic field of 0.34 G (b) PSD of the SPCM signal for an offset magnetic field of 0.51 G. The frequency axis in both panel is defined relative to the central beat note in the heterodyne measurement (see 4.5 for details). The atoms are illuminated for 200 ms with an intensity $I \approx 14\, I_{\mathrm{sat}}$ and a detuning of $-12\,\Gamma$ during each experimental cycle. For each realization, we obtain the PSD from a windowed Fourier transform of the SPCM signal (Welch method, 1 ms window). Both spectra are averaged over 6000 experimental realizations. The dashed black lines correspond to fits of the experimental data, see main text for the fit model. From the fits, we extract mean numbers of excitations of (a) $\{\langle n_x\rangle, \langle n_y\rangle, \langle n_z\rangle\} = \{0.20(2), 0.52(2), 1.47(8)\}$ and (b) $\{\langle n_x\rangle, \langle n_y\rangle, \langle n_z\rangle\} = \{1.2(3), 0.78(4), 0.36(8)\}$, indicating that all motional DOF can be cooled close to the ground state.

The fitted spectra are shown in Fig. 5.5(a) and (b). In panel (b), the fit yields trap frequencies $\{\omega_x, \omega_y, \omega_y\}/2\pi = \{154, 94, 231\}$ kHz, which agree with our *ab initio* calculation within 10%. From the widths of the fitted sidebands, we determine the upper limit of about 10 % for the inhomogeneity of the trapping frequencies in different sites along the nanofiber. The clear asymmetry of the Stokes and anti-Stokes sidebands in Fig. 5.5(a) and (b) indicates significant ground-state occupations. The spectrum shown in Fig. 5.5(a) corresponds to an offset magnetic field of $B_{\mathrm{off}} = 0.34$ G. Our fit yields $\{\langle n_x\rangle, \langle n_y\rangle, \langle n_z\rangle\} = \{0.20(2), 0.52(2), 1.47(8)\}$, which corresponds to ground states occupations of $\{83\,\%, 66\,\%, 40\,\%\}$ for the x, y, and z motional DOF, respectively. We can more efficiently cool the z motional DOF by changing the offset magnetic field closer to the resonance condition for the direct exchange between one spin excitation and one excitation in the z DOF. For this reason, we record another spectrum at $B_{\mathrm{off}} = 0.51$ G (see Fig. 5.5(b)), which yields a mean number of excitations of $\langle n_z\rangle = 0.36(8)$, corresponding to a ground-state occupation of 74 %. For the other motional DOF, we then find $\{\langle n_x\rangle, \langle n_y\rangle\} = \{1.2(3), 0.78(4)\}$.

To extract the sideband amplitude, we fit the acquired spectra using a model based on second order perturbation and rate-equation approach [42, 45]. In our model, the florescence spectrum $S(\omega)$ is given by summing the contributions of all $n \to n \pm 1$ processes in all motional DOF. The width of the spectral contribution from the transition between motional states n and $n+1$ in the i DOF is given by the decay rate of the states coherence, $\Gamma^i_{n,n+1}$:

Die approbierte gedruckte Originalversion dieser Dissertation ist an der TU Wien Bibliothek verfügbar.
The approved original version of this doctoral thesis is available in print at TU Wien Bibliothek.
TU Bibliothek Your knowledge hub WIEN

$$\Gamma^i_{n,n+1} = (\Gamma^i_n + \Gamma^i_{n+1})/2 = \Gamma^i_0(n+1), \tag{5.3}$$

where Γ^i_n is the depopulation rate of the motional state n.

For our model, we add different contributions incoherently to obtain the spectrum:

$$S(\omega) = \sum_{i=x,y,z} \sum_{n=0}^{+\infty} \{\pi^i_n \gamma^i_{n+1\to n} \frac{\Gamma^i_{n,n+1}/(2\pi)}{(\omega+\omega_i)^2 + (\Gamma^i_{n,n+1}/2)^2} + \pi_{n+1}\gamma^i_{n\to n+1} \frac{\Gamma^i_{n,n+1}/(2\pi)}{(\omega-\omega_i)^2 + (\Gamma^i_{n,n+1}/2)^2}\} + C_{\text{off}}, \tag{5.4}$$

where π^i_n is the population of the motional state n, $\gamma^i_{n_i,n_f}$ is the rate of transition between motional states n_i and n_f, C_{off} is an constant offset to account for the background signal.

We assume a thermal distribution of the motional states: $\pi^i_n = (1-q_i)q_i^n$, with $q_i = \exp(-\hbar\omega_i/(k_{\text{B}}T_i))$, where T_i is the temperature in the i DOF and and k_{B} is the Boltzmann's constant.

The rates $\gamma^i_{n\to n+1}$ and $\gamma^i_{n+1\to n}$ are given by:

$$\gamma^i_{n\to n+1} = \gamma^i_{n+1\to n} = (\Delta k_{\text{i}} i_0)^2 (n+1)\frac{\gamma_s}{4\pi}\delta\Omega, \tag{5.5}$$

where $\delta\Omega/(4\pi)$ is the percentage of the emitted light that are coupled to the nanofiber-guided mode, γ_s is the total scattering rate of the atom, Δk_i is the change of the wave vector in the scattering process along i-axis, i_0 is the root mean square size of the motional ground state in the i DOF.

Due to the moving time window used to compute the power spectral density from the SPCM data, the profile of each spectral contribution is closer to a Gaussian function rather than a Lorentzian function. Hence, we use Gaussian function for the fit. In addition, we introduce a new fit parameter $\xi_i = \xi_{\text{det}}(\Delta k_{\text{i}} i_0)^2 \delta\Omega\gamma_s/(4\pi)$, where ξ_{det} is the detection efficiency. The fit function can be written as follow:

$$S(\omega) = \sum_{i=x,y,z} \xi_i(1-q_i) \sum_{n=0}^{+\infty} q_i^n \frac{2}{\Gamma^i_0}\sqrt{\frac{\ln 2}{\pi}}\{\exp(-\frac{(\omega-\omega_i(n))^2}{(\Gamma^i_0(n+1))^2/(4\ln(2))}) + q_i\exp(-\frac{(\omega+\omega_i(n))^2}{(\Gamma^i_0(n+1))^2)/(4\ln(2))})\} + C_{\text{off}}, \tag{5.6}$$

where $\omega_i(n)$ is the trap frequency that has a dependency on n. This accounts for the trap anharmonicity which is modeled by $\omega_i(n) = (E_{n+1} - E_n)/\hbar = \omega^i_0(1+e_1+e_2(2n+1))/(1+e_1+e_2)$, where e_1 and e_2 are two constant coefficients obtained from *ab initio* simulation, $\omega^i_0\hbar$ is the energy difference between $n=0$ to $n=1$ in the i DOF.

The fit parameters include $\omega^i_0, q_i, \Gamma^i_0, \xi_i$ for $i = \{x,y,z\}$. Moreover, the global offset C_{off} is used as a free parameter to account for the background signal. The mean number of motional quanta in the i DOF is given by $\langle n_i\rangle = q_i/(1-q_i)$.

Die approbierte gedruckte Originalversion dieser Dissertation ist an der TU Wien Bibliothek verfügbar.
The approved original version of this doctoral thesis is available in print at TU Wien Bibliothek.
TU Bibliothek Your knowledge hub WIEN

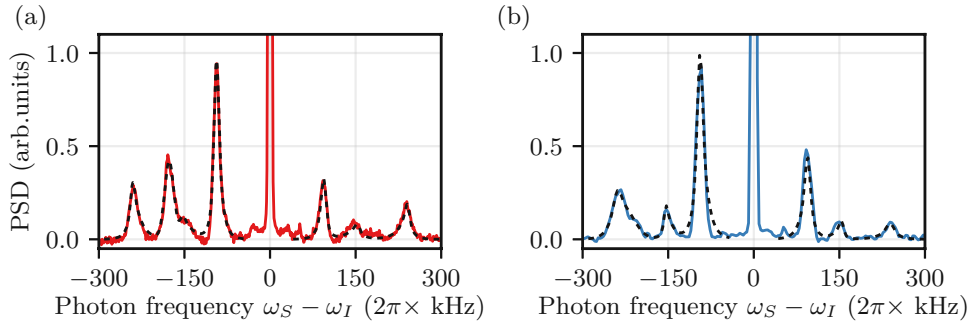

Figure 5.6: Fluorescence spectrum during DRC. (a) PSD of the SPCM signal for an offset magnetic field of 0.34 G. (b) PSD of the SPCM signal for an offset magnetic field of 0.51 G. The dashed black lines in both panels present fit which account for an additional m_F-changing transition. From the fits, we extract mean numbers of excitations of $\{\langle n_x\rangle, \langle n_y\rangle, \langle n_z\rangle\} = \{1.85(7), 0.51(1), 1.62(3)\}$ for panel (a) and $\{\langle n_x\rangle, \langle n_y\rangle, \langle n_z\rangle\} = \{1.3(2), 0.80(3), 0.9(2)\}$ for panel (b).

A shortcoming of this model is that the transitions between adjacent Zeeman substates are not taken into account. For example, a two-photon transition could occur between $|F = 4, m_F = -3\rangle$ and $|F = 4, m_F = -4\rangle$, where the first and second photon have π and σ^- polarization, respectively. This transition is not available if the excitation light field has a purely σ^- polarization. However, due to experimental imperfections, i.e., imperfect optical alignment, a small portion of the π polarization in the excitation light field could result in an m_F-changing transition that has a comparable signal intensity with the motional sidebands. The Zeeman splittings for the setting of the two spectra in Fig. 5.5 are at 105 kHz and 175 kHz, respectively. Therefore the m_F-changing transition has a frequency close to the x motional sidebands in Fig. 5.5(a) and the y motional sidebands in Fig. 5.5(b). To check its effect, we extract Δk_i for the i motional DOF, where Δk_i is the difference between the i component of the wavevector of the incident photon and the scattered photon. We expect Δk_i to be constant for all spectra since the experimental geometry is fixed. As shown in section 4.2, the ratio between the areas corresponding to the two first-order sidebands transitions $S^i_{\Delta 1} + S^i_{\Delta -1}$ and to the carrier transition S_0 is proportional $(\Delta k_i)^2$:

$$\frac{S^i_{\Delta 1} + S^i_{\Delta -1}}{S_0} = (2\langle n_i\rangle + 1)\Delta k_i^2 {i_0}^2, \tag{5.7}$$

where S_0 is the area corresponding to the carrier transition.

With equation 5.7, we can extract Δk_i from the data in Fig. 5.5(a) and (b), resulting in $\{\Delta k_x, \Delta k_y, \Delta k_z\} = \{8(2), 8.9(2), 7.3(3)\}$ µm^{-1} and $\{\Delta k_x, \Delta k_y, \Delta k_z\} = \{4.1(8), 9.0(4), 12(2)\}$ µm^{-1}, respectively. While the values of Δk_y in the two datasets agree within the error, the values of Δk_x and Δk_z differ by a factor of $\sim$2. We attribute this discrepancy to the addition of the m_F-changing transition near the x motional sidebands in Fig. 5.5(a) and the y motional sidebands in Fig. 5.5(b).

Die approbierte gedruckte Originalversion dieser Dissertation ist an der TU Wien Bibliothek verfügbar.
The approved original version of this doctoral thesis is available in print at TU Wien Bibliothek.
TU Bibliothek Your knowledge hub WIEN

The $|F = 4, m_{\mathrm{F}} = -3\rangle \rightarrow |F = 4, m_{\mathrm{F}} = -4\rangle$ transition has a lower emitted photon energy compared to the incoming photon energy, thereby this transition would appear on the red side ($\omega_S - \omega_I < 0$) of the spectra and exaggerates the asymmetry of the observed spectra. The amplitude of the Zeeman changing transition depends on the polarization of the excitation beam and the distribution of Zeeman substates. To account for this transition, we include in our fit model an additional Gaussian function that has three fit parameters, ω_{ze}, γ_{ze} , A_{ze}, corresponding to the center position, width and the height of the Gaussian function, respectively. Furthermore, to restrict the number of free parameters for a more robust fit, we fix Δk_i using our previous fit shown in Fig. 5.5. When the m_F-changing transition is near a motional sideband, we take Δk_i from an different dataset where the m_F-changing transition is close to a different motional sideband. For example, for Fig. 5.5(a), the m_F-changing transition is close to the x DOF. We then use Δk_x extracted from the fit shown in Fig. 5.5(b) where the m_F-changing transition is close to the z motional sidebands. We show this fit in Fig. 5.6. The fit yields $\{\langle n_x\rangle, \langle n_y\rangle, \langle n_z\rangle\} = \{1.85(7), 0.51(1), 1.62(3)\}$ for panel (a) and $\{\langle n_x\rangle, \langle n_y\rangle, \langle n_z\rangle\} = \{1.3(2), 0.80(3), 0.9(2)\}$ for panel (b). These mean numbers of motional quanta are higher than what was found in the previous analysis. Nevertheless, they still indicate atoms are close to the ground states in all 3 motional DOF.

We now discuss possible mechanisms that can limit the performance of DRC scheme, i.e., the final temperature of the trapped atoms. The final temperature or the mean number of motional quanta is measured in a stationary state where the heating rate matches the cooling rate. For a fixed trapping configuration, the cooling rate depends on the power and detuning of the cooling laser (see Fig. 5.4) and on the amplitude of the offset magnetic field (see Fig. 5.3). In general, the upper limit of the cooling rate is set by the rate of spin-motion coupling at the chosen magnetic field. There are two types of heating mechanisms during our DRC schemes. The first type of heating comes from the optomechanical coupling of the optically trapped atoms to the mechanical modes of the nanofiber [57]. In previous work, the heating rate in the y-direction is measured to be about 0.3 quanta/ms [58]. The second type of heating comes from the DRC scheme itself. Since the cooling laser in our experiment is on an optical cycling transition, there are no optical dark states and the atoms constantly experience recoil heating during DRC. The intensity of the cooling laser field for our fluorescence spectrum measurements is higher than the optimum intensity indicated in the Fig. 5.4(b). We use a larger intensity in order to increase the signal-to-noise in our spectra. The increased recoil heating in this setting suggests that the measured mean numbers of motional quanta correspond to the upper bounds of what can be achieved with the DRC method, e.g., using a light field on a non-cycling transition for cooling.

5.6 Discerning and preparing atoms on only one side of the nanofiber

In our trap configuration, two atomic ensembles are trapped in two diametric lattices of trapping sites around the nanofiber. The two arrays are $\sim 1\,\mu\mathrm{m}$ apart. The trapping light fields can cause state-dependent light shifts that are different on the two sides of the nanofiber, and thereby lead to an inhomogeneous broadening of atomic transitions. For engineering collective interaction between atoms and light, it is often advantageous to reduce such complexity and select atoms

Die approbierte gedruckte Originalversion dieser Dissertation ist an der TU Wien Bibliothek verfügbar.
The approved original version of this doctoral thesis is available in print at TU Wien Bibliothek.
TU Bibliothek Your knowledge hub WIEN

on only one side of the nanofiber. This capability was first demonstrated in previous work by R. Mitsch et al. [24]. A single optical mode is used to pump the two atomic ensembles to opposite Zeeman states simultaneously. At a magnetic field where the Zeeman splitting between these two states is greater than the natural linewidth, the two atomic ensembles can be discerned in their optical spectra. Furthermore, opposite fictitious magnetic fields can be introduced to the two atomic ensembles via modifying the trap configuration. As a result, the locally distinct Zeeman shifts allow one to discern and manipulate the two atom ensembles even when prepared in the same Zeeman substate.

Taking advantage of DRC, we demonstrate an alternative method to select atoms on one side of the nanofiber. As shown in chapter 2, we utilize a nanofiber-guided excitation light field that is quasi-linearly polarized along the x-axis. Its evanescent field is mostly σ^+ polarized on one side of the nanofiber and σ^- polarized on the other side. While the σ^- polarized light facilitates degenerate Raman cooling, the σ^+ polarized light does the opposite, i.e., degenerate Raman heating. As the σ^+ polarized light pumps atoms to a higher Zeeman state, the added energy of the spin DOF can be converted to of motional DOF through the process of spin-motion coupling.

As shown in Fig. 5.7(a), the atoms trapped on opposite sides of the nanofiber overlap with the σ^- and σ^+ components of the evanescent field of a quasi-linearly polarized nanofiber-guided light, respectively. By adding an offset magnetic field between $0.2\,\mathrm{G}$ and $0.5\,\mathrm{G}$ along the $+y$ direction, we achieve cooling of atoms on one side of the nanofiber while simultaneously heating atoms out of their trapping potential the other side. Furthermore, the excitation light field optically pumps the two atomic ensembles into different Zeeman states, enabling us to discern the population of the two ensembles since their optical resonance frequencies now differ by the Zeeman splitting. We ramp the offset magnetic field to $16\,\mathrm{G}$ and measure the transmission spectra of the trapped atoms. To obtain the transmission spectrum, we sweep the frequency of a nanofiber-guided probe light over a $140\,\mathrm{MHz}$ interval or $\sim 27\ \Gamma$. The two spectra in panel (b) and (c) exhibit the structure of two dips. The left dip originates from the extinction of the atomic ensemble on the σ^+ side. These atoms are lost during degenerate Raman heating. Meanwhile, the atomic ensemble on the σ^- side undergoes degenerate Raman cooling and remains trapped.

For a more qualitative result, we measure N_{at}/N_i of the two atomic ensembles as a function of the illumination duration with the excitation light field, see Fig. 5.7(d). The populations of the two atomic ensembles are extracted from the transmission spectrum, e.g., the spectra shown in panel (b) and (c). Here we assume a constant OD per atom. From an exponential fit, the lifetime of the atomic ensemble on the σ^+ side is found to be $2.3\,\mathrm{ms}$, far less than the passive trapping of lifetime $\sim$70 ms.

Die approbierte gedruckte Originalversion dieser Dissertation ist an der TU Wien Bibliothek verfügbar.
The approved original version of this doctoral thesis is available in print at TU Wien Bibliothek.
TU Bibliothek Your knowledge hub WIEN

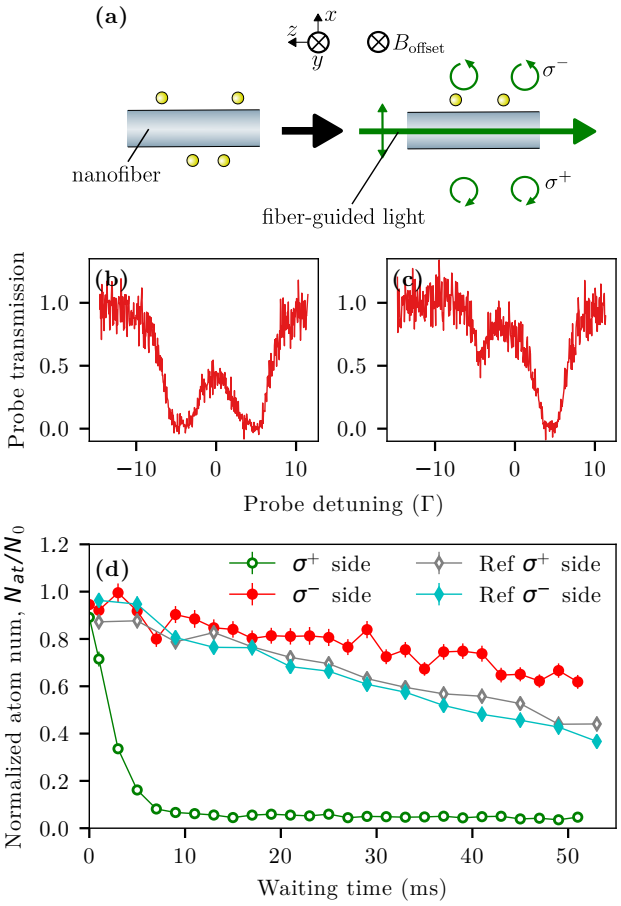

Figure 5.7: Selection of the atomic ensemble trapped on one side of the nanofiber. (a) Schematic diagram for selecting an atomic ensemble on one side of the nanofiber. Using a nanofiber-guided light which is linearly polarized along the x-axis, atoms trapped on one side of the nanofiber undergo degenerate Raman heating and are heated out of the trap. Meanwhile, the atoms on the other side undergo degenerate Raman cooling and remain trapped. (b)-(c) Transmission spectra before and after exciting atoms with 31 ms of the nanofiber-guided light field, respectively. Both spectra are taken at 16 G offset magnetic field along $+y$ direction. For the spectrum shown in panel (b), atoms are trapped on both sides of the nanofiber, whereas atoms are trapped predominantly on one side of the nanofiber in the spectrum in panel (c). The left (right) peak in the spectrum results from the extinction of the guided light by the atomic ensemble on the σ^+ (σ^-) side. (d) Normalized atom number as a function of the time. The number of the atomic ensemble trapped on the σ^+ (σ^-) side is indicated by the hollowed circle (filled circle). In the absence of the nanofiber-guided excitation light, the population of the two atomic ensembles, indicated by the hollowed diamond and blue diamond, respectively, are equal at the various waiting time. It is apparent that the trapping lifetime of atoms on the σ^+ (σ^-) side is far shorter (longer) than the lifetime in the absence of the excitation light field, indicating the presence of degenerate Raman heating and cooling on the two atomic ensembles, respectively.

Die approbierte gedruckte Originalversion dieser Dissertation ist an der TU Wien Bibliothek verfügbar.
The approved original version of this doctoral thesis is available in print at TU Wien Bibliothek.
TU Bibliothek Your knowledge hub WIEN

5.7 Summary and outlook

In this chapter, we demonstrate degenerate Raman cooling of the nanofiber-trapped atoms. Our cooling scheme relies on the strong gradients of fictitious magnetic fields, which naturally arise for atoms trapped using evanescent fields of nanofiber-guided light. The implementation of the DRC scheme in our system requires only one additional laser field, which can be either fiber-guided or in free space. Thus, our cooling scheme is directly applicable to a wide variety of optical microtraps, e.g., nanophotonic-based atom traps. We use fluorescence spectroscopy to measure the temperature of trapped atoms. We confirm all motional DOF can be cooled close to the ground state.

One interesting technical improvement in the near future is to probe the atom's temperature using Raman sideband spectroscopy [62]. This would allow us to characterize the performance of the DRC scheme with stimulated Raman transitions. We expect observation of even lower numbers of the mean motional state excitation since the photon recoil heating rate is significantly reduced in this method. In addition, Raman sideband spectroscopy can be used to probe transient atomic temperature. This would open the possibility to directly measure the heating rate in all three motional DOF simultaneously. Furthermore, it would be interesting to study the effectiveness of DRC using different trapping laser frequencies and powers, which would result in the change of trap frequency and coupling strength of spin-motion DOF.

By preparing atoms close to the motional ground state near a nanophotonic waveguide, we ensure homogeneous coupling between the guided light and the nanofiber-trapped atoms. This could significantly improve the performance of experiments which rely on the collective effect of the atomic ensemble, e.g., atomic Bragg mirrors [28, 29], quantum memories [26, 32], or squeezing protocols [63]. In a more general context, by cooling atoms close to the ground state, we provide a well-defined initial states for future studies including near-surface effects [40, 64–66], or quantum friction [67].

Die approbierte gedruckte Originalversion dieser Dissertation ist an der TU Wien Bibliothek verfügbar.
The approved original version of this doctoral thesis is available in print at TU Wien Bibliothek.
TU Bibliothek Your knowledge hub WIEN

Die approbierte gedruckte Originalversion dieser Dissertation ist an der TU Wien Bibliothek verfügbar.
The approved original version of this doctoral thesis is available in print at TU Wien Bibliothek.

Die approbierte gedruckte Originalversion dieser Dissertation ist an der TU Wien Bibliothek verfügbar.
The approved original version of this doctoral thesis is available in print at TU Wien Bibliothek.

CHAPTER 6

Ultra-strong spin-motion coupling of nanofiber-trapped atoms

Studying light-matter interaction is at the heart of quantum optics. A textbook example is the quantum Rabi model (QRM) describing the interaction of a single bosonic mode and a two-level system. Together, with its extension for an ensemble of atoms, namely the Dicke model (DM), they constitute as a cornerstone of quantum optics due to their universality. Both models have been used extensively for a wide variety of quantum systems, e.g., cavity and circuit QED systems.

In the past decade, there has been tremendous progress in realizing larger coupling strengths and new regimes of light-matter interaction. In particular, g can be made comparably large with respect to the bosonic mode frequency ω_0. In this regime, the RWA breaks down, yielding the ultra-strong coupling (USC) regime, i.e., for $\eta_c = g/\omega_0 \gtrsim 0.1$, where η_c is normalized coupling strength. In 2009, USC was first experimentally realized in an intersubband polaritons system with $\eta_c \approx 0.1$ [68, 69]. In 2010, USC was also realized in superconducting circuits, where $\eta_c \approx 0.1$ [70, 71]. When the coupling strength is increased further, i.e., $\eta_c \approx 1$, the deep-strong coupling (DSC) regime can be realized [72]. DSC was achieved more recently in circuit QED as well as by coupling a planar THz metamaterial with cyclotron resonances [73–75].

In the USC and DSC regimes, the very nature of light-matter interaction can be modified. In particular, the higher-order coupling, i.e., between states with different numbers of excitations, can no longer be neglected. In the USC and DSC regimes, there are new possibilities to study and engineer light-matter systems, which could lead to many applications, e.g., novel protocols for quantum communication and quantum information processing [76–79]. Furthermore, at these non-perturbative regimes, the existence of a quantum phase transition is expected in the thermodynamic limit, which adds to the richness of the DM [80–82].

While current experimental setups have reached the USC and DSC regimes, the large coupling strength makes state preparation and read-out challenging. For this reason, alternative routes were proposed to achieve large coupling in experimental platforms that, at the same time, offer a high level of control and tunability [83, 84]. Among these proposals, the QRM in the

USC and DSC regimes has been realized in both circuit QED and single-trapped ions experiments [85–87].

In this chapter, we realize a mechanical analog of the Dicke model using the spin-motion coupling of nanofiber-trapped atoms. As shown in chapter 2, strong gradients of the fictitious magnetic field arise naturally in nanofiber-based optical traps. The fictitious magnetic field gradients facilitate the coupling between atom's motional and spin degrees of freedom (DOF). With spin-motion coupling induced by a linear fictitious magnetic field gradient, the Hamiltonian of a nanofiber-trapped atom is formally equivalent to the QRM or the DM [88]. Instead of photons in a cavity QED system, the bosonic mode is represented by atoms' motional states. Hence, ω_0 is given by the trap frequency of $\approx$100 kHz, which is $\sim$9 orders of magnitude less than the energy of a photon in the optical domain.

To probe the energy spectrum of the trapped atoms' Hamiltonian, we employ fluorescence spectroscopy which was used previously to measure atoms' temperature during degenerate Raman cooling (see chapter 5). In these fluorescence spectra, we observe a vacuum Rabi splitting and also the transitions between the dressed states. In addition, we infer the coupling strength from the vacuum Rabi splitting, which is shown to be a significant fraction of the mode frequency and thereby in the USC regime. Furthermore, we show that the coupling strength can be readily tuned in situ using an additional laser light field. The discussion in this chapter closely follows the published manuscript [89].

6.1 Simulating quantum Rabi model and Dicke model with nanofiber-trapped atoms

The Rabi model was first introduced in 1935, describing the transition between Zeeman substates in the presence of a rapidly varying weak magnetic field [90]. Later, Jaynes and Cummings introduced the quantum Rabi model (QRM) describing a two-level atom interacting with a quantized bosonic mode:

$$H_{QRM}/\hbar = \omega_{eg}\hat{\sigma}_z + \omega_0\hat{a}^\dagger\hat{a} + g(\hat{a}^\dagger + \hat{a})\hat{\sigma}_x, \tag{6.1}$$

where $\hat{a}$ ($\hat{a}^\dagger$) is the creation (annihilation) operator for the single bosonic mode, $\hat{\sigma}_x$ and $\hat{\sigma}_z$ are the Pauli matrices of the two-level system, ω_{eg} is the energy gap of the two-level system, ω_0 is the single bosonic mode frequency, and g is the coupling strength between the two-level system and the bosonic mode.

By substituting $\hat{\sigma}_x$ with the raising operator $\hat{\sigma}_+$ and the lowering operator $\hat{\sigma}_-$, we can rewrite the coupling term in equation 6.1 as $g(\hat{\sigma}_+\hat{a}^\dagger + \hat{a}\sigma_-) + g(\hat{a}^\dagger\hat{\sigma}_- + \hat{a}\hat{\sigma}_+)$. The co-rotating terms $\hat{a}\hat{\sigma}_+$ and $\hat{a}^\dagger\hat{\sigma}_-$ conserve the total number of excitation, i.e., $\hat{a}\hat{\sigma}_+$ ($\hat{a}^\dagger\hat{\sigma}_-$) corresponds to the annihilation (creation) of one bosonic excitation and the creation (annihilation) of one spin excitation. In contrast, the counter-rotating terms $\hat{a}^\dagger\hat{\sigma}_+$ and $\hat{a}\hat{\sigma}_-$ do not conserve the total number of excitations.

The DM was first introduced to describe the phenomenon of superradiance, where N indistinguishable two-level systems interfere constructively in their emission process at an amplitude

Die approbierte gedruckte Originalversion dieser Dissertation ist an der TU Wien Bibliothek verfügbar.
The approved original version of this doctoral thesis is available in print at TU Wien Bibliothek.
TU Bibliothek Your knowledge hub WIEN

proportional to N [91]. The DM has the following Hamiltonian:

$$H_{DM}/\hbar = \omega_0 \hat{a}^\dagger \hat{a} + \sum_{j=1}^{N} \omega_{eg} \hat{\sigma}_z^j + g(\hat{a}^\dagger + \hat{a}) \sum_{j=1}^{N} \hat{\sigma}_x^j, \tag{6.2}$$

When $N = 1$, the DM is identical to the QRM model. The coupling strength g depends on the dipole moment of the atomic transitions. Most cold-atom systems, e.g., cavity QED systems, are in the so-called strong coupling regime, where g is larger than the rate of dissipation. In this regime, a coherent exchange of excitations between a bosonic mode and an atom can be observed in Rabi oscillation. However, g can be orders of magnitude smaller than ω_{eg} and ω_0 in the strong coupling regime. Hence, the rotating-wave approximation (RWA) is valid and the counter-rotating terms that are far off-resonant can be neglected. The resulting Hamiltonian after this approximation is known as the Jaynes-Cummings model:

$$H_{JC}/\hbar = \omega_0 \hat{a}^\dagger \hat{a} + \omega_{eg} \hat{\sigma}_z + g(\hat{\sigma}_- \hat{a}^\dagger + \hat{\sigma}_+ \hat{a}). \tag{6.3}$$

In chapter 3, we derived the Hamiltonian of the trapped atoms in the y motional DOF and with an additional offset magnetic field B_0 along the $+y$ direction:

$$\hat{H} = \hbar\omega_y \hat{a}_y^\dagger \hat{a}_y + \hbar\Delta \hat{F}_y + \frac{\hbar g_y^{'}}{\sqrt{2F}} \left(\hat{a}_y^\dagger + \hat{a}_y\right) \left(\hat{F}_+ + \hat{F}_-\right), \tag{6.4}$$

where $\hat{F}_+$ ($\hat{F}_-$) is the spin raising (lowering) operator, Δ is the Zeeman splitting between adjacent m_F substates and is proportional to the magnitude of an external offset magnetic field, B_0.

For equation 6.4, we substitute equation 3.6 in chapter 3 with $\Omega_y/2 = g_y^{'}/\sqrt{2F}$ so the coupling strength $g_y^{'}$ becomes independent of the F-quantum number. For $F = 1/2$, the Hamiltonian (6.4) becomes the QRM. When $F > 1/2$, the Hamiltonian corresponds to the DM with $N = 2F$ two-level systems. In this case, $\hat{F}_x$ in equation 6.4 becomes the angular momentum operator of a pseudo-spin-$N/2$:

$$\hat{F}_x = \frac{1}{2}(\hat{F}_+ + \hat{F}_-) = \sum_{j=1}^{N} \hat{\sigma}_x^j, \tag{6.5}$$

where the states with the same number of total spin excitations, spanning from $-N$ to N, can be mapped onto Zeeman substates $m_F = -N...N$. For example, the state $F = 4$ of the cesium atom allows one to simulate the DM with 8 two-level systems.

The physics of the QRM and the DM is governed by three parameters: The mode frequency, ω_y, the Zeeman splitting between adjacent m_F-states, $\Delta \propto B_0$, and the spin-motion coupling strength, $g_y^{'} \propto b_y$, where b_y is the gradient of the fictitious magnetic field along the y-direction. An *ab initio* calculation using our trapping configuration yields $g_y^{'} \approx 2\pi \times 17\,\text{kHz}$, $\omega_y \approx 2\pi \times 82\,\text{kHz}$, and $g_y^{'}/\omega_y \approx 0.2$ (see chapter 3).

Die approbierte gedruckte Originalversion dieser Dissertation ist an der TU Wien Bibliothek verfügbar.
The approved original version of this doctoral thesis is available in print at TU Wien Bibliothek.
TU Bibliothek Your knowledge hub WIEN

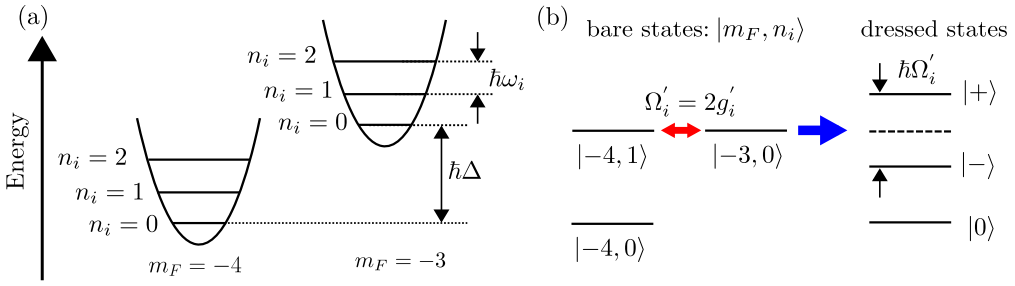

Figure 6.1: Schematic diagram for spin-motion coupling. (a) In the absence of spin-motion coupling, the eigenstates in the harmonic trapping potentials are $|m_F, n_i\rangle$ with eigenenergies $\hbar(m_F\Delta + n_i\omega_i)$, where $\hbar\Delta$ is the Zeeman splitting between two adjacent m_F substates and $\hbar\omega_i$ is the energy of one motional quantum. The spin-motion coupling is resonant for $\Delta = \omega_i$. (b) At the resonance of spin-motion coupling, the energy degeneracy between $|-4,1\rangle$ and $|-3,0\rangle$ is lifted. The energies of the new eigenstates $|+\rangle$ and $|-\rangle$ are split by $\hbar\Omega_i'$. We denote $|-4,0\rangle$ as the ground state $|0\rangle$.

6.2 Fluorescence spectroscopy and 2D spectrum

We measure the energy spectrum of nanofiber-trapped atoms using fluorescence spectroscopy. The experimental scheme is detailed in section 4.5. The trapped atoms are excited by a σ^- polarized light propagating along the $+y$ direction. This light is used to optically pump atoms to the low-lying energy states and facilitate degenerate Raman cooling, see Fig. 6.1 [60]. We set the excitation light to be red-detuned with respect to the cycling transition of the D_2 line of cesium. The final spectrum is obtained using heterodyne detection (see chapter 4).

In our experiment, the nanofiber-trapped cesium atoms are initially prepared in the $F = 4$ hyperfine ground state. In the absence of spin-motion coupling, the eigenstates of $\hat{H}_y$ are the bare state $|m_F, n_y\rangle$, where n_y corresponds to the motional state of the harmonic trapping potential in the y DOF. The energy diagram of the bare states is illustrated in Fig. 6.1(a). In the presence of spin-motion coupling, the motional and spin states become hybridized, thereby the new eigenstates are dressed states. We illustrate this effect in Fig. 6.1(b), where the spin-motion coupling is resonant ($\Delta = \omega_y$). Due to spin-motion coupling, the energy degeneracy of the two bare states $|-4,1\rangle$ and $|-3,0\rangle$ is lifted. The new eigenstates are now superpositions of the bare states, i.e., $|\pm\rangle = (|-4,1\rangle \mp |-3,0\rangle)/\sqrt{2}$. The two dressed states are separated in energy by $\hbar\Omega_y'$, where Ω_y' is the Rabi frequency. Here, we expected $\Omega_y' = 2g_y' = 2\pi \times 34\,\mathrm{kHz}$ based on an *ab initio* calculation (see chapter. 3).

We measure fluorescence spectra for different values of the Zeeman splitting, $\Delta \propto B_0$, see Fig. 6.2(a)-(c), where Δ corresponds to the energy of the two-level systems in the Dicke model. By tuning the offset magnetic field B_0, and thereby Δ, we can modify the spin-motion coupling condition to be either off-resonant or on-resonant. The ordinate axis in Fig. 6.2(a) corresponds to the Zeeman splitting expected at a given B_0. In the case of far off-resonance, i.e., for $|\Delta - \omega_i| \gg \Omega_i'$, we observe three pairs of motional sidebands. An example of such a spectrum is shown in Fig. 6.2(b) measured at a Zeeman splitting of Δ_1, indicated by the top

Die approbierte gedruckte Originalversion dieser Dissertation ist an der TU Wien Bibliothek verfügbar.
The approved original version of this doctoral thesis is available in print at TU Wien Bibliothek.
TU Bibliothek Your knowledge hub WIEN

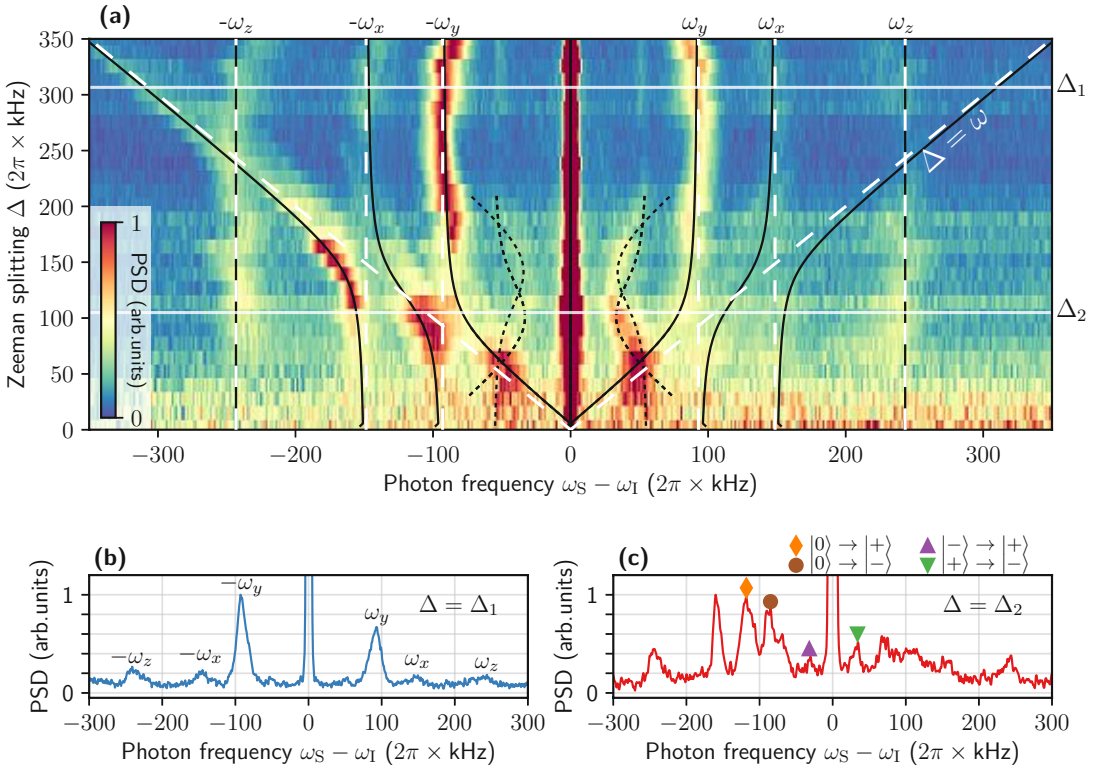

Figure 6.2: (a) Fluorescence spectra for different values of Δ. The two horizontal white lines indicate the Zeeman splitting Δ_1 and Δ_2 used for the spectra in panel (b) and (c), respectively. The avoided crossings occur when the resonance condition is fulfilled for the x DOF or the y DOF. The predicted transitions between the ground-to-bare states are derived from a fit of the data far from resonance and are indicated by the dashed white lines. In particular, the two diagonal dashed white lines indicate the transition between two adjacent Zeeman substates, i.e., $|F = 4, m_F = -4\rangle$ and $|F = 4, m_F = -3\rangle$. We use this transition to calibrate the offset magnetic field. The solid black lines indicate a multi-parameters fit of the ground-to-dressed state transitions. We infer the coupling strength from this fit. The inter-dressed-state transitions are indicated by the dashed black lines. (b) Fluorescence spectra when the Zeeman splitting is Δ_1. Here the coupling is far from resonance, and three pairs of motional sidebands are apparent. (c) Fluorescence spectra when the Zeeman splitting is Δ_2 and the coupling condition is fulfilled for the y DOF. The transition between the two dressed states $|-\rangle \rightarrow |+\rangle$ ($|+\rangle \rightarrow |-\rangle$) is indicated by the up-pointing (down-pointing) triangle, whereas the transition $|0\rangle \rightarrow |+\rangle$ ($|0\rangle \rightarrow |-\rangle$) is indicated by the diamond (circle).

Die approbierte gedruckte Originalversion dieser Dissertation ist an der TU Wien Bibliothek verfügbar.
The approved original version of this doctoral thesis is available in print at TU Wien Bibliothek.
TU Bibliothek Your knowledge hub WIEN

horizontal white light in Fig. 6.2(a). Here the eigenstates of the trapped atoms can be represented by the bare states due to the near-absence of spin-motion coupling. The motional sidebands correspond to the transitions which the motional states is changed by one motional quantum. Thus the sideband positions correspond to the trap frequencies. We find $\{\omega_x, \omega_y, \omega_z\} = 2\pi \times \{149(2), 93(2), 243(5)\}$ kHz. The strong asymmetry of the sidebands indicates that atoms are close to the motional ground state [92]. Furthermore, we observe transitions between two adjacent m_F-states at a given motional state, shown as the diagonal line in the upper left part of Fig. 6.2(a). The m_F changing transitions at $\omega_I - \omega_S < 0$ originates from a combination of π polarized incident photon and σ^- polarized scattered photon. The π component of incident light field could originate from experimental imperfections, i.e., the propagation direction of the incident light field is not parallel to the quantum axis along y.

We now look at a spectrum with near-resonant spin-motion coupling, i.e., when the Zeeman splitting $\Delta \approx \omega_y$, see Fig. 6.2(c). A double-peak structure occurs near the expected frequency of ω_y. This structure corresponds to the transition between the ground state and the lowerest pair of dressed states. As we scan Δ around the resonances, two avoided crossings are visible near ω_x and ω_y, see panel (a), indicating that strong spin-motion coupling is present for both the x and y DOF. The coupling in the x DOF could arise from a spurious vector light shift originating from the interference of the external excitation light with its reflection on the nanofiber or from the imperfect alignment of the polarization of the trapping light fields. In addition, we can also observe transitions between the two dressed state, indicated by the triangles in Fig. 6.2(c) near the carrier transition. Since atoms are close to the motional ground state, the transition between the lowest pair of dressed states is pronounced [92]. By fitting the spectrum, we find $\Omega_y^{'} = 2\pi \times 35(1)\,\mathrm{kHz}$ and $\Omega_x^{'} = 2\pi \times 36(1)\,\mathrm{kHz}$, which correspond to normalized coupling strengths of $g_y^{'}/\omega_y = 0.19(1)$ and $g_x^{'}/\omega_x = 0.12(1)$, respectively. Therefore, our system is in the USC regime for both the x and y DOF.

6.3 Tuning the coupling strength

An advantage of our setup is the ability to tune the coupling strength *in situ*. Since the coupling is induced by light, we can turn the coupling on and off instantaneously compared to the timescale of the atom's internal and external dynamics. For this purpose, we utilize an additional fiber-guided light field at the tune-out wavelength of $\sim$880 nm (see section 2.3). We denote this light field as the tune-out laser. At the tune-out wavelength, the scalar polarizability vanishes for the electronic ground state of cesium, i.e., $F = 3$ and $F = 4$ hyperfine states. Therefore, the laser field only induces a vector light shift. When this field propagates in the same direction and has the same polarization as the blue-detuned trapping light field, we expect a partial compensation of the fictitious magnetic field gradient and thereby of the spin-motion coupling strength [58]. We demonstrate this capability by measuring the Rabi splitting $\Omega_y^{'}$ as a function of the tune-out laser power P_{880}, see Fig. 6.3. As expected, $\Omega_y^{'}$ decreases with P_{880}. The linear slope of the fitted line is $\mathrm{d}\Omega_y^{'}/\mathrm{d}P_{880} = 2\pi \times -120(10)\,\mathrm{Hz/\mu W}$, see Fig. 6.3(b). Taking into account the vector polarizability and the mode function of the nanofiber-guided tune-out light, an *ab initio* calculation yields a slope of $2\pi \times -100\,\mathrm{Hz/\mu W}$, which is in reasonable agreement with the experimental value.

Die approbierte gedruckte Originalversion dieser Dissertation ist an der TU Wien Bibliothek verfügbar.
The approved original version of this doctoral thesis is available in print at TU Wien Bibliothek.
TU Bibliothek Your knowledge hub WIEN

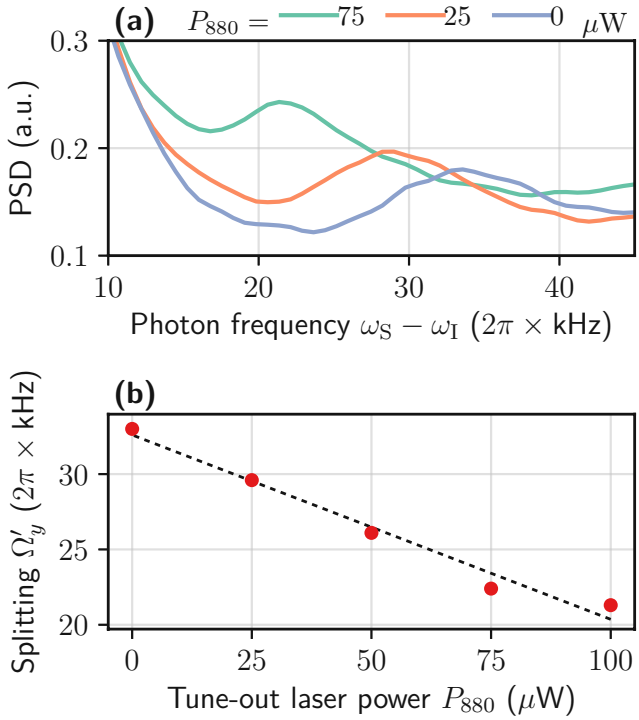

Figure 6.3: Tunability of the spin-motion coupling strength. We tune the spin-motion coupling strength using a nanofiber-guided tune-out laser field at a wavelength of $\sim$ 880 nm. The tune-out laser modifies the fictitious magnetic field gradient along y direction, which is proportional to the coupling strength. (a) Fluorescence spectra taken at resonant coupling of the y DOF ($\Delta = \omega_y'$) and different values of the tune-out laser power P_{880}. The peaks in panel (a) correspond to the $|+\rangle \rightarrow |-\rangle$ inter-dressed-state transitions. Each peak position corresponds to the Rabi splitting Ω_y'. The peak shifts toward the carrier frequency for increasing values of laser power P_{880}, indicating a reduction of the coupling strength. (b) Measured Ω_y' as a function of P_{880}. A linear fit, indicated by the black dashed line, yields $\mathrm{d}\Omega_y'/\mathrm{d}P_{880} = 2\pi \times -120(10)\,\mathrm{Hz/\mu W}$. For $P_{880} > 100\,\mu$W, the proximity of the carrier transition peak impedes a precise measurement of the peak position of the inter-dressed state transition.

Die approbierte gedruckte Originalversion dieser Dissertation ist an der TU Wien Bibliothek verfügbar.
The approved original version of this doctoral thesis is available in print at TU Wien Bibliothek.
TU Bibliothek Your knowledge hub WIEN

6.4 Exploration of the USC regime at higher coupling strengths

In this section, we explore the USC regime where the spin-motion coupling strength is increased. In contrast to the last section, we now reverse the propagation direction of the tune-out laser field so it counterpropagates with respect to the blue-detuned trapping light field. We expect the tune-out laser field increases the gradient of the fictitious magnetic field and thereby the coupling strength.

Fig. 6.4 shows the comparison of the atom's trapping lifetime with and without DRC at various $\Omega_y^{'}$. Here we convert the tune-out laser power to $\Omega_y^{'}$ using $\mathrm{d}\Omega_y^{'}/\mathrm{d}P_{880}$ obtained in section 6.3. The passive lifetime (without DRC) is roughly constant with respect to $\Omega_y^{'}$, indicating that the trapping potential and the heating rate are both similar at different tune-out laser power. In contrast, as we increase $\Omega_y^{'}$ during DRC, the trapping lifetime reduces by ∼2 orders of magnitude and becomes shorter than the passive lifetime. Since all other experimental parameters are constant, the drastic reduction of the trapping lifetime indicates an additional heating channel introduced by the combination of optical pumping and larger coupling strength.

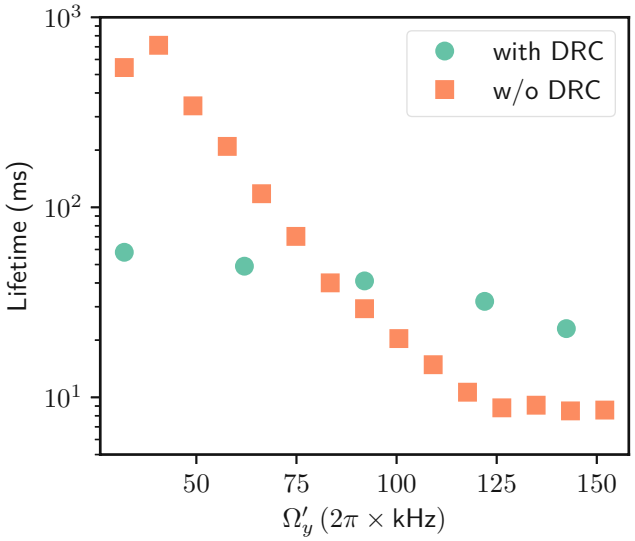

Figure 6.4: Comparison of the trapping lifetime in the presence (grey circle) and absence (orange square) of optical pumping, respectively.

In Fig. 6.5(a)-(f) show a collection of spectra at different $\Omega_y^{'}$. Note that the fluorescence spectra here are not obtained at a steady state as atoms are lost from the trap on the timescales shown in Fig. 6.4. An interesting feature in Fig. 6.5(a) is that the ratio between the area of two first-order y motional sidebands $S^y_{\Delta 1}$ and $S^y_{\Delta -1}$ decreases as the coupling strength increases, where $S^y_{\Delta \pm 1}$ is the area of the sideband corresponding to the transition $n_y \rightarrow n_y \pm 1$. At $\Omega_y^{'} = \sim 80\,\mathrm{kHz}$, an inversion of the sideband areas occurs, i.e., $S^y_{\Delta -1}$ is larger than $S^y_{\Delta 1}$. This inversion is usually a signature of the motional states' population inversion, which corresponds

Die approbierte gedruckte Originalversion dieser Dissertation ist an der TU Wien Bibliothek verfügbar.
The approved original version of this doctoral thesis is available in print at TU Wien Bibliothek.
TU Bibliothek Your knowledge hub WIEN

to a negative temperature in the case of thermal distribution. The population inversion should correspond to a high mean motional excitation number. To verify this, we compute the average motional excitation number in the y DOF inferred from the carrier-to-sidebands ratio:

$$\frac{S^y_{\Delta 1} + S^y_{\Delta -1}}{S_0} = (2\langle n_y \rangle + 1)\Delta k_y^2 {y_0}^2, \tag{6.6}$$

where y_0 is the RMS extent of the motional ground state in y DOF, S_0 is the area of the carrier transition, Δk_y is the change of the wavenumber along the y-axis during scattering. Consider the experimental geometry where the incident and scattered light fields propagate approximately in orthogonal directions, we use the wavenumber of the excitation light field in free space for Δk_y.

The average motional excitation $\langle n_y \rangle$ increases with Ω'_y, as shown in Fig. 6.5 (h), from $\sim$1 to $\sim$2 quanta. At $\langle n_y \rangle = 2$ quanta, the average motional energy is $\sim$8 µK, i.e., far below the trap depth expected in this trapping configuration at $\sim$180 µK. This suggests that the inversion of the motional sidebands does not originate from the population inversion of the motional state, but rather other mechanisms. By simulating the fluorescence spectrum using a master equation, we find the inversion of the motional sidebands can occur while observing π polarized emission. The master equation we used for this simulation is detailed in chapter 4. Since the reference light field in the heterodyne spectroscopy was aligned to a σ^- polarization, the π polarized emission should not show up in the observed spectra. Therefore, further investigation is needed to find out the origin of the motional-sideband inversion.

Die approbierte gedruckte Originalversion dieser Dissertation ist an der TU Wien Bibliothek verfügbar.
The approved original version of this doctoral thesis is available in print at TU Wien Bibliothek.
TU Bibliothek Your knowledge hub WIEN

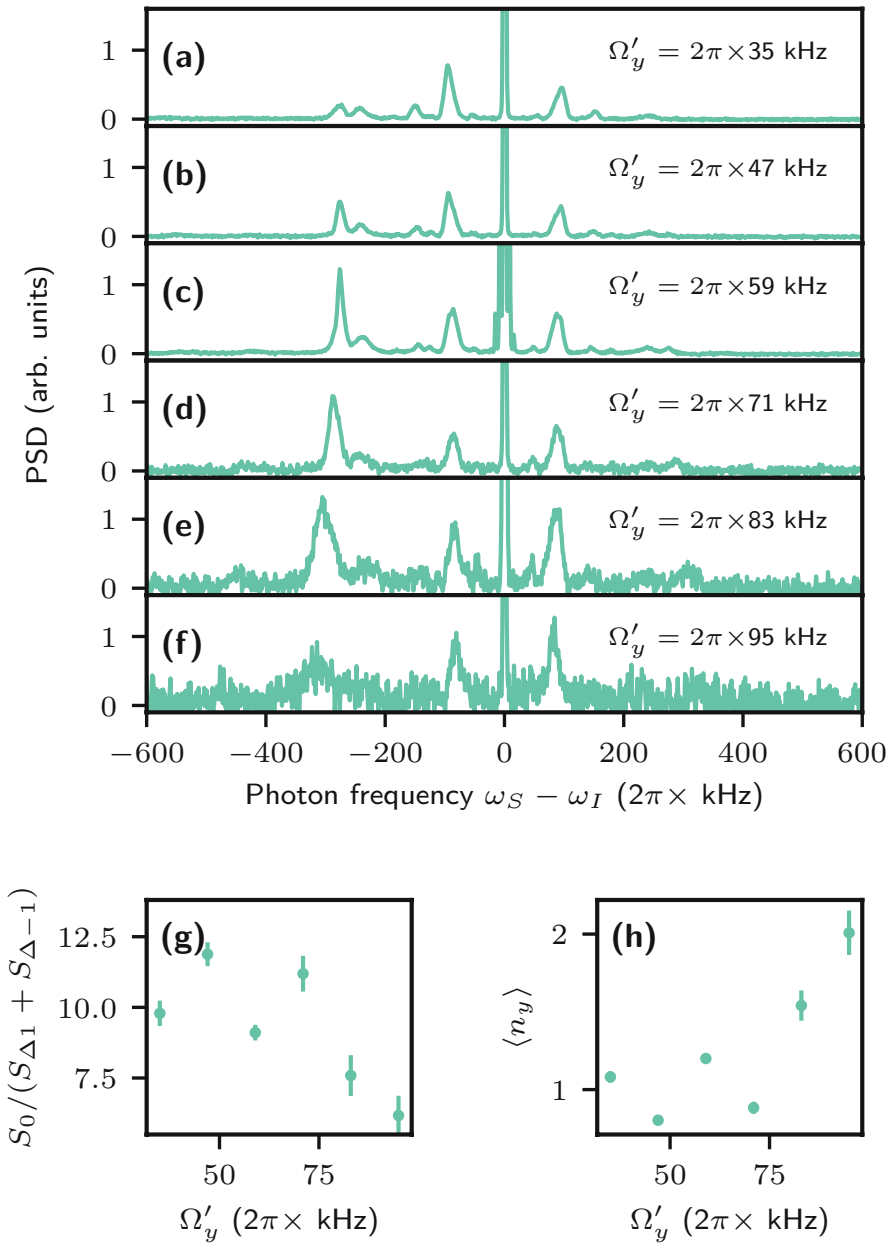

Figure 6.5: (a)-(f) Fluorescence spectra at different coupling strength $\Omega_y^{'}$. Each spectrum is normalized such that the peak of the carrier transition has the same amplitude. The coupling strength $\Omega_y^{'}$ is calculated based on the expected fictitious magnetic field gradient in the presence of the nanofiber-guided light field at the tune-out wavelength. (g) Ratio between the areas of two first-order y motional sidebands $S^y_{\Delta 1}$ and $S^y_{\Delta -1}$ as a function of $\Omega_y^{'}$. Both $S^y_{\Delta 1}$ and $S^y_{\Delta -1}$ are inferred from multiple Gaussian fits. (h) Mean motional excitation in the y DOF as a function of $\Omega_y^{'}$. We infer the mean excitation from the carrier-to-sidebands ratio. The error bars in panels (g) and (h) are propagated from the fit error.

Die approbierte gedruckte Originalversion dieser Dissertation ist an der TU Wien Bibliothek verfügbar.
The approved original version of this doctoral thesis is available in print at TU Wien Bibliothek.
TU Bibliothek Your knowledge hub WIEN

6.5 Summary and outlook

In summary, we show an implementation of the DM using the nanofiber-trapped atoms. Our implementation relies on the gradient of the fictitious magnetic field, which can occur in a wide classes of optical traps, e.g., optical lattices and free-space optical microtraps [93–95]. Our approach constitutes a new route to explore light-matter interaction in the USC regime, and potentially, even the DSC regime. By using a cold-atom setup, we also have access to the rich toolbox developed in the cold-atom community. In future implementations, other established techniques could be used to probe motional states and spin states [58, 96–99].

We demonstrate that the coupling strength can be readily tuned using a nanofiber-guided light at the tune-out wavelength. The ability to switch the spin-motion coupling off non-adiabatically is essential for projecting the system onto the uncoupled basis prior detection, allowing observation of quantum quench dynamics. In addition, the versatility of having tunable system parameters in our implementation enables the study of the dynamical Casimir effect [100] or of the role of dissipation in the USC and DSC [101]. Understanding these effects will be beneficial for realizing ultra-fast quantum gates or qubit protection protocols [77–79] relying on the USC. By tailoring real and fictitious magnetic field patterns, our implementation can be extended to realize generalizations of the QRM or the DM, e.g., the driven QRM, or the QRM with quadratic coupling [88].

Moreover, an important feature of the DM is a phase transition to a superradiant state once the coupling strength is at a critical value which is on the order of trap frequencies for our system [102]. Since the critical coupling strength can be reached using a tune-out laser, it would be interesting to investigate whether a phase transition can be observed in our setup.

Die approbierte gedruckte Originalversion dieser Dissertation ist an der TU Wien Bibliothek verfügbar.
The approved original version of this doctoral thesis is available in print at TU Wien Bibliothek.
TU Bibliothek Your knowledge hub WIEN

Die approbierte gedruckte Originalversion dieser Dissertation ist an der TU Wien Bibliothek verfügbar.
The approved original version of this doctoral thesis is available in print at TU Wien Bibliothek.

Die approbierte gedruckte Originalversion dieser Dissertation ist an der TU Wien Bibliothek verfügbar.
The approved original version of this doctoral thesis is available in print at TU Wien Bibliothek.

CHAPTER 7

Imaging of individual nanofiber-trapped atoms

One of the main assets of nanophotonic cold atom systems is to study atom-light interaction in unique geometries and at large interaction strength. Thus far, we have demonstrated the preparation of the internal and external quantum state of atoms trapped and optically interfaced with an optical nanofiber [58, 92, 103]. In light of these developments, the next steps to achieve further control of trapped atoms near a nanophotonic waveguide is to directly image and to selectively address individual atoms. For free-space atomic tweezer or atomic lattice experiments, there have been many remarkable results utilizing single-atom imaging and addressing [104–109]. In contrast to the free-space atomic traps, the nanophotonic-based atom traps are a few hundred nanometers away from a surface, which can act as a large scatterer of light. The main challenge for imaging has been suppressing the background scattered light field when illuminating the trapped cold atoms. Recently, optical tweezers have been employed to trap and position atoms close to an optical chip [110]. Atom imaging in such a tweezer array has been demonstrated. Furthermore, single-atom detection using a nanophotonic resonator has been demonstrated [16].

The discussion in this chapter closely follows our manuscript in PRL [111]. In this chapter, we present the experimental method for imaging nanofiber-trapped atoms. we show series of raw atom images under different experimental settings. In addition, we characterize the detection efficiency of a single trapped atom. To highlight the unique research opportunities enabled by single-atom imaging, we will show two applications. In the first application, we use atom imaging to determine the exact number of the trapped atoms and to measure the transmission of a nanofiber-guided probing light field as a function of the atom number. This gives us a direct measurement of the extinction per single atom interfaced with a waveguide. In the second application, we use atom imaging to study atom-scattered light fields that are coupled into the nanofiber-guided mode. In particular, we observe interference between the two atom-scattered light fields.

7.1 Experimental method

A schematic diagram of the experiment is shown in Fig. 7.1. We show in chapter 5 that degenerate Raman cooling (DRC) can be implemented with nanofiber-trapped atoms [92]. Here, we use DRC to continuously cool atoms close to their motional ground state while collecting atom-scattered light to image the atoms. We apply an offset magnetic field of $0.3\,\mathrm{G}$ in the y-direction. The excitation light is red-detuned relative to the D_2 cycling transition of Cesium and its wavelength is at $\sim 852\,\mathrm{nm}$. Unless otherwise mentioned in this chapter, the excitation light is an external light field in free-space. We also show the possibility of imaging with a nanofiber-guided excitation light in section 7.2. The $6S_{1/2}, F = 3$ is a dark state with respect to the excitation light. To pump atoms from $F = 3 \rightarrow F = 4$ of the $6S_{1/2}$ state, we use a nanofiber-guided light that is resonant on the D_1 transition, i.e., $6S_{1/2}, F = 3 \rightarrow 6P_{1/2}, F' = 4$. This light field has a quasi-linear polarization such that it is mainly σ^- polarized at the trapping sites. Since the D_1 transition is about $40\,\mathrm{nm}$ detuned from the D_2 line at $852\,\mathrm{nm}$, we can easily filter out the D_1 light before the camera or the SPCM with bandpass filters. We use a similar trapping configuration as described in the chapter 2 with two modifications. First, we change the wavelength of the blue-detuned trapping light to $762.6\,\mathrm{nm}$ (TOPTICA's DLX 110 diode laser). This wavelength is chosen to reduce the background noise originating from the Raman scattering induced by the trapping light field in the fiber material. In comparison to the $783\,\mathrm{nm}$ light used in previous chapters, we achieve a factor of 7 reduction of the Raman scattered light at $\sim 852\,\mathrm{nm}$ for the same power of the laser. Since the scalar light shift is about $30\,\%$ lower at $765\,\mathrm{nm}$ than $783\,\mathrm{nm}$, our second modification is to reduce the total power of the red-detuned standing light from $2.88\,\mathrm{mW}$ to $1.96\,\mathrm{mW}$. In this setting, the total trapping potential is similar to the one used in chapter 2, and the trapping potential minimum is about $270\,\mathrm{nm}$ from the nanofiber surface according to our *ab initio* calculation.

Atoms are initially loaded into the trapping potentials on both sides of the nanofiber. To avoid interference between the atom-scattered light on the two sides of the nanofiber, we use a nanofiber-guided light field to selectively heat out atoms trapped on one side of the nanofiber, see section 5.6 for details. To make sure the imaged atoms are illuminated evenly by the excitation light, we trap atoms in a smaller region in comparison to the diameter of the imaging beam. Before atom imaging, we perform DRC on the atoms for $300\,\mathrm{ms}$ using an excitation light with a Gaussian diameter of $200\,\mu\mathrm{m}$. Since the trapping lifetime during DRC is on the order of $1\,\mathrm{s}$, i.e., significantly longer in comparison to the passive trapping lifetime of $\sim 50\,\mathrm{ms}$, the diameter of the excitation light defines the region of the trapped atoms, see subsection 7.3.5. We perform atom imaging using an excitation light field with a diameter of $1300\,\mu\mathrm{m}$, more than 6 times larger in comparison with the previous excitation light. The uniformity of illumination is characterized experimentally in subsection 7.3.5. A smaller trapping region also helps us to minimize the effect of vignetting in the imaging process. This way, we ensure the width of the trapped atoms' position distribution is less than half of the width of the intensity profile of the excitation beam used for imaging.

We use a band-pass filter (Semrock $852\,\mathrm{nm}$ MaxLine) and a long-pass filter (Semrock $808\,\mathrm{nm}$ EdgeBasic) in front of the camera to further improve the ratio between the atom signal to the background. We collect the photons scattered by the atoms using an imaging objec-

Die approbierte gedruckte Originalversion dieser Dissertation ist an der TU Wien Bibliothek verfügbar.
The approved original version of this doctoral thesis is available in print at TU Wien Bibliothek.
TU Bibliothek Your knowledge hub WIEN

tive with a numerical aperture (NA) of 0.29 [112]. The objective is mounted $\sim 3.6\,\mathrm{cm}$ away from the nanofiber and inside the vacuum chamber. The solid angle corresponding to the NA is $\Omega/4\pi = (1-\sqrt{1-\mathrm{NA}^2})/2 \approx 2.1\%$. We image the light scattered by the atoms onto a camera (Andor iXon Ultra 897) using a $10\,\mathrm{cm}$ focusing lens outside the vacuum chamber. The magnification of our imaging setup is $\sim$3, and the point spread function of our imaging system has a measured $1/e$ radius of $\sim 10\,\mu\mathrm{m}$ in the objective plane. The CCD chip of the camera is set to -60°C, resulting in quantum efficiency of $\sim$45 % at $852\,\mathrm{nm}$. The light exiting the nanofiber, i.e., a nanofiber-guided probe light or the light scattered from the atom into guided modes, can be detected with an SPCM. Before the SPCM, we use a combination of short-pass, long-pass filter, band-pass filters, and a passively-stabilized ultra-narrow band Fabry-Pérot filter cavity (FPE001B, Quantaser) to filter out the Raman scattering originating from nanofiber-guided light. The combined transmission of the signal through the filtering system is $\sim$50 %, and the background SPCM count rate after filtering is $\sim$ 2 counts/ms.

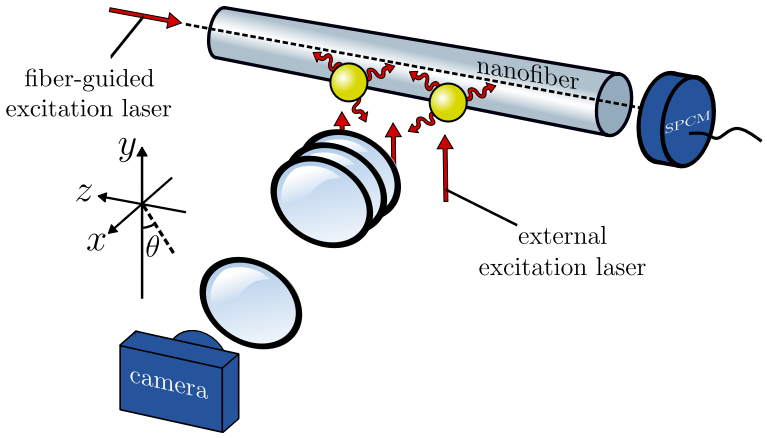

Figure 7.1: Experimental setup. Individual cesium atoms are trapped $\sim 270\,\mathrm{nm}$ away from the surface of an optical nanofiber. DRC is used to simultaneously counteract heating and generate fluorescence signals for imaging. The excitation light in DRC can be either an external light field propagating along the $+y$ direction or a nanofiber-guided light field. Individual atoms are imaged onto a camera using a combination of an in-vacuum objective lens and a focusing (convex) lens outside the vacuum chamber. A fraction of the fluorescent photons are coupled to the nanofiber-guided mode and are detected with an SPCM.

7.2 Raw atom images using an external or nanofiber-guided excitation light field

Fig. 7.2(a) shows a typical series of raw images from one experimental run. Here the excitation light is a σ^- polarized external light field propagating along the y-direction. We acquire consecutively 11 images with an exposure time of $150\,\mathrm{ms}$ per image. Between every two consecutive images, there are $45\,\mathrm{ms}$ of waiting time reserved for the camera to perform image readout and

Die approbierte gedruckte Originalversion dieser Dissertation ist an der TU Wien Bibliothek verfügbar.
The approved original version of this doctoral thesis is available in print at TU Wien Bibliothek.
TU Bibliothek Your knowledge hub WIEN

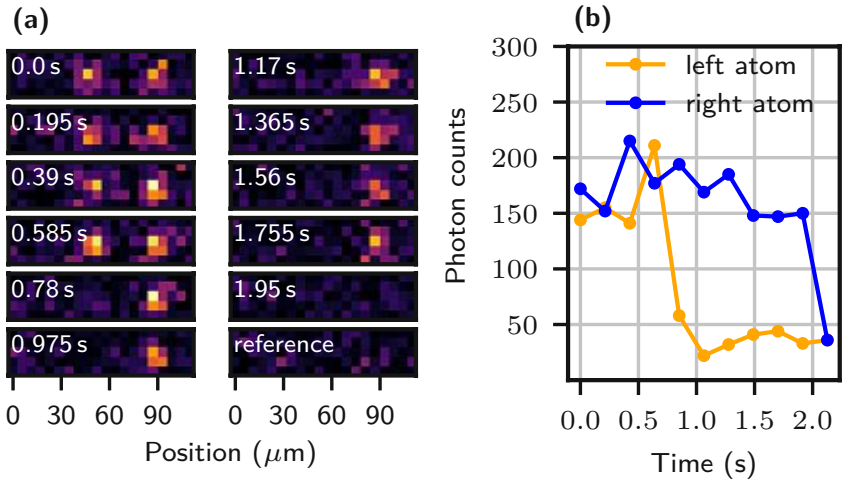

Figure 7.2: Raw images of nanofiber-trapped atoms. (a) A typical series of raw atom images. Each image has an integration time of 150 ms. (b) Time evolution of the atom photon counts. The photon counts are summed over regions of 3 × 3 pixels, centered on the atoms shown in (a). The photon counts drop to the background level when the left and right atom are lost from the trap after ∼0.8 s and ∼2 s, respectively.

to reinitialize for the next image. After imaging, we turn off the red-detuned trapping light field to lose any remaining trapped atoms. Moreover, in each experimental run, we take an additional reference image of 150 ms integration time when no trapped atoms are present but other experimental parameters, e.g., the intensity of the excitation light and trapping light, are same as during atom imaging. The first atom image in Fig. 7.2(a) contains two trapped atoms with similar photon counts. The left atom and the right atom are lost from the trap after ∼0.8 s and ∼2 s, respectively. In Fig. 7.2(b), we analyze the same series of images by summing photon counts over 3×3 pixel regions centered on the detected atom positions. The yellow (blue) symbols show the signal corresponding to the atom on the left (right). For each atom, ∼180 photon counts are observed per image. When an atom is lost from the trap, a significant drop of photon counts can be observed.

In addition, we demonstrate that faster imaging time can be achieved while the atom image remains clearly distinguishable from the background noise, see Fig. 7.3. Here the exposure time of each image is shortened to 100 ms and the waiting time between adjacent images is now 40 ms. All other settings, i.e., power and frequency of the excitation laser, remain unchanged from the previous experiment.

For some nanophotonic cold-atom systems, it might be challenging to use an external excitation light field for atom imaging without introducing excessive background light. Here we demonstrate atom imaging using only nanofiber-guided light, shown in Fig. 7.4. We use the same imaging scheme as in described in section 7.1 except the excitation light is now guided by the nanofiber. We align the polarization of the excitation light field such that it is mainly

Die approbierte gedruckte Originalversion dieser Dissertation ist an der TU Wien Bibliothek verfügbar.
The approved original version of this doctoral thesis is available in print at TU Wien Bibliothek.
TU Bibliothek Your knowledge hub WIEN

σ^- polarized at the trapping sites. The excitation light is -3 Γ detuned with respect to the D_2 cycling transition. The integration time for the image series in Fig. 7.4 is 400 ms. We expect the performance of the nanofiber-guided excitation light to be similar to the free-space excitation light, and a shorter exposure time such as 150 ms is sufficient for atom detection.

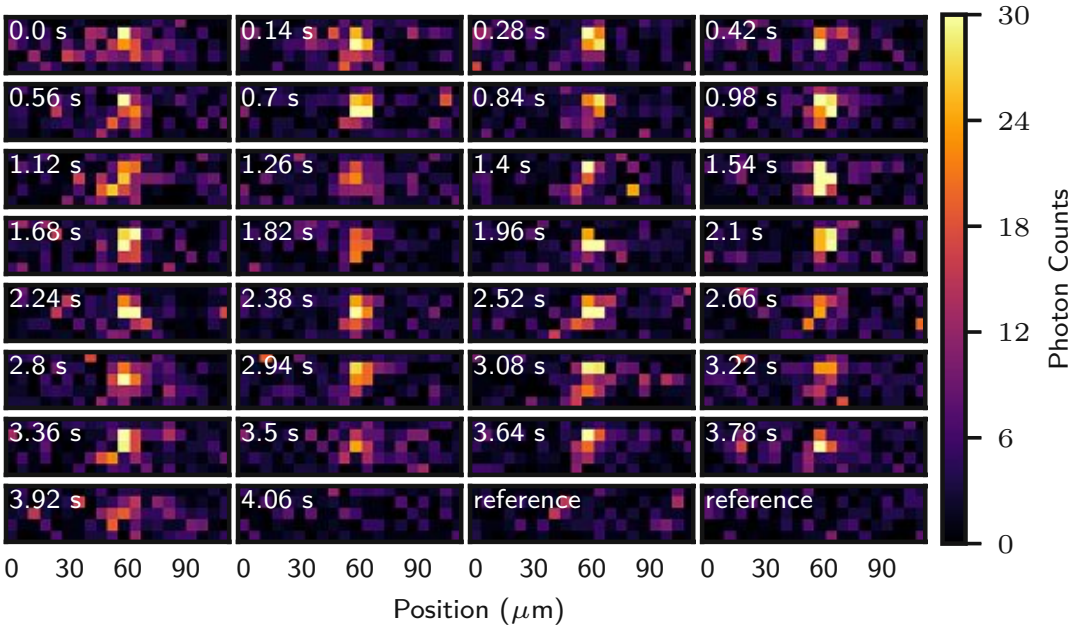

Figure 7.3: Fast atom imaging with an external light field. Each image has an integration time of 100 ms. Each experimental cycle consist of 32 consecutive images. The excitation beam is an external light field which is -3Γ detuned from the D_2 cycling transition and σ^- polarized.

Die approbierte gedruckte Originalversion dieser Dissertation ist an der TU Wien Bibliothek verfügbar.
The approved original version of this doctoral thesis is available in print at TU Wien Bibliothek.
TU Bibliothek Your knowledge hub WIEN

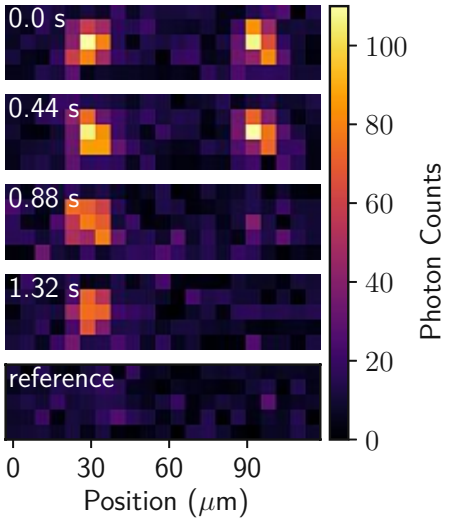

Figure 7.4: Atom imaging with a nanofiber-guided light. Here we show atom images with 400 ms of integration time each. An experimental cycle consists of 5 consecutive images.

7.3 Atom detection scheme

To detect the presence of atoms, we need to distinguish an atom signal from the background noise. The background noise consists of mostly camera dark counts, Raman scattering of the trapping light field, and other stray light fields, e.g., spuriously scattered excitation light. An example of the image section used for the detection sequence is shown in Fig. 7.5. The analysis outlined in this section relies on a dataset that was acquired over 6000 experimental runs. A typical experimental run is described in the previous section.

In the first step of our detection procedure, we smoothen the noise by convoluting the raw image with a discretized two-dimensional Gaussian. We set the two-dimensional Gaussian to have a full width at half maximum of 1.5 pixels or 8 µm in the object plane. It is set to zero outside an 11×11 pixel region. An example of the convoluted image is shown in Fig. 7.5(c). In the next step, we subtract each convoluted image with the averaged background image, which is generated by averaging over 6000 reference images. Note that average background image is also convoluted with the same two-dimensional Gaussian with a full width at half maximum of 1.5 pixels. We position the camera such that the highest photon counts from a trapped atom always falls into the same pixel row, regardless of the position of its trapping site along the nanofiber. Fig. 7.5(a) shows the average of images, i.e., of the first images obtained in all 6000 experimental runs. The central row of pixels shows the highest photon counts. In the final step, we analyze this row, see Fig. 7.5(d), and search for the position and value of pixels that exhibit local maxima of the photon counts. We find a trapped atom when a pixel value of these local maxima in the convoluted, background-corrected image exceeds a threshold of 18 counts. We save the position of this pixel in order to analyze the same spot in consecutive images. In Fig. 7.5(d), two atoms were detected and their locations are indicated by the two vertical dashed lines.

Die approbierte gedruckte Originalversion dieser Dissertation ist an der TU Wien Bibliothek verfügbar.
The approved original version of this doctoral thesis is available in print at TU Wien Bibliothek.
TU Bibliothek Your knowledge hub WIEN

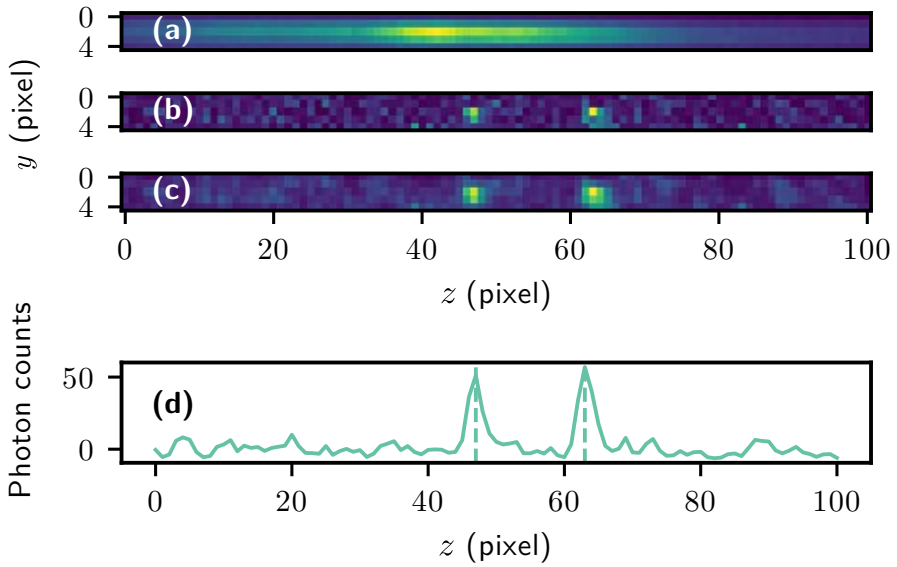

Figure 7.5: Atom detection scheme. (a) The mean of the first image of each 11-image series over 6000 experimental runs. (b) A typical example of a raw image. (c) The raw image in panel (b) is convoluted with a discrete two-dimensional Gaussian with FWHM of 1.5 pixels. (d) A horizontal cut of the background subtracted convoluted image in panel (c). The detected atom positions are indicated by the two vertical dashed lines.

To study how well we can herald the atoms in such experiments, we have quantitatively characterized the performance of our detection procedure, shown in Fig. 7.6. For this analysis, we use a region of interest of $\sim 300\,\mu\mathrm{m}$ along the nanofiber, see subsection 7.3.5. This corresponds to the segment of the nanofiber where most trapped atoms are prepared.

When our procedure detects one and only one atom in the region of interest, we take the non-convoluted, non-background corrected version of next image in the series and generate a histogram of the total photon counts in the 3×3 pixel region that is centered on the pixel at which the atom was detected. We repeat this for all image series of the data set. The resulting photon count histogram is shown in Fig. 7.6(a), which shows two distinct peaks. We expect that the left and right peak corresponds to the background photon counts in the absence of atoms and the presence of one atom, respectively. We fit this histogram with the sum of two Gaussians, see the black dashed line. The left peak is centered at 38.8(6) counts (standard deviation σ= 12.5(6), whereas the right peak is centered at 146.9(8) counts (σ= 32.6(8) counts).

To check the left peak corresponds to the background photon counts in the absence of atoms, we analyze the reference images for all 6000 experimental runs. We generate a photon count histogram of disjoint 3×3 pixel regions in these images, see Fig. 7.6(b). The histogram exhibits only one single peak. We perform a Gaussian fit to the histogram in Fig. 7.6(b), shown as the black dashed line, yielding a center value of 35.2(2) counts and a standard deviation of σ=10.5(2) counts. Therefore the presence of the left peak in Fig. 7.6(a) implies that there are some instances

Die approbierte gedruckte Originalversion dieser Dissertation ist an der TU Wien Bibliothek verfügbar.
The approved original version of this doctoral thesis is available in print at TU Wien Bibliothek.
TU Bibliothek Your knowledge hub WIEN

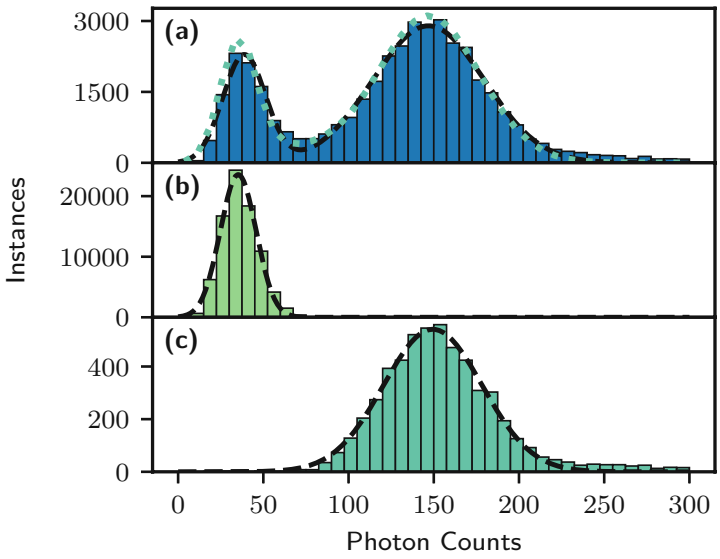

Figure 7.6: Histogram of photon counts of single nanofiber-trapped atoms obtained with the camera. The photon counts sum over 3×3 pixel squares that are centered on the detected atom positions. The threshold of the peak detection algorithm is at 18 pixel counts. In one run, we take 11 consecutive images with an integration time of 150 ms per image. (a) Histogram of photon counts conditioned on a detection event in the previous image, i.e., when an atom is detected in images number $1, 3, 5, 7, 9$. We build this histogram using the photon counts at the detected atom positions in the subsequent image frame. (b) Histogram of photon counts with no atoms in the trap. The narrow peak in the histogram corresponds to the background photon count distribution. (c) Histogram of photon counts when false detections and atom loss are excluded. Here the dataset is conditioned on the peak detection in the previous and subsequent images, i.e., images number (1,3), (3,5), (5,7), (7,9), (9,11), when building the histogram on images number $2, 4, 5, 6, 8$, respectively. The black dashed lines in the three panels are Gaussian fits, and the dotted line in panel (a) is a simulated photon count distribution, see text for details.

when no atom is present in the image following the one in which a detection event has occurred. There are two possible mechanisms that can lead to such a false detection event. First, the detection algorithm may erroneously detect atoms in an image where no atom is present. By running the detection algorithm on all 6000 reference images, we find that this happens with $\sim$ 7 % probability in the region of interest. Second, an atom that is correctly detected in an image may be lost before the next image is recorded due to the finite trapping lifetime.

We can rule out the occurrence of both mechanisms by analyzing also the image directly following the one that was used to generate the histogram in Fig. 7.6(a). When an atom is detected in this additional image, we obtain the photon count histogram in Fig. 7.6(c). This histogram exhibits one single peak which coincides with the right peak of the histogram in Fig. 7.6(a), which confirms that this peak originates from the in-situ fluorescence of a single

Die approbierte gedruckte Originalversion dieser Dissertation ist an der TU Wien Bibliothek verfügbar.
The approved original version of this doctoral thesis is available in print at TU Wien Bibliothek.
TU Bibliothek Your knowledge hub WIEN

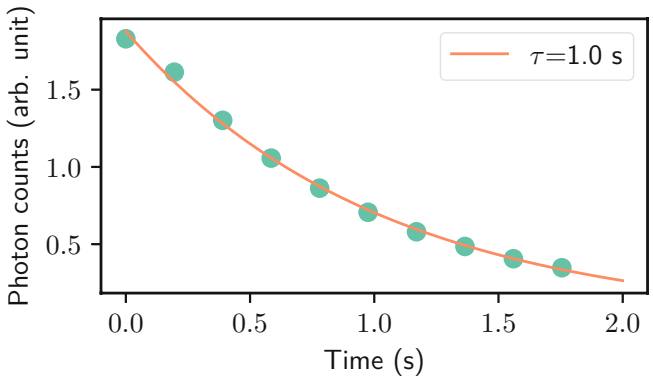

Figure 7.7: Measurement of the trapping lifetime of atoms during imaging. Each data point here corresponds to the mean photon counts per pixel in a given image number averaged over 6000 experimental runs. Due to the averaging over many realizations, we expect that the interference between different atom emissions can be neglected, and the atom signal is proportional to the atom number. The red line is an exponential fit.

nanofiber-trapped atom. We fit the histogram in panel (c) with a Gaussian (black dashed line), yielding a center value of 149.4(5) counts (σ= 29.0(5) counts). Note that the observed photon counts in panel (c) differ significantly from the threshold value of 18 pixel counts. The threshold condition refers to the photon counts of a single pixel while the histogram in panel (c) shows the photon counts of 3 $\times$ 3 pixel regions in the non-convoluted, non-background corrected images. Furthermore, the widths of the right peak in panel (a) and panel (c) are wider than the shot noise limited width. We attribute this, at least partially, to the position dependence of the single-atom signal, which originates from vignetting and inhomogeneous illumination with the external excitation laser beam, see subsection 7.3.5.

To confirm that the histogram in Fig. 7.6(a) is indeed influenced by atom loss and false detection, we establish a model which incorporates the photon count distributions from panels (b) and (c), the independently measured trapping lifetime during DRC of $\tau_{\mathrm{DRC}} \sim 1\,\mathrm{s}$ (see Fig. 7.7), and the probability for false detections to predict the data shown in panel (a). The model prediction is in a very good agreement with the experimental data, see the green dotted line in panel (a). From the model, we infer that the probability of not detecting a trapped atom due to its loss during the 150-ms image integration time is $\sim 6\,\%$. In addition, we infer that the probability of detecting a trapped atom which is then lost by the end of the image integration time is $\sim 8\,\%$. The details of this model are described in the next subsection.

7.3.1 Modeling photon count histogram and false atom detection probability in the presence of atom loss

In this subsection, we study in detail how the finite trapping lifetime of atoms can affect atom detection and alter the photon count histogram. To this end, we first simulate the photon count

Die approbierte gedruckte Originalversion dieser Dissertation ist an der TU Wien Bibliothek verfügbar.
The approved original version of this doctoral thesis is available in print at TU Wien Bibliothek.

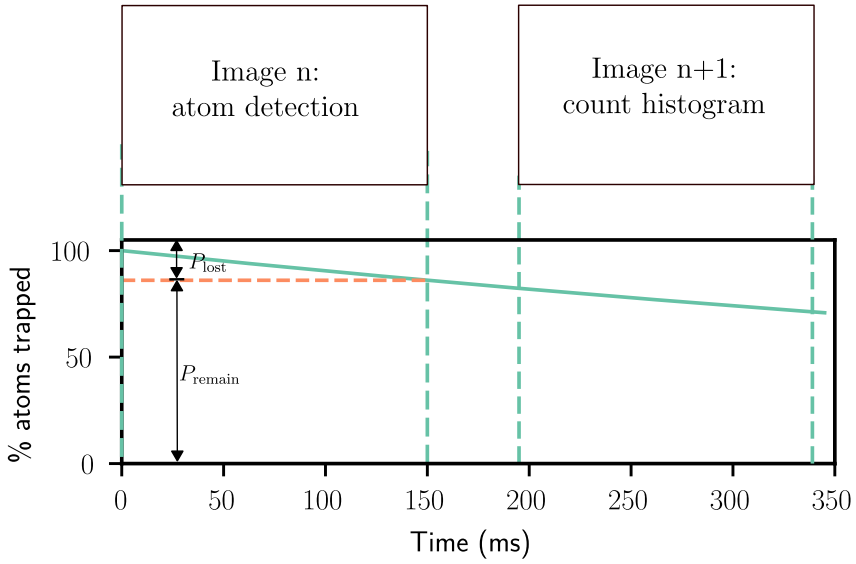

Figure 7.8: Time sequence of building the photon count histogram conditioned on atom detection in the previous image. The bottom panel shows an exponential decay representing the percentage of atoms that remain trapped since the beginning of imaging session. The two consecutive images are used for atom detection and for generating the photon count histogram, respectively. The integration time of each image is 150 ms, and there are 45 ms of waiting time between two adjacent imaging acquisitions.

distribution conditioned on the detection of a single atom in the previous image. In Fig. 7.8, we show the time sequence for building such a photon count histogram. We see in the bottom panel that the percentage of atoms that are lost after the first imaging session n, P_{lost}, is $\sim 14\,\%$

The procedure to compute the photon count histogram in presence of atom loss can be summarized in three steps (a detailed, quantitative discussion follows):

1. We compute the photon count histogram of the single-atom signal without atom loss using the histograms shown in Fig.7.6 (b) and (c). In this step, we remove the contributions of Poissonian and background noise.

2. We compute the histogram of the single-atom signal with a finite trapping lifetime.

3. We add Poissonian and background noise to the final histogram to compare with the experimental data.

The rate of atom loss is given by the measured trapping lifetime of 1 s, see Fig. 7.7. The probability for an atom to remain trapped at time t is given by the exponential function:

$$P_{atom} = e^{-t/1\,\text{s}}. \tag{7.1}$$

The photon count histogram when an atom is trapped during the entire image integration time is shown in Fig. 7.6(c). The histogram can be well fitted with a Gaussian function, shown as the

Die approbierte gedruckte Originalversion dieser Dissertation ist an der TU Wien Bibliothek verfügbar.
The approved original version of this doctoral thesis is available in print at TU Wien Bibliothek.

black-dashed line in Fig. 7.6(c). Thus we can approximate this histogram with a Gaussian profile, which is denoted as $H_{\text{atom+bng}}(n_{\text{ph}})$. Since $H_{\text{atom+bng}}(n_{\text{ph}})$ is based on the non-background corrected images, we need to remove the contribution of the background signal to find the count distribution of the atom signal. The photon count histogram of the background signal is shown in Fig. 7.6(b), and we use a Gaussian fit $H_{\text{bng}}(n_{\text{ph}})$ as an approximation.

Since both $H_{\text{atom+bng}}(n_{\text{ph}})$ and $H_{\text{bng}}(n_{\text{ph}})$ have Gaussian shapes, the histogram for the trapped atom without the background signal, $H_{\text{atom}}(n_{\text{ph}})$, also follows a Gaussian distribution. For notation, we denote $\tilde{n}$ and σ as the center and the standard deviation of the Gaussian, respectively, and we use the subscript to indicate the corresponding Gaussian-shaped histogram, e.g., $\tilde{n}_{\text{atom+bng}}$ is the center of the histogram $H_{\text{atom+bng}}(n_{\text{ph}})$. The center of $H_{\text{atom}}(n_{\text{ph}})$ is given by $\tilde{n}_{\text{atom}} = \tilde{n}_{\text{atom+bng}} - \tilde{n}_{\text{bng}}$, and the standard deviation of $H_{\text{atom}}(n_{\text{ph}})$ is given by $\sigma_{\text{atom}} = \sqrt{(\sigma^2_{\text{atom+bng}} - \sigma^2_{\text{bng}}) - \tilde{n}_{\text{atom}}}$. Note that we subtract $\tilde{n}_{\text{atom}}$ from the standard deviation to remove the contribution of the Poissonian noise. The standard deviation σ_{atom} originates from technical noise, i.e., inhomogeneous illumination and intensity drift of the excitation light.

For an atom that remains trapped at the end of imaging session n, see Fig. 7.8, there are three different cases:

- **Atom is lost during the 45-ms waiting time and before the imaging session n+1:** Since atom is already lost before the imaging session n+1, there are no atom signal in image $n+1$. The probability of this event is: $P_{\text{lossbf}} = 1 - P_{\text{atom}}(45\,\text{ms}) = 1 - \exp(-45\,\text{ms}/1\,\text{s}) = 0.04$.

- **Atom is lost during the imaging session n+1:** The chance for the atom to be lost from the trap at time $t_i = i\Delta t$ is given by $P(t_i) = P'_{\text{atom}}(t_i)\Delta t$. The trapped atom scatters light for $t_i/150\,\text{ms}$ of the imaging time. Note that we use discrete time step here for the computation.

- **Atom stays trapped during the entire imaging session of n+1:** The probability of this case is: $P_{\text{noloss}} = P_{\text{atom}}(45\,\text{ms}+150\,\text{ms}) = \exp(-(195\,\text{ms})/1\,\text{s}) = 0.82$. The atoms scatter light for 100 % of the imaging time.

We summarize the three cases into two vectors:

$$\begin{cases} P = [P_{\text{lossbf}}, P(t_1), P(t_2)...P_{\text{noloss}}] \\ R_t = [0, t_1/150\,\text{ms}, t_2/150\,\text{ms}, ..., 1] \end{cases},$$

where R_t is the ratio between the duration of atom being trapped and the image integration time.

We can calculate the photon count histogram with atom loss:

$$H_{\text{wloss}}(n) = \sum_{\substack{j \\ n=n_{\text{ini}}R_t(j)}} \sum_{n_i} (H_{\text{atom}}(n_{\text{ini}})P(j)), \tag{7.2}$$

where index j is used for both vector P and R_t.

Die approbierte gedruckte Originalversion dieser Dissertation ist an der TU Wien Bibliothek verfügbar.
The approved original version of this doctoral thesis is available in print at TU Wien Bibliothek.
TU Bibliothek Your knowledge hub WIEN

In the next step, we include the background noise by discretely convolving the histogram from equation 7.2 with the background histogram H_{bng}:

$$H_{\text{wloss+bng}} = H_{\text{wloss}} * H_{\text{bng}}. \tag{7.3}$$

Finally, we add back the contribution of the Poissonian noise:

$$H^{p}_{\text{wloss+bng}}(i) = \sum_{n} P_{\text{Pois}}(i, \lambda = n) H_{\text{wloss+bng}}(n), \tag{7.4}$$

where P_{Pois} is the Poisson distribution.

Now we have a photon count histogram which takes into account the atom loss. To compare with the photon count histogram shown in Fig. 7.6(a), i.e., the photon count histogram conditioned on the one-atom detection in the previous image, we need to account for two erroneous detection mechanisms which lead to additional instances of the background signal in the histogram.

First, due to statistical fluctuation, the background noise can be erroneously detected as atoms. At the detection threshold of a pixel value of 18 counts, a single false atom is detected in $P_F = 7$ % of the reference images which contain no trapped atoms, see subsection 7.3.2. Since the histograms in Fig. 7.6 are conditioned on the detection of one atom, this source of error contributes to the histograms when there are no trapped atoms but one false detection has occurred. Therefore, the percentage of this contribution in our histogram is given by $P_F N_0^r / N_1^d$, where N_1^d denotes the number of images in which we detect one atom, and N_0^r denotes the number of images which contain zero trapped atoms. The probability of the false atom detection in the entire reference image $P_{F,\text{ref}}$ is $\sim$14 %, whereas the 7 % quoted earlier this paragraph is for the region of interest used in our analysis in section 7.3, which is about half of the size of the entire image. We estimate N_0^r by dividing N_0^d by $(1 - P_{F,\text{ref}})$, where N_0^d is the number of images in which we detect zero atoms. We find the percentage of the false detections out of all one-atom detection events to be $\sim$9 %.

Second, an atom can be detected in an image but is lost during imaging due to the finite trapping lifetime. In order to infer this probability, we analyze the images underlying Fig. 7.6(c). As discussed in section 7.3, for these images, the presence of an atom in the trap during the entire integration time is ensured by the detection of an atom the previous and subsequent images with a fixed threshold of 18. As for the atom detection described in section 7.3, we smoothen these images through convolution, subtract the background, and determine the pixel value at the position of the detected atom. We plot the histogram of these pixel values in Fig. 7.9(a). For every pixel position used for Fig. 7.9(a), we find the pixel value at the same position in the corresponding reference image in the same experimental run, which contains no trapped atoms. The histogram of these pixel values corresponds to the background pixel counts and is shown in Fig. 7.9(b). Note that the counts in the pixel count histogram correspond to the maxima of the pixel values detected in the background subtracted and convoluted images, which differ from the photon counts in Fig. 7.6 that sum over 3×3 regions centered on the detected maxima. We use the same procedure described earlier this subsection (see 7.3.1) except here we no longer take Poissonian noise into account. The photon counts of the background-subtracted images can have negative photon counts and cannot be treated with Poissonian statistics. For simplicity,

Die approbierte gedruckte Originalversion dieser Dissertation ist an der TU Wien Bibliothek verfügbar.
The approved original version of this doctoral thesis is available in print at TU Wien Bibliothek.
TU Bibliothek Your knowledge hub WIEN

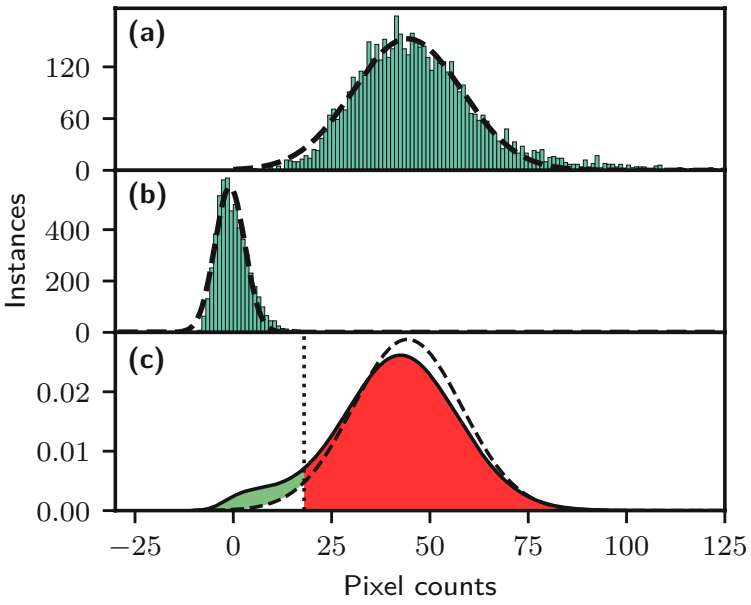

Figure 7.9: Pixel count histogram in presence of atom loss. (a) Measured pixel count histogram of a single detected atom which is present during the entire image integration time. (b) Measured pixel count histogram of the background signal. (c) Comparison between the theoretical pixel count distribution with atom loss (dashed line) and without atom loss (solid line). The vertical dotted line in panel (c) indicates the chosen threshold value of 18 pixel counts. The green shaded area represents the instances where atoms are lost and not detected, and the red shaded area represents the instances where atoms are detected.

we use the Gaussian fit in Fig. 7.9(a) as the pixel count distribution of atoms that stay trapped over the entire image acquisition time, shown as the dashed black lines in panel (a) and (c). The simulated pixel count distribution with atom loss is shown as the solid black line in the panel (c). Both distributions are normalized to have an integral of 1. The difference between the two distributions below the threshold value of 18 represents the fraction of atoms which are not detected due to loss from the traps, which amounts to 6 % out of total distribution. Since we know there is in total 14 % atom loss after the exposure time of one image, the joint probability of atoms that are lost from the trap and of atom detection $P_{\text{det}\cap\text{lost}}$ is 8 %. The instances of detected atoms correspond to the area above the threshold value of 18. We use this area as the detection probability P_{det}. We find the percentage of the detected atoms that are already lost during detection, $P_{\text{det}\cap\text{lost}}/P_{\text{det}} = 9\ \%$.

To compare with the histogram from our experiment, we sum over all contributions to the simulated photon count histogram, see Fig. 7.10. The light red area in Fig. 7.10 corresponds to the fraction of atoms that remain trapped after the previous imaging session, whereas the dark red area corresponds to the fraction of atoms that are lost but still detected. Together, the light and dark red areas represent all detection events originating from trapped atoms, which corresponds

Die approbierte gedruckte Originalversion dieser Dissertation ist an der TU Wien Bibliothek verfügbar.
The approved original version of this doctoral thesis is available in print at TU Wien Bibliothek.
TU Bibliothek Your knowledge hub WIEN

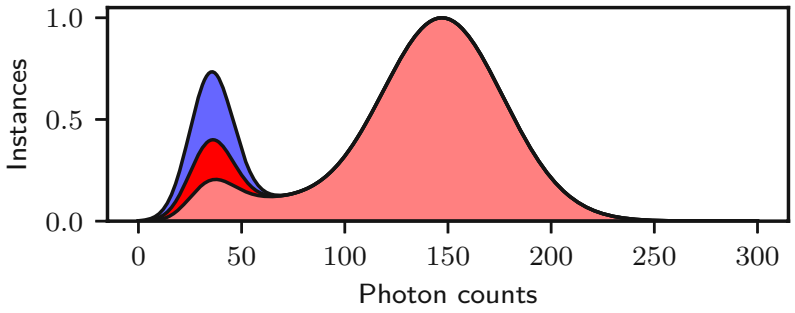

Figure 7.10: Simulated photon count histogram. The light red region corresponds to the instances where the detected atoms remain trapped at the end of integration time of image n. The dark red region corresponds to the instances where atoms that were lost during the integration time of image n but are still detected. The blue region corresponds to the false detection events where no trapped atoms are present during imaging.

to the red region in Fig. 7.9(c). Furthermore, the blue region represents the contribution from falsely detected atoms. We normalize this region to have 9 % of the total colored area. For the instances where atoms are not trapped, i.e., represented by the blue and dark red regions in Fig. 7.10, they follow the background count distribution $H_{\mathrm{bg}}(n_{\mathrm{ph}})$ (see also Fig. 7.10(b)). Finally, after summing over all contributions, we normalize the total photon count distribution to have the same number of instances as our experimental data, resulting in the simulated photon count distribution shown as the green dotted line in Fig. 7.6(a).

7.3.2 Atom detection probability as a function of detection threshold

We examine the effect of the threshold on the atom detection. The basis for the analysis in this subsection is the same data set that underlies Fig. 7.6. Due to statistical fluctuation, background noise can result in pixel counts that exceed the threshold value, and thereby get falsely detected as atoms. We can increase the detection threshold to lower the probability of false atom detections. On the other hand, choosing a higher threshold will also decrease the atom detection efficiency since the statistical fluctuation of the atom signal can result in pixel counts that are lower than the threshold. More quantitatively, one figure of merit is the probability of detecting a trapped atom for a given threshold. The atom loss in our system is dictated by the rate of the background gas collision and subject to day to day changes of the vacuum chamber pressure. Therefore, to characterize the performance of the atom imaging, it is more systematic to look at the detection probability of atoms that remain trapped for the duration of the entire image integration time.

In order to infer this probability, we use the same data that is used to generate Fig. 7.9(a). As discussed in the previous subsection, we use images where the presence of an atom in the trap during the entire integration time is ensured. We take the convoluted, background-subtracted version of these images, and determine the pixel value at the position of the detected atom. We

Die approbierte gedruckte Originalversion dieser Dissertation ist an der TU Wien Bibliothek verfügbar.
The approved original version of this doctoral thesis is available in print at TU Wien Bibliothek.
TU Bibliothek Your knowledge hub WIEN

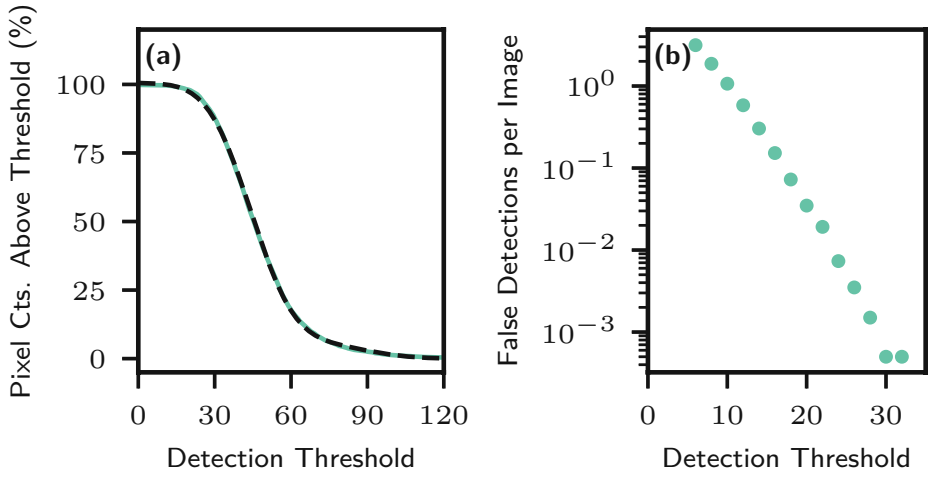

Figure 7.11: Atom detection at different threshold values. (a) Percentage of pixel counts above a given threshold value (green solid line). The black dashed line is a fit using the sum of two cumulative Gaussian distribution functions. (b) Mean number of false detections per image as a function of threshold. Here, we use 6000 reference images which are taken in absence of trapped atoms.

compute the percentage of pixel counts above a threshold value as a function of this threshold, see the green line in Fig. 7.11. When all analyzed images contained exactly one atom, this percentage corresponds to the efficiency of detecting a trapped atom. However, there are cases when two nearby trapped atoms may mistakenly be detected as a single trapped atom. This will lead to images with an anomalously high pixel value. This effect appears in the small asymmetry of the histogram of photon counts shown in Fig. 7.6(c), i.e., the distribution is above the fitted Gaussian towards the larger photon counts.

To infer the probability of detecting a single trapped atom in spite of this systematic error, we fit the data in Fig. 7.11(a) with the sum of two cumulative Gaussian distribution functions, indicated by the black dashed line. The two cumulative Gaussian distributions correspond to a single atom and two unresolved trapped atoms, respectively. We assume in our fit that the latter has on average twice the pixel counts of the former. The fit is in good agreement with the data. From the fit, we find the probability of detecting a single atom is ∼97.5 % at a threshold value of 18. We choose this threshold value for the atom detection procedure shown in section 7.3.

Another useful figure of merit is the number of false atom detections per image at a chosen threshold, see Fig. 7.11(b). Here, we apply the atom detection procedure to 6000 reference images, which were acquired in the absence of trapped atoms. We compute the mean number of false detections per image by averaging the occurrence of false atom detections over all reference images. We infer from this data that the probability of at least one false detection to occur in a given image is ∼7 % at the chosen threshold of 18.

Die approbierte gedruckte Originalversion dieser Dissertation ist an der TU Wien Bibliothek verfügbar.
The approved original version of this doctoral thesis is available in print at TU Wien Bibliothek.
TU Bibliothek Your knowledge hub WIEN

7.3.3 Determine atom positions with sub-pixel resolution

To determine atom positions better than the pixel resolution, we fit atom images with a Gaussian function and use the fitted center for atom localization. The estimated one-dimensional position error for an atom with the Gaussian shaped point spread function is given by [113]:

$$(\Delta z)^2 = \frac{\omega_{\mathrm{RMS}}^2 + \Delta_p^2/12}{N} + \frac{4\sqrt{\pi}\omega_{\mathrm{RMS}}^3\,\sigma_b^2\,n_\perp}{\Delta_p\,N^2}, \tag{7.5}$$

where N is the average number of recorded photons per atom, $n_\perp$ is the number pixels that the fluorescence signal is integrated over in the direction transverse to the lattice, ω_{RMS} is the RMS width of a Gaussian PSF, Δ_p is the size of a camera pixel in the object plane, and σ_b is the background noise per pixel.

The procedure to determine atom positions is shown in Fig. 7.12. Using the peak finding procedure described in section 7.3, we detect atoms after image smoothing and background subtraction. To better localize the atom, we only consider instances where an atom is detected in three consecutive images. We first sum over the three consecutive raw atom images without additional image processing. We then take 5×3 pixel regions centered on the detected atom positions, and integrate them along the direction transverse to the lattice. We fit the resulting one-dimensional array with a Gaussian function and use the fitted center as the atom position, see Fig. 7.12(c). For typical experimental parameters described in section 7.3, we have $\omega_{\mathrm{RMS}} = 1.2$ pixels, Δ_p =5.76 µm, $N = 340$ counts, $n_\perp = 3$ pixels, and $\Delta z \approx$500 nm.

In addition, by fitting the atom images, we can better quantify the variation of PSF of atoms along the nanofiber. In Fig. 7.12(d) we see the fitted Gaussian width of atom images as a function of atom positions. We see the fitted width varies by ~ 50 % in the region of interest, i.e., the region between 20 and 70 pixels.

Die approbierte gedruckte Originalversion dieser Dissertation ist an der TU Wien Bibliothek verfügbar.
The approved original version of this doctoral thesis is available in print at TU Wien Bibliothek.
TU Bibliothek Your knowledge hub WIEN

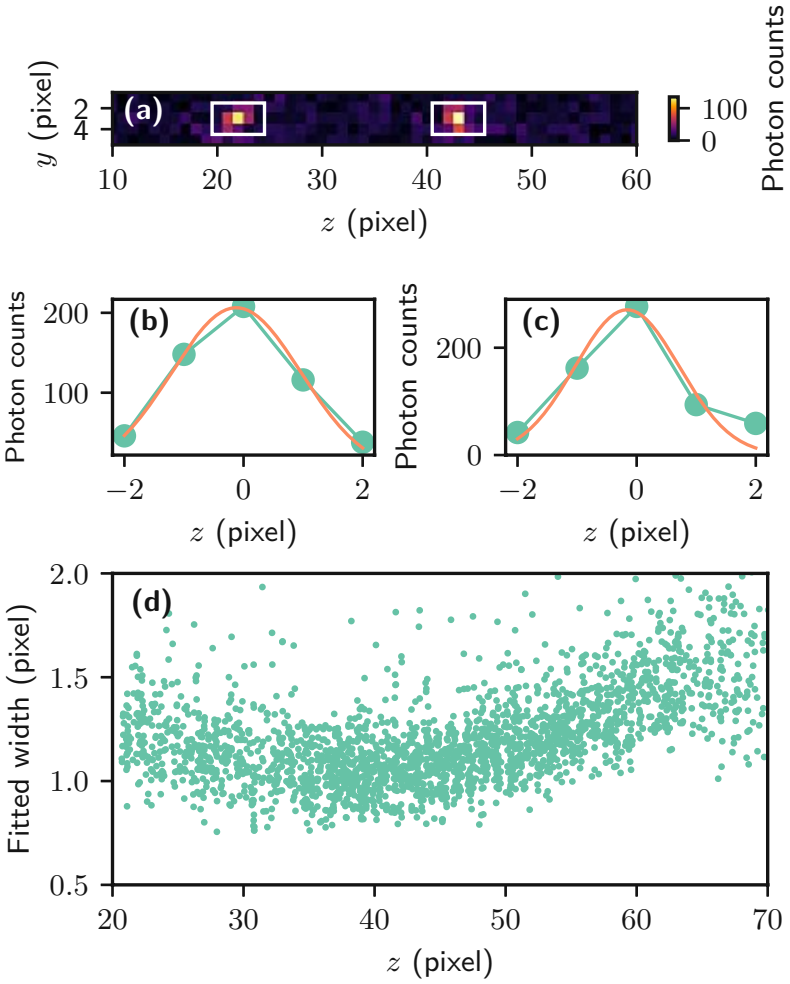

Figure 7.12: Measurement of atom positions using imaging. (a) Example of an image showing two nanofiber-trapped atoms. The image shown here is integrated over three consecutive imaging sessions of 150 ms integration time. The white boxes enclose 5 × 3 pixel regions centered on the detected atom positions. (b) Photon counts of atoms in one dimension. We integrate the 5 × 3 pixel regions shown in (a) along the y-axis, and fit the resulting one-dimension array with Gaussian function. We use the center of fitted Gaussian as the position of the atom. (c) Width of the fitted Gaussian along different nanofiber positions. The variation of fitted widths at different nanofiber positions is due to astigmatism of the imaging setup.

7.3.4 Atom detection error due to nearby atoms

The PSFs of our imaging system can be inferred from atom images. The $1/e$ Gaussian width of the PSF is ∼10 µm . Since the lattice spacing in our system is ∼500 nm, the two atoms that are only a few lattice sites apart cannot be spatially resolved by our detection scheme. In Fig. 7.13

Die approbierte gedruckte Originalversion dieser Dissertation ist an der TU Wien Bibliothek verfügbar.
The approved original version of this doctoral thesis is available in print at TU Wien Bibliothek.
TU Bibliothek Your knowledge hub WIEN

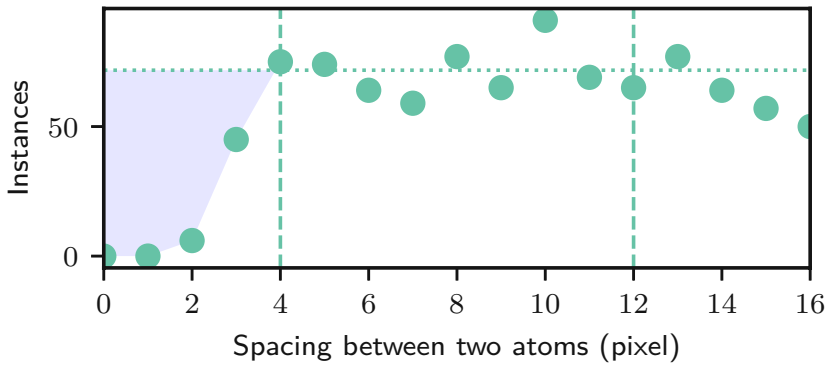

Figure 7.13: Instances of two-atom spacing. Based on the one-atom position distribution, we expect the instances of the two-atom spacing to be near constant when the two-atoms events are correctly detected. When two atoms are closely spaced, they can be detected as one. The occurrence of this event is highlighted in the light blue region. The horizontal dotted line indicates the average number of instances of atom-atom distance between 4 and 12 pixels.

we plot the occurrence of detected atom-atom distances conditioned on a two-atom detection. Based on the one atom position distribution, which has a FWHM of $250\,\mu\mathrm{m}$ or ~ 46 pixels, we expect the distribution of the two-atom distance to be nearly flat at the distance below 10 pixels. However, we see the occurrence of the two-atom distance gradually drops to zero at distances below 4 pixels. We compute the average instances between 4 and 12 pixel distance and use it as the expected instances for a flat distribution of atom-atom distances, shown as the horizontal dotted line. We interpret the area of the difference between the flat distribution and the detected two-atom distance distribution as the number of instances where two atoms are falsely detected as one atom, shown as the blue region in Fig. 7.13. We can thus estimate the percentage of instances where two atoms are falsely detected as one out of the total two-atom instances to be $\sim 14\,\%$.

To mitigate events where two atoms are detected as one, we can use an additional processing procedure. The emissions from the two atoms interfere constructively or destructively depending on their distance. When the two atoms are at least 3 lattice sites away from each other, the size of the interference fringe at the objective lens is less than the lens diameter of $2.54\,\mathrm{cm}$. In this case, the intensity of the atom signal at the lens is about twice of one-atom signal. We can then identify two-atom events based on the photon counts, see 7.3.2.

7.3.5 Position dependence of single-atom signal

We study the level of light scattered by a single nanofiber-trapped atom as a function of its position along the nanofiber. We record in parallel the photon counts of atom images on the camera and the SPCM counts of the scattered light that are coupled into the nanofiber-guided mode. To check the position dependence of single-atom signal, we plot both the camera counts and the SPCM counts in panel (a) and (b) of Fig. 7.14 as a function of the atom position, respectively.

Die approbierte gedruckte Originalversion dieser Dissertation ist an der TU Wien Bibliothek verfügbar.
The approved original version of this doctoral thesis is available in print at TU Wien Bibliothek.
TU Bibliothek Your knowledge hub WIEN

For this analysis, we use the camera images to determine the atom position. The uniformity of SPCM counts and photon counts both depend on the spatial variation of the excitation light intensity. However, the SPCM counts depend also on the local coupling efficiency of the scattered photon into the nanofiber-guided mode, whereas the photon counts in atom images depend additionally on the collection efficiency of the imaging system at different trap positions.

To avoid the complication of spatial interference between multiple atom-scattered light fields, the underlying data in Fig. 7.14 are conditioned on the detection of a single trapped atom in the previous and subsequent images. For the region of interest between $100\,\mu\mathrm{m}$ and $400\,\mu\mathrm{m}$ where most atoms are trapped, the SPCM counts vary within 5 %. The photon counts seen by the camera are less uniform in the same region, showing a variation of ~ 20 % due to imperfections of the imaging system. The horizontal black-dotted lines in Fig. 7.14(a) and (b) indicate the background photon counts measured without any trapped atoms.

Fig. 7.14(c) shows the histogram of the locations of the detected atoms. The two vertical-dash lines in Fig. 7.14(c) enclose the region of interest used for Fig. 7.6. The photon counts in Fig. 7.14(b) is summed over every 3×3 pixel region centered at the detected atom position. We do data binning over $50\,\mu\mathrm{m}$ intervals for Fig. 7.14(a)-(c).

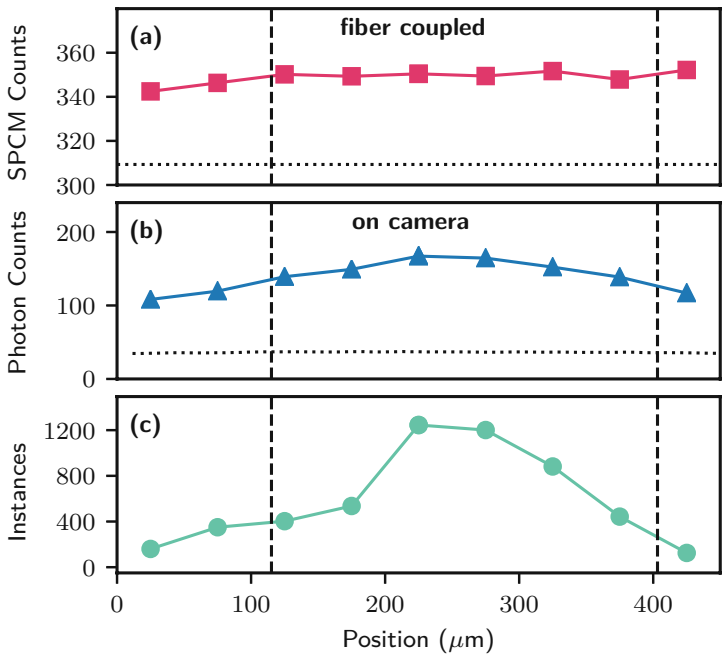

Figure 7.14: Position dependence of single-atom signals. (a) SPCM counts of nanofiber-coupled light. (b) Photon counts of 3×3 pixel regions detected with the camera (c) Spatial distribution of detected atom location. In (a) and (b), the counts are averaged over atom events occurring in $50\,\mu\mathrm{m}$ wide intervals. In (c), the instances are summed up in the same $50\,\mu\mathrm{m}$ intervals.

Die approbierte gedruckte Originalversion dieser Dissertation ist an der TU Wien Bibliothek verfügbar.
The approved original version of this doctoral thesis is available in print at TU Wien Bibliothek.
TU Bibliothek Your knowledge hub WIEN

7.4 Resonant transmission through nanofiber-coupled atoms

Taking advantage of our imaging technique, we measure the extinction of a resonant nanofiber-guided probing light as a function of the atom number determined by atom imaging. The extinction per atom is an important figure of merit for atom-nanophotonic systems since it characterizes how well the atom is coupled to the guided light. We detect the transmitted light with an SPCM and use spectral filters to lower counts detected from the background, see section 7.1. We choose a resonant probing light at the D_2 cycling transition to increase the extinction per atom. The probing light field is quasi-linearly polarized along the x-axis, and it is almost perfectly σ^- polarized at the positions of the trapped atoms on one side of the nanofiber [114]. This probing light also functions as the excitation light in DRC which counteracts against recoil heating. In practice, DRC works more effectively when this excitation light is far detuned, i.e., higher trapping lifetime. This could originate from the large differential Zeeman shift induced by light at the near resonance condition. To increase the trapping lifetime of atoms during resonant transmission measurement, we use an interleaved scheme where we illuminate atoms alternatingly between a resonant and a -3 Γ detuned light field for $0.2\,\mathrm{ms}$ and $0.5\,\mathrm{ms}$, respectively. This way, atoms reinitialize to a cooler temperature by the detuned light field in each cycle, and they are less likely to be heated out after the resonant transmission. We repeat this sequence for 450 cycles in one experimental run. Furthermore, we acquire atom images before and after all transmission measurements. We condition our dataset on detecting a constant number of atoms in the images before and after to ensure no occurrence of atom loss during the transmission measurement.

In Fig. 7.15, histograms of the detected SPCM counts of the resonant transmission are shown. The histograms in Fig. 7.15(a)-(d) are conditioned on the detection of zero, one, two, or three atoms, respectively. The histograms show the mean distribution shifts to a lower value by more than 100 counts with every additional atom. We calculate the mean SPCM counts, $\bar{N}(i)$, for $i = 0 \ldots 3$ atoms. We find that the extinction increases with each additional atom. The mean extinction per atom is $\{\bar{\eta}(1), \bar{\eta}(2), \bar{\eta}(3)\}$={0.039(1), 0.039(1), 0.043(3)} , where $\bar{\eta}(i) = 1 - \bar{N}(i)/\bar{N}(i-1)$. These values are constant within the error, which is in agreement with Beer-Lambert law. The mean extinction per atom is consistent with the prediction using an atom–fiber surface distance of $\sim$300 nm, which is close to the expected position of the trap minimum of $\sim$270 nm that is calculated using the trap configuration in our experiment. The slightly larger value of the atom–fiber surface distance might originate from the fact that some atoms are not in the motional ground state during the transmission measurement. As the trapping potential along the radial direction is asymmetric and falls off more slowly further away from the trap minimum, we expect the mean atom-surface distance is larger at higher motional states.

To correct for the drifts of the experimental setting, e.g., the probe laser power or the frequency of the filter cavity, we record SPCM counts in the absence of the trapped atoms at the end of each experimental run. We calculate the moving average of the photon counts by summing over two consecutive experimental runs, shown in Fig. 7.16(a). The standard deviation of the moving average is about 6 % of its mean value. We rescale the moving average by dividing its mean value. Finally, we correct the SPCM counts by dividing it by the rescaled moving average. Fig. 7.16(b) and (c) show the histograms with and without correction of the drifts, respectively.

Die approbierte gedruckte Originalversion dieser Dissertation ist an der TU Wien Bibliothek verfügbar.
The approved original version of this doctoral thesis is available in print at TU Wien Bibliothek.
TU Bibliothek Your knowledge hub WIEN

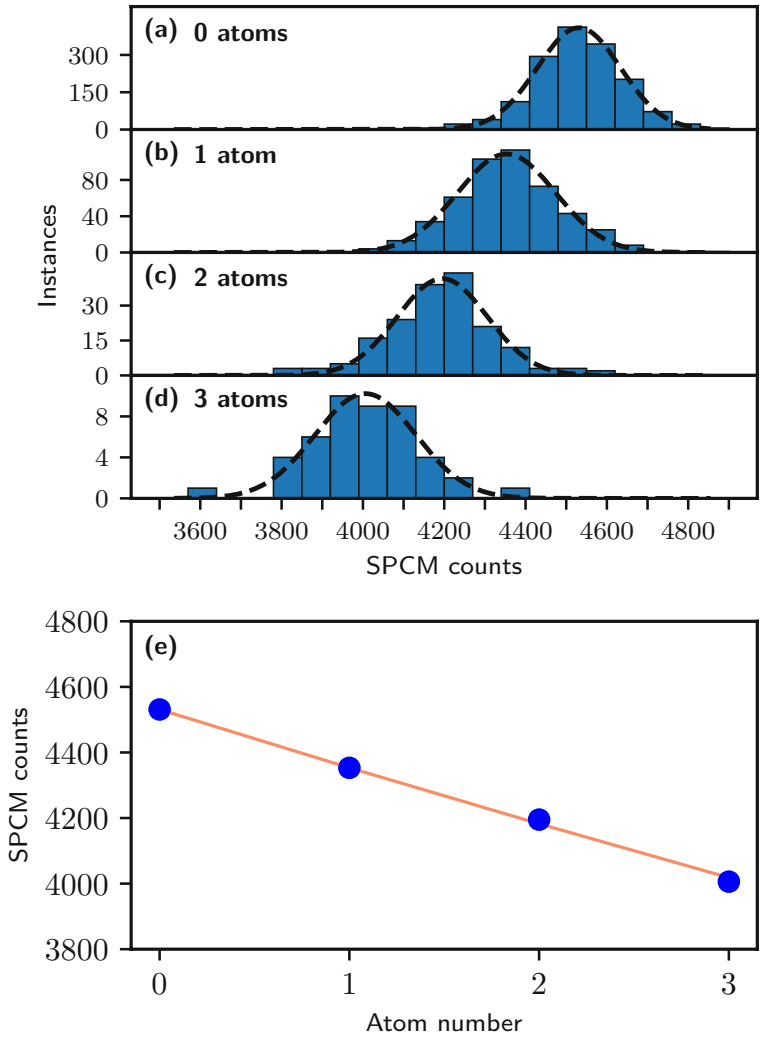

Figure 7.15: Histograms of the SPCM counts of the resonant light transmitted through nanofiber-trapped atoms. (a)-(d) Histograms of the transmitted photon number conditioned on having zero, one, two, or three atoms detected, respectively. (e) SPCM counts as a function of atom number. The transmission is fitted using Beer-Lambert's law, shown as the red-solid line.

Die approbierte gedruckte Originalversion dieser Dissertation ist an der TU Wien Bibliothek verfügbar.
The approved original version of this doctoral thesis is available in print at TU Wien Bibliothek.

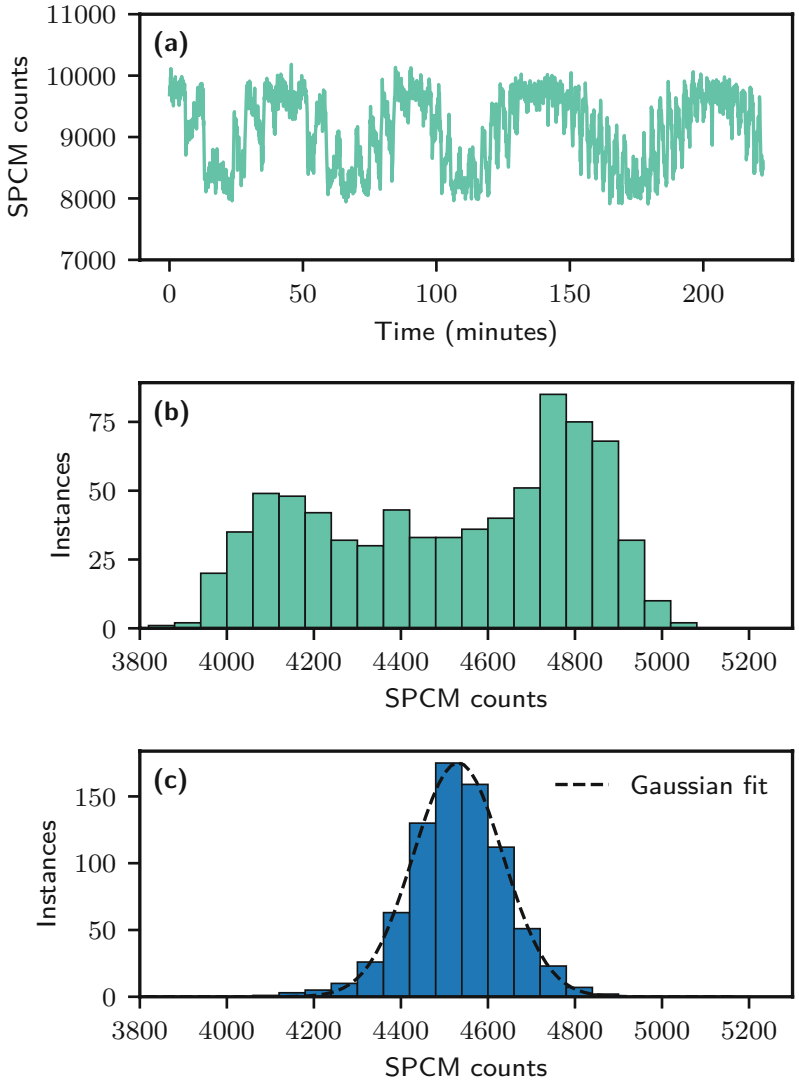

Figure 7.16: (a) SPCM counts of the nanofiber transmitted light in the absence of the trapped atoms. This is measured at the end of each experimental sequence and used for referencing drifts of the setup. The plotted photon counts sum over two consecutive reference measurements. (b) Histogram of the transmitted photon counts conditioned on zero atoms detected. The underlying data in the histogram is measured separately but in the same sequence as the referencing measurement. (c) Same as figure (b) but the photon counts are corrected for drifts using the reference measurement.

Die approbierte gedruckte Originalversion dieser Dissertation ist an der TU Wien Bibliothek verfügbar.
The approved original version of this doctoral thesis is available in print at TU Wien Bibliothek.
TU Bibliothek Your knowledge hub WIEN

7.5 Scattering of light by atoms into the nanofiber-guided mode

We study the scattering of light by single as well as pairs of trapped atoms into the nanofiber-guided mode. For this purpose, we image atoms while recording the signal of the nanofiber-coupled scattered light with an SPCM. Fig. 7.17(a)-(c) show the SPCM count histogram conditioned on the detection of zero, one, and two atoms in images taken with the camera, respectively. We fit the two histograms in Fig. 7.17(a) and (b) with a Gaussian function. In the case of zero-atoms detection, as shown in panel (a), the Gaussian center $\bar{N}_{\mathrm{bg}}$ and width $\sigma_{N_{\mathrm{bg}}}$ are at 309.63(9) and 18.89(9) counts, respectively. The background contribution is close to a Poissonian distribution or shot-noise limited, i.e., $\sigma_{N_{\mathrm{bg}}} \approx \sqrt{\bar{N}_{\mathrm{bg}}}$. Panel (b) corresponds to the case of one-atom detection. The fitted Gaussian center in panel (b) $\bar{N}_1$ is at 345.8(7) counts, a clear shift from the zero-atom case. The increase in the SPCM counts originates from the light scattered by one atom into the nanofiber-guided modes. Furthermore, the Gaussian RMS width for the one-atom case σ_{N_1} is 30.9(7) counts, about 70 % wider than what is expected from Poissonian distribution. We attribute the super-Poissonian distribution of the one-atom signals to the experimental drift and other imperfections, e.g., shot to shot variation of atom-nanofiber coupling strengths due to drift of trapping laser power and the inhomogeneity of the excitation laser intensity along the nanofiber.

We now look at the SPCM count histogram conditioned on a pair of trapped atoms. The saturation parameter in our experiment is ~ 0.0023, therefore we expect mainly coherent scattering of the excitation light field by the atoms. The light fields scattered by individual atoms will interfere constructively or destructively, depending on their relative phase. In the case of perfect interference between two fields of equal amplitude, the SPCM counts are bounded by maximum constructive and destructive interference between the light scattered by trapped atoms. The lower bound of counts thus corresponds to the background signal, whereas the upper bound corresponds to the sum of the background signal and four times the counts of the one-atom signal. We take the mean counts in Fig. 7.17(a) and (b), and plot the corresponding lower and upper bounds of counts as the two vertical black-dotted lines in Fig. 7.17 (a)-(c). Assuming the excitation light field is a plane wave, the relative phase between the two-atom scattered light fields varies linearly with respect to the inter-atomic distance. The excitation light in our experiment is at a $\sim 16^\circ$ incident angle with respect to the y-axis of our coordinate system. This results in even sampling of relative phases of the scattered light fields in the interval $[0, 2\pi)$. To confirm this, we compute the histogram of relative phases, shown in Fig. 7.17(d). For this calculation, we take into account of the spatial distribution of the trapped atoms along the nanofiber, see subsection 7.3.5, and use it to infer the distribution of the two-atom distances.

We now model the expected count distribution for two atoms. The step by step procedure is explained in Fig. 7.18. We first consider the case with only common-mode variations, where the amplitudes of the fields scattered by the two atoms vary from shot to shot, but are always equal to each other. We expect such common-mode variations from the drifts of the filter cavity, the excitation laser power, or the trapping potential. We show the count distribution with common-mode variations as the red dotted line in Fig. 7.17(c). We normalize the distribution to have the same integral as the total number of SPCM counts in the experimental data in Fig. 7.17(c).

To simulate the count distribution with common-mode variations, we first compute the count

Die approbierte gedruckte Originalversion dieser Dissertation ist an der TU Wien Bibliothek verfügbar.
The approved original version of this doctoral thesis is available in print at TU Wien Bibliothek.
TU Bibliothek Your knowledge hub WIEN

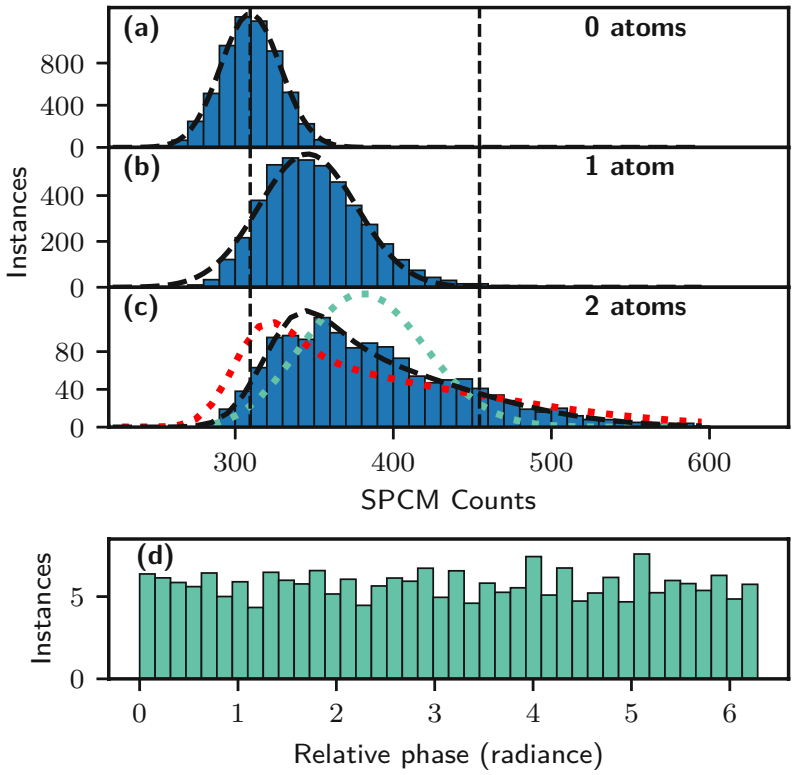

Figure 7.17: SPCM count distribution versus number of trapped atoms. Atoms are exposed to a near-resonant excitation laser field. A fraction of the atomic fluorescence is scattered into the guided mode of the nanofiber. From (a) to (c), the histogram is conditioned on having zero, one, two atoms detected in images taken with the camera, respectively. We fit the data in panel (a) and (b) with Gaussian functions to extract the photon counts of the background and the one-atom signals. We use the fitted values to simulate the count histogram of the two-atom signal. The grey and red dash-dotted lines correspond to the two limiting cases assuming common-mode and differential-mode variations of the two atom-scattered light fields, respectively. The black dashed line corresponds to a fit to the experimental data, which has a weight of 71 % common-mode variations and 29 % differential-mode variations. (d) Simulated histogram of the relative phases between the light fields scattered by two atoms into the nanofiber.

histogram of one-atom signal without Poissonian and background noise following the procedure described in subsection 7.3.1. As a starting point for this calculation, we use the count histogram of background and one-atom signal shown in Fig. 7.17(b). We find the one-atom signal's count histogram by removing the background noise's contribution which is given by the count histogram shown in Fig. 7.17(a). Same as the procedure shown in subsection 7.3.1, we approximate the count histograms with their fitted Gaussian distributions. This way, we can easily deduce the technical noise of the one-atom signal which cause the Gaussian distribution to be

Die approbierte gedruckte Originalversion dieser Dissertation ist an der TU Wien Bibliothek verfügbar.
The approved original version of this doctoral thesis is available in print at TU Wien Bibliothek.
TU Bibliothek Your knowledge hub WIEN

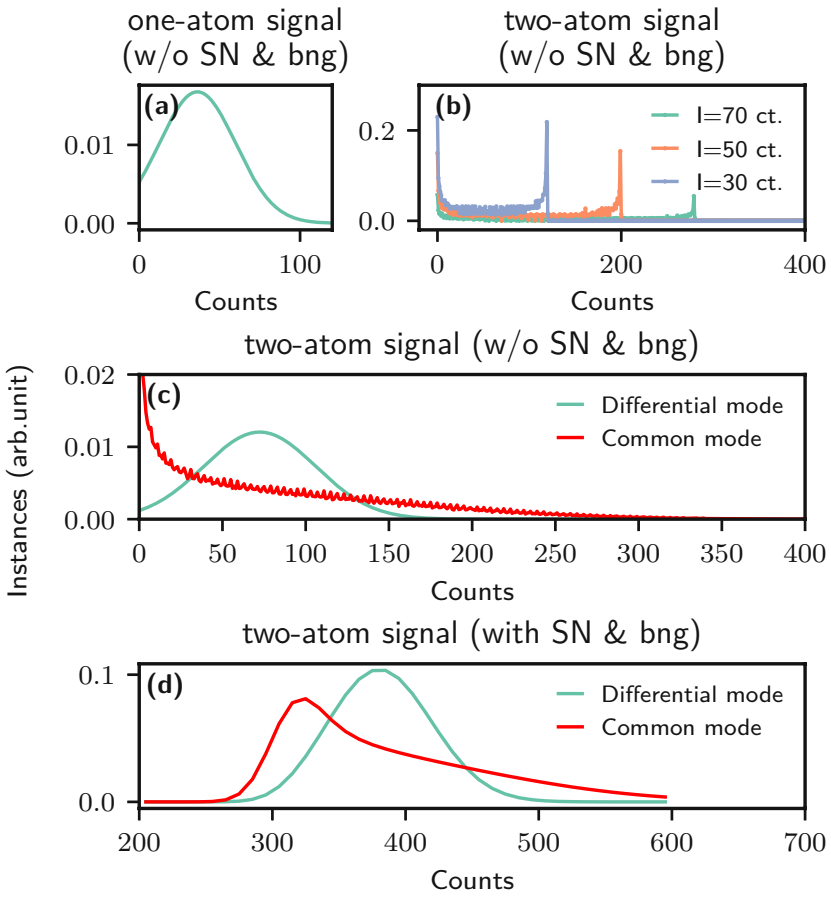

Figure 7.18: Modeling of the SPCM count distribution of two atom-scattered light. (a) Count distribution of one-atom signal. Compare to Fig. 7.17(a), Poissonian and background noise are removed here. (b) Examples of two-atom signal's count histograms with different values of one-atom signal I. For each count histogram , the two maxima at 0 and 4I correspond to the case of perfect destructive and constructive interference, respectively. The histograms of two-atom signal are weighted based on the count distribution of one-atom signal shown in panel (a). (c) Red and grey lines indicate the count distribution of two-atom signal with common-mode and differential-mode variations, respectively. To generate the count distribution with common-mode variations, we sum over count histograms of two-atom signal such as the three examples shown in panel (b). The count distribution with differential-mode variations can be obtained using the incoherent sum of two count distributions of single atoms. We generate the count distribution with differential-mode variations by taking the incoherent sum of two one-atom signal.(d) Same count distributions as panel (c) but with Poissonian and background noise added.

Die approbierte gedruckte Originalversion dieser Dissertation ist an der TU Wien Bibliothek verfügbar.
The approved original version of this doctoral thesis is available in print at TU Wien Bibliothek.
TU Bibliothek Your knowledge hub WIEN

broader than the shot-noise limited width.

We then calculate two-atom signal's count histograms at every given SPCM counts of one-atom signal, see Fig. 7.18(b). In this calculation, we sample through all possible phases between two atom-scattered light fields, see Fig. 7.17(d). We weight the two-atom signal's count histograms based on the corresponding instances in the count histogram of one-atom signal (without Poissonian and background noise). After summing the two-atom signal's weighted count histograms, we have the common-mode count distribution in Fig. 7.18(c). In Fig. 7.18(d), We add the Poissonian and background noise to the common-mode count distribution.

The final common-mode count distribution has a similar asymmetry compared to the experimental data in Fig. 7.17(c). We attribute the deviation between the experimental data and this theory prediction to the differential-mode variations. We can expect differential-mode variations from an out of phase thermal motion of the two atoms in the radial direction of the trapping potential which corresponds to a variation of the atom-nanofiber coupling strengths. Moreover, a spatial inhomogeneity of the excitation light field intensity would also lead to two unequal scattered field strengths. In the extreme case of an on-off modulation of the coupling strengths, the count distribution with the differential-mode variations is given by the incoherent sum of the two single-atom signals, see the green dotted lines in Fig. 7.17(c), which also deviates from the experimental data. We compute the count distribution with the differential-mode variations by taking the convolution of two one-atom signal's count distributions, see Fig. 7.18(c).

Taking into account both the common-mode and differential-mode variations and fitting their weight, we find very good agreement between the simulated distribution of SPCM counts and the experimental data for 71 % common-mode and 29 % differential-mode variations, see the black dashed line in panel (c).

Moreover, we use a Gaussian fit to locate the two-atom positions, and determine the atom-atom distance with a precision of $\sim$0.7 µm, see subsection 7.3.3. We sort the SPCM counts by the atom-atom distance, and use this data to compute the power spectral density (PSD) of the Fourier spectrum of the two-atom interference pattern, see Fig. 7.19(b). From the PSD, we can infer the spatial frequency of the two-atom interference pattern. If the inter-atomic distance can be varied continuously (denoted as d_c), the condition for constructive interference is given by the incident angle θ, the wavenumber of the excitation light in free-space and the wavenumber of the scattered light in the nanofiber-guided mode (see Fig. 7.19(b)):

$$k_{nf}\sin(\theta)d_c + k_0 d_c = 2\pi. \tag{7.6}$$

The corresponding spatial frequency f_c is then:

$$f_c = \frac{1}{d_c} = \frac{(k_{nf}\sin(\theta) + k_0)}{2\pi}. \tag{7.7}$$

However, the lattice spacing Δz is fixed in our experiment. This leads to a discrete sampling frequency of $f_s = \frac{1}{\Delta z}$. Therefore, the Fourier spectrum will have multiple peaks at $f^m_{alias} = f_c + m f_s$ due to the aliasing effect, where m is an integer number. The aliasing effect can be easily understood considering the value of $\sin(2\pi(f_c + m f_s)n\Delta z)$ is constant with respect to any integer m, where $n\Delta z$ is the distance between two trapped atoms, i.e., an integer multiple of Δz. As shown in Fig. 7.19(b), the Gaussian center of the peak in the Fourier spectrum is at

Die approbierte gedruckte Originalversion dieser Dissertation ist an der TU Wien Bibliothek verfügbar.
The approved original version of this doctoral thesis is available in print at TU Wien Bibliothek.
TU Bibliothek Your knowledge hub WIEN

$0.274\,\mu\mathrm{m}^{-1}$. This peak position corresponds to $\theta = 20°$, which is in good agreement with our experimental geometry.

The results in this section are obtained in the following way: For each experimental cycle, we image the atoms for 11 frames with an exposure time of $150\,\mathrm{ms}$ per frame. In addition, we collect the background signal without trapped atoms at the end of each imaging cycle. To reduce the number of instances where two closely-spaced atoms are detected as one, we only take atoms where its peak value from the convoluted, background-corrected image is less than 80 pixel counts. In addition, to reduce outliers, we only take data where the error of fitted distance is less than 0.3 pixels or $1.6\,\mu\mathrm{m}$.

Die approbierte gedruckte Originalversion dieser Dissertation ist an der TU Wien Bibliothek verfügbar.
The approved original version of this doctoral thesis is available in print at TU Wien Bibliothek.
TU Bibliothek Your knowledge hub WIEN

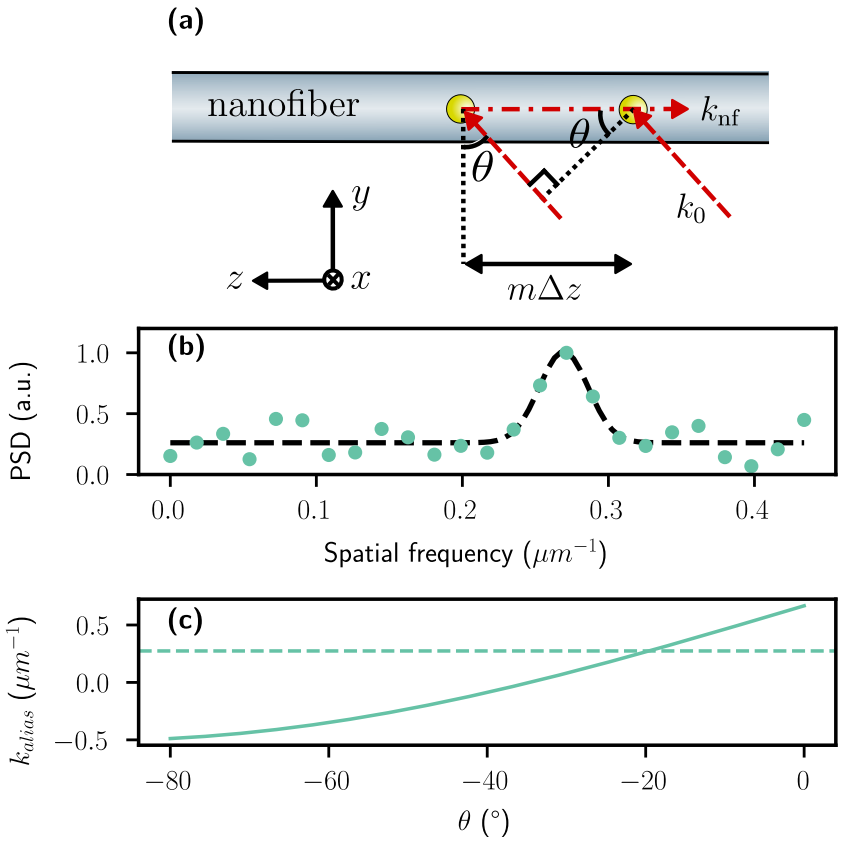

Figure 7.19: Spatial interference of nanofiber-coupled light. (a) Schematic diagram of incident excitation light field and nanofiber-trapped atoms. The incident light is indicated by the red dashed arrows. We measure the photon number of the scattered light coupled to the nanofiber-guided mode and propagating in the $-z$ direction. This scattered light is indicated by the red dash-dotted arrow. The trapped atoms, indicated by the yellow circles, are separated by an integer multiple of the lattice spacing $m\Delta z$. (b) Spatial Fourier spectrum of the interference pattern from the light scattered by two atoms. Conditioned on the two-atom detection from the camera image, we record the SPCM counts of the atom-scattered light that are coupled into the nanofiber-guided mode. We sort the counts by the atom-atom distance inferred from the camera image. We take the resulting data from this analysis to compute the spatial Fourier spectrum of the interference pattern using the Blackman window function. The PSD in the figure label stands for power spectral density. We see a clear peak in the Fourier spectrum with a spatial frequency of $\sim 0.27\,\mu\mathrm{m}^{-1}$, in good agreement with the theory prediction for our experimental conditions. (c) The expected spatial frequency as a function of the incident angle of the excitation light, θ. The horizontal dashed line indicates the measured spatial frequency of $\sim 0.27\,\mu\mathrm{m}^{-1}$.

Die approbierte gedruckte Originalversion dieser Dissertation ist an der TU Wien Bibliothek verfügbar.
The approved original version of this doctoral thesis is available in print at TU Wien Bibliothek.
TU Bibliothek Your knowledge hub WIEN

7.6 Summary and outlook

We demonstrate in this chapter, for the first time, imaging of individual atoms interfaced with an optical nanofiber. We use DRC to keep trapped atoms close to the motional ground state while collecting the atom-scattered light on a camera. We obtain a sufficient ratio of signal-to-noise to identify an atom within $150\,\mathrm{ms}$, well below the trapping lifetime during imaging. We summarize the figures of merit in the following table:

Probability of detecting a single atom	97.5 %
Probability of false detection per image	7 %
Percentage of the detected atoms that are lost after detection	9 %
$1/e$ width of PSF	$10\,\mu\mathrm{m}$
Error of atom position (Gaussian PSF)	$0.5\,\mu\mathrm{m}$

Table 7.1: Figures of merit for image detection. Here we use a detection threshold of 18 pixel counts and an image integration time of $150\,\mathrm{ms}$.

Our imaging capabilities provide new avenues for studying atom-light interactions using a nanophotonic interface. The imaging of individual atoms allows us to measure precisely the number of a few trapped atoms, and to determine the inter-atomic distance with sub-wavelength precision. In this chapter, we demonstrate two immediate applications. First, we measure the transmission of a resonant fiber-guided probe light conditioned on zero, one, two, and three trapped atoms. We extract the extinction atom by atom, which is in good agreement with the exponential scaling of Beer-Lambert's law. Second, we observe interference of nanofiber-coupled light fields scattered by the two nanofiber-trapped atoms. We observe interference by measuring the SPCM counts of the nanofiber-coupled light fields as a function of the atomic distance. The inferred spatial modulation period is well within our expectation.

A technical improvement in the near future is to increase the collection efficiency of the imaging system. A straightforward method is to increase the NA of the imaging objective, which currently limits the collection efficiency of the scattered photons. If we can increase the NA of our setup from 0.29 to a current state-of-the-art value of 0.92 [115], the collection efficiency of the imaging system improves from 2.1 % to 28 % (see section 7.1), a factor of $\sim$13 increase. At this NA, ideally only $12\,\mathrm{ms}$ of exposure time is required to reach a comparable imaging quality to that shown in this chapter.

Furthermore, given the current technology, it is feasible to achieve imaging resolution to site resolve nanofiber-trapped atoms. This would minimize the number of instances where two closely spaced atoms are erroneously detected as one atom, and allow us to investigate atom-light

Die approbierte gedruckte Originalversion dieser Dissertation ist an der TU Wien Bibliothek verfügbar.
The approved original version of this doctoral thesis is available in print at TU Wien Bibliothek.
TU Bibliothek Your knowledge hub WIEN

interaction with higher filling factors of the nanofiber-based trap. In addition, this would improve the precision of determining the inter-atomic distance. For conventional imaging techniques (non-super resolution), site-resolved imaging requires an optical resolution that is better than the lattice spacing, which is $\sim$0.5 µm in our setup. The diffraction-limited resolution of an imaging system is given by $d = \lambda/(2\mathrm{NA})$, where λ is the wavelength of the imaging light. For our imaging setup, the diffraction-limited resolution is $\sim$1.5 µm, i.e., about 3 times larger than the lattice spacing. By employing a state-of-the-art microscope objective with $NA = 0.92$, the diffraction-limited resolution using a D_2 imaging light is at ~ 463 nm and below the lattice spacing in our setup. In the current work, the experimentally determined PSF has a $1/e$ radius of $\sim$10 µm, which is much larger than the PSF radius of $\sim$0.835 µm expected if our imaging system was operating at the diffraction limit. We attribute this discrepancy to aberrations of the imaging system. The microscope objective in our setup is mechanically fixed to the vacuum chamber and its alignment could not be optimized for the single atom imaging experiment. Therefore, an obvious improvement is to mount the microscope objective onto a mechanical stage for fine positioning and alignment.

When the interaction between the nearest lattice sites is not of interest, e.g., for studies of atom tunneling, we can increase the lattice spacing by employing a larger wavelength of the red-detuned standing trapping light field. For example, if we select 1.6 µm wavelength for the red-detuned light field, we could reach a similar trapping depth using a higher red-detuned light field intensity. This would increase the lattice spacing by 60 % to $\sim$ 800 nm spacing. Such a spacing would loosen the requirements for site-resolved imaging of trapped atoms. In a different approach, we can use atom trapping based on two-mode interference in ultrathin optical fibers [116]. When the trapping potential is formed by two co-propagating blue-detuned light fields with different mode orders, the trapping site spacing can be given by the beat length of the two modes. By employing different combinations of modes and laser powers, site spacings on the order of 10 µm can be realized using a nanofiber diameter of 400 nm and trapping light wavelength at $\sim$850 nm, enabling single-site resolution in our current imaging setup.

Die approbierte gedruckte Originalversion dieser Dissertation ist an der TU Wien Bibliothek verfügbar.
The approved original version of this doctoral thesis is available in print at TU Wien Bibliothek.
TU Bibliothek Your knowledge hub WIEN

CHAPTER 8

Conclusion & Outlook

In this thesis, the coupling between spin and motional degrees of freedom in nanofiber-trapped atoms has been investigated experimentally and theoretically.

We described the nanofiber-based two-color trap for laser-cooled atoms. In particular, we showed the polarization and mode profile of a nanofiber-guided light field. We discussed the laser configuration of the nanofiber-based cold-atoms trap, which consists of a running blue-detuned light and a pair of counter-propagating red-detuned light. We also summarized the experimental procedure to prepare and load cold atoms into the nanofiber-based atom traps, as well as the probing scheme to measure the optical density of the trapped atoms. We described the gradient of fictitious magnetic fields that originate from the trapping light fields and, in particular, their gradient over the trap volume. We showed these gradients lead to the coupling between spin and motional degrees of freedom.

We demonstrated that the spin-motion coupling can be utilized to perform degenerate Raman cooling. We presented fluorescence spectra of the nanofiber-trapped atoms that are cooled close to the motional ground state. In addition, we showed that the spin-motion coupling in the nanofiber system can be treated as a mechanical analog of the Dicke model. We demonstrated that the spin-motion coupling strength corresponds to the ultrastrong-coupling regime of light-matter interaction. Finally, we demonstrated imaging of single nanofiber-trapped atoms. To demonstrate the usefulness of atom imaging, we showed two-textbook experiments: testing Beer-Lambert's law atom by atom and observing interference of two nanofiber-coupled light fields emitted from two nanofiber-interfaced atoms.

By preparing atoms close to the motional ground states, the atoms are at a well defined and uniform atom-light coupling strength. Thereby, inhomogeneous broadening of the atomic transitions due to thermal motion in the trap is suppressed. In conjunction with imaging of single atoms, these two experiments mark unprecedented control of cold atoms trapped near a nanophotonic structure. Our findings provide new avenues to study complex light-matter interaction phenomena atom-by-atom.

For future experimental studies, the interference measurements of the nanofiber-interfaced atoms provide an excellent basis for looking at collective, waveguide-mediated effects [117–

Die approbierte gedruckte Originalversion dieser Dissertation ist an der TU Wien Bibliothek verfügbar.
The approved original version of this doctoral thesis is available in print at TU Wien Bibliothek.
TU Bibliothek Your knowledge hub WIEN

119]. Our results pave the way for implementing position-resolved real-time feedback and for the step-by-step assembly of quantum matter built from nanostructure-based lattices of atoms and photons [120]. Finally, the demonstrated atom imaging and cooling techniques will be assets, for example, for the investigation of self-organization phenomena [121, 122], including in the chiral domain [123, 124].

Die approbierte gedruckte Originalversion dieser Dissertation ist an der TU Wien Bibliothek verfügbar.
The approved original version of this doctoral thesis is available in print at TU Wien Bibliothek.
TU Bibliothek Your knowledge hub WIEN

CHAPTER 9

Appendix

9.1 Heating mechanisms of nanofiber-trapped atoms

One of the main challenges to achieving full quantum control of the nanofiber-trapped atoms is to mitigate heating in the nanofiber-based traps. The heating rates in our experimental setup are 0.3 quanta/ms in the y (azimuthal) degree of freedom (DOF) and 0.7 quanta/ms in the z (axial) DOF [23, 58]. The high heating rates in our setup results in a trapping lifetime of $50\,\mathrm{ms}$. The trapping lifetimes of the nanofiber-based cold-atoms from groups are $\sim$10 ms, indicating similar or higher heating rates [125, 126]. In this section, we discuss the heating mechanisms listed in the following:

- Off-resonant scattering of the trapping laser fields by the atoms
- Raman scattering in the fiber
- Blackbody radiation and Johnson–Nyquist noise
- Mechanical modes of the nanofiber and their coupling to guided light fields
- Brillouin scattering in the fiber

9.1.1 Off-resonant scattering of the trapping laser fields by the atoms

We consider off-resonant scattering from the trapping light fields. Following the recipe shown in chapter 2, we first calculate the intensities of trapping light fields at the position of the trap potential minima. We then compute the off-resonant scattering rate which is given by the intensities and the detuning of trapping light fields (see equation 4.30 in chapter 4). Finally, we convert the off-resonant scattering rate to the recoil heating rate, which amounts to ~ 2 quanta/s for z DOF, far less than the measured heating rates in our experiment setup.

Die approbierte gedruckte Originalversion dieser Dissertation ist an der TU Wien Bibliothek verfügbar.
The approved original version of this doctoral thesis is available in print at TU Wien Bibliothek.
TU Bibliothek Your knowledge hub WIEN

9.1.2 Raman scattering in the fiber

The fiber-guided trapping light fields introduce Raman scattering in the fused-silica-based fiber. For an order of magnitude estimate, we focus on the contribution of the blue-detuned trapping light since it has much larger power than the red-detuned trapping light. The Raman scattering induced by a fiber-guided laser field of $780\,\mathrm{nm}$ wavelength has been measured and the Stokes-scattered light was recorded using a spectrometer. The test fiber in this measurement was the same type as the one used in our experiment (Liekki Passive-6-125). From this measurement and other system parameters, we can infer that a single nanofiber-trapped Cesium atom absorbs about 50 photon/s of the Raman light, corresponding to a heating rate of 0.7 quanta/s, which is negligible compared to the measured heating rates in our experimental setup.

9.1.3 Blackbody radiation and Johnson–Nyquist noise

Blackbody radiation and Johnson–Nyquist noise are fundamental processes which are prominent in many cold atom systems [127]. For example, in the work by Henkel et al. [127], the heating rate is computed for a spin confined in a harmonic potential that is in close proximity to a material half space. For a trap frequency of $100\,\mathrm{kHz}$, the expected heating rate is only at $\sim 10^{-14}$ quanta/s for an atom 200 nm away from a glass substrate, which is negligible compared to the measured heating rates in our experiment. The small Johnson–Nyquist noise related heating rate originates from the low electrical conductivity of glass. Thus, we conclude that Blackbody radiation and Johnson–Nyquist noise are negligible contributions for the heating rates of nanofiber-trapped atoms.

9.1.4 Mechanical modes of the nanofiber and their coupling to guided light fields

The nanofiber can sustain three different types of mechanical modes: torsional modes, flexural modes, and longitudinal modes. In the theory work by Hummer et.al., the dominant heating process stems from the optomechanical coupling of the optically trapped atoms to the continuum of thermally occupied flexural mechanical modes of the waveguide structure, while the torsional mode's contribution can be neglected [57]. The flexural modes have a quadratic dispersion relation that gives rise to a high density of modes near low frequencies. This results in significant heating estimates. Unfortunately, both the resonance frequencies and the Q-factors of flexural modes and longitudinal modes are not yet experimentally accessible. In this subsection, we check experimentally that the contribution from torsional modes is indeed negligible.

The contribution of torsional modes to the heating process can be inferred from resonance frequencies and mechanical Q-factors. To extract these numbers, we experimentally characterize the polarization modulation of a nanofiber-guided light field at the wavelength of $1064\,\mathrm{nm}$. We carry out this experiment in the same nanofiber cold atom system with which all other experiments of the thesis have been conducted. We set this light field to be quasi-linearly polarized at the waist of the nanofiber. To see the polarization modulation, we add a linear polarizer after the light is transmitted through the nanofiber. We measure the intensity modulation of the nanofiber transmission after the linear polarizer using a low noise photodiode (see Fig. 9.1). We record the

Die approbierte gedruckte Originalversion dieser Dissertation ist an der TU Wien Bibliothek verfügbar.
The approved original version of this doctoral thesis is available in print at TU Wien Bibliothek.
TU Bibliothek Your knowledge hub WIEN

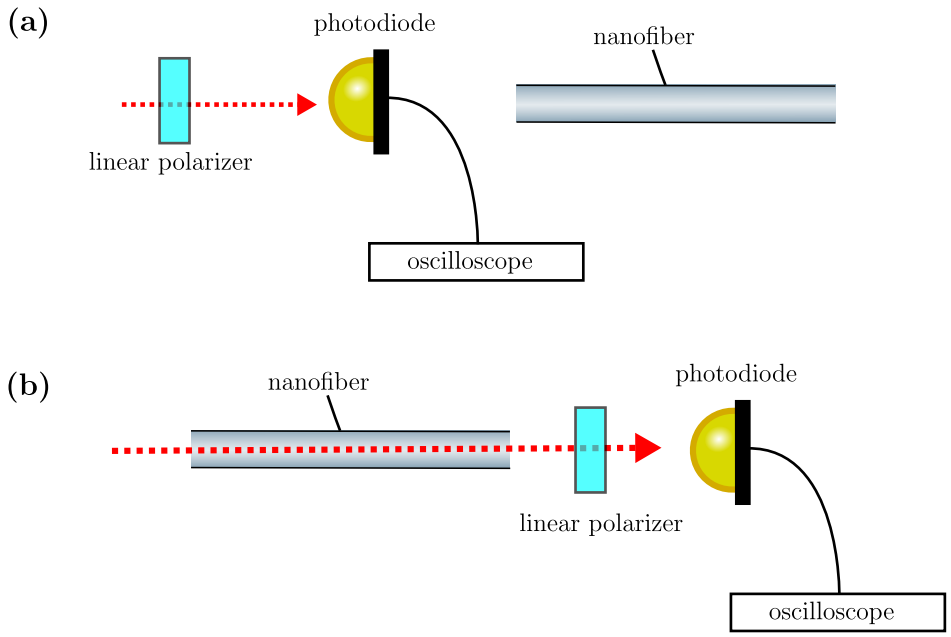

Figure 9.1: Experimental setup to measure the Q factors of mechanical modes of the nanofiber. (a) The intensity of a trapping light field is measured before the nanofiber and after the linear polarizer. (b) The intensity of a trapping light field is measured after the nanofiber and the linear polarizer. By comparing the Fourier spectrum measured in setup (a) and (b), we find frequency components which originate from the optomechanical coupling of the nanofiber-guided light to the mechanical modes of the nanofiber.

time domain signal on the oscilloscope and calculate the power spectrum of the fractional intensity fluctuation. To identify the peaks in the spectrum that originate from the torsional modes of the nanofiber, we also measure the spectrum before the nanofiber. In addition, we measure spectra without either the laser light or the linear polarizer. In absence of the linear polarizer, the peaks in the spectrum correspond to intensity fluctuations. The spectra are shown in Fig. 9.2. The additional peaks observed with the linear polarizer indicate the existence of the torsional mechanical modes of the nanofiber at 258 kHz and 375 kHz. Using Gaussian fits, we find the Q-factor for the modes are at 258 kHz and 375 kHz are 5400 ± 100 and 58000 ± 5000, respectively (see Fig. 9.3). The uncertainty of the Q-factors originate from the Gaussian fits.

The two observed frequencies for the torsional modes are far higher than the typical frequencies expected from technical noise. We assume the torsional modes are thermally occupied. To estimate the heating rate from the torsional modes, we consider the position fluctuation of the nanofiber-based trapping sites that originates from the strain-optic effect of the torsional mode of the nanofiber.

We calculate the heating rate due to position fluctuations following the paper from Savard et al. [128]:

Die approbierte gedruckte Originalversion dieser Dissertation ist an der TU Wien Bibliothek verfügbar.
The approved original version of this doctoral thesis is available in print at TU Wien Bibliothek.
TU Bibliothek Your knowledge hub WIEN

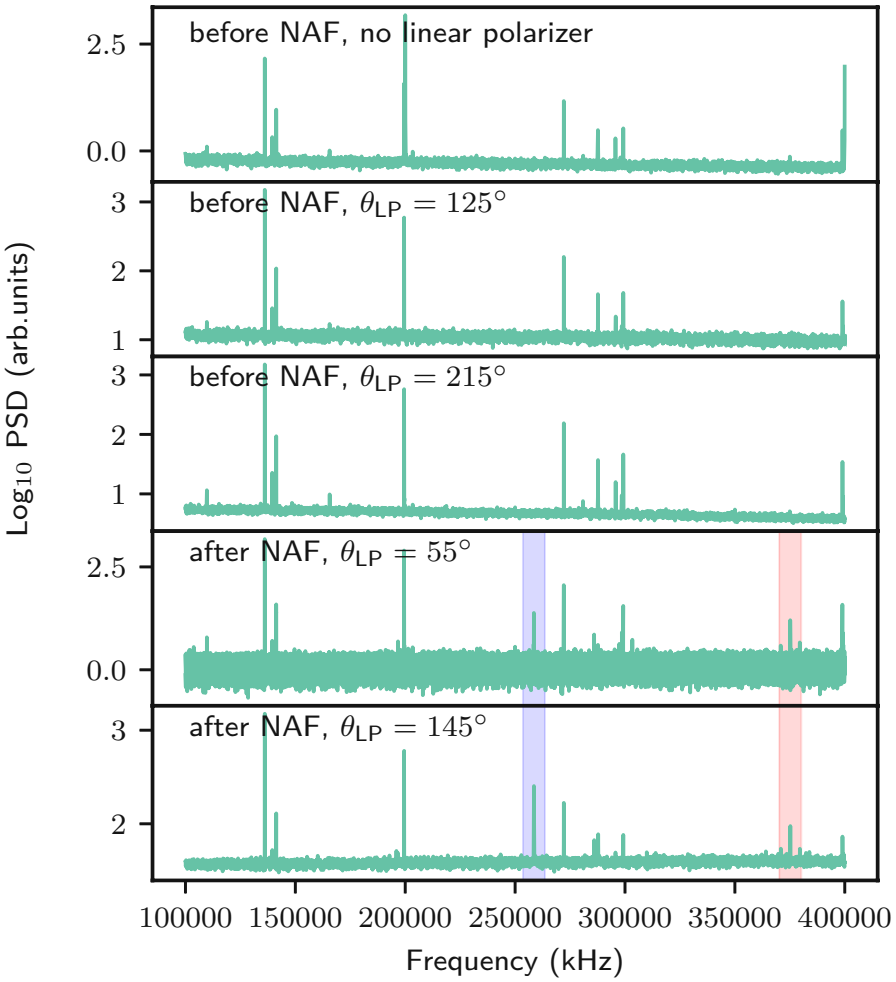

Figure 9.2: Power spectra of a nanofiber-guided light at 1064 **nm.** (a) Spectrum measured before the nanofiber and without linear polarizer. The observed peaks correspond to intensity fluctuation. (b)-(c) Spectra measured before the nanofiber and after a linearly polarizer. Here we check if there are any polarization fluctuations of the light before coupling into the nanofiber. The axes of polarization of the linear polarizer are orthogonal in the two panels, i.e., (b) $\theta_{\mathrm{LP}} = 125°$ and (c) $\theta_{\mathrm{LP}} = 215°$. (d)-(e) Spectra measured after transmission in the nanofiber and after a linearly polarizer at two orthogonal axes of polarization. The additional peaks at $258\,\mathrm{kHz}$ and $375\,\mathrm{kHz}$ observed in panel (d) and (e) are induced by the mechanical modes of the nanofiber.

$$\left\langle \dot{E} \right\rangle = \frac{\pi}{2} M_{\mathrm{cs}} \omega_{\mathrm{tr}}^4 S_x(w) \,, \tag{9.1}$$

where ω_{tr} is the trap frequency, M_{cs} is the mass of a cesium atom, and S_x is the power spectrum of the position fluctuations.

Die approbierte gedruckte Originalversion dieser Dissertation ist an der TU Wien Bibliothek verfügbar.
The approved original version of this doctoral thesis is available in print at TU Wien Bibliothek.
TU Bibliothek Your knowledge hub WIEN

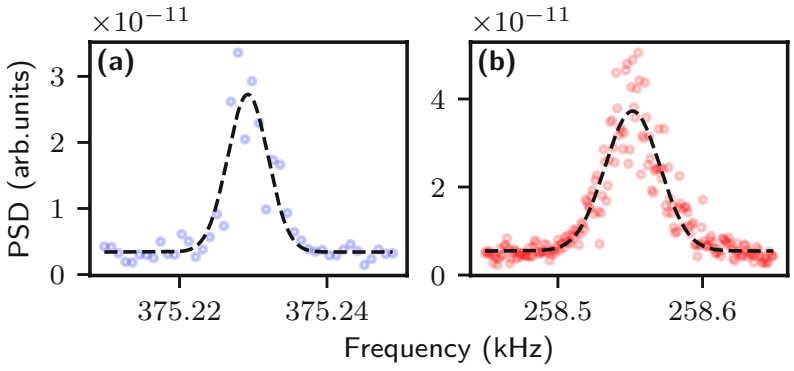

Figure 9.3: (a)-(b) Spectrum near 258 kHz and 375 kHz, respectively. The Q-factor is obtained using the ratio between the fitted peak frequency and the full width at half maximum

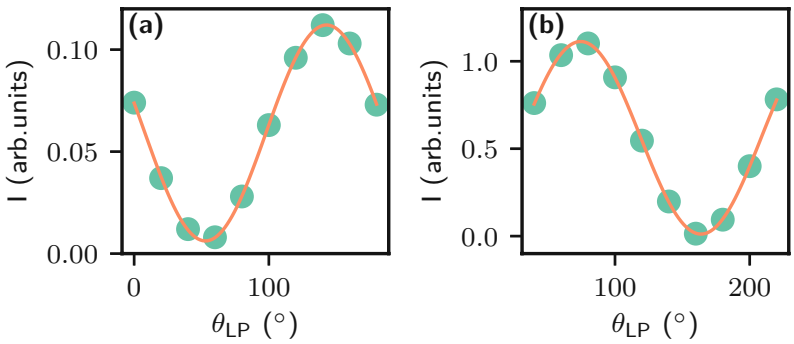

Figure 9.4: (a)-(b) Intensity of the red-detuned trapping light field as a function of the angle of the linear polarizer measured before and after the nanofiber, respectively.

The power spectrum of the position fluctuation $S_x(w)$ is proportional to the power spectrum of the angle fluctuation of the polarization of the guided light $S_{\phi_{0,n}}(\omega)$ by a constant factor:

$$S_x(w) = S_{\phi_{0,n}}(\omega) R^2 \,, \tag{9.2}$$

where R is trapped atom's radial distance from the center axis of nanofiber.

The power spectrum of the angle fluctuation is proportional to the variance of the maximum displacement $\langle \phi_{0,n}^2 \rangle$:

$$S_{\phi_{0,n}}(\omega) = \frac{4 \langle \phi_{0,n}^2 \rangle}{\omega} \frac{\xi}{([\omega/\omega_{0,n}]^2 - 1)^2 + \xi^2} \,, \tag{9.3}$$

where $\langle ... \rangle$ denotes the time average, ξ is the mechanical damping rate which is inverse of the Q factor, $\omega_{0,n}$ is the frequency of the torsional modes.

Die approbierte gedruckte Originalversion dieser Dissertation ist an der TU Wien Bibliothek verfügbar.
The approved original version of this doctoral thesis is available in print at TU Wien Bibliothek.
TU Bibliothek Your knowledge hub WIEN

The variance of the maximum displacement is:

$$\langle \phi_{0,n}^2 \rangle = \frac{k_B T}{\omega_{0,n}^2 I_{\text{eff},n}}. \tag{9.4}$$

The effective moment of inertia I_{eff} is estimated to be $4.6 \times 10^{-26}\text{kg.m}^2$ for the first torsional mode. We infer this value from the Ph.D thesis of C.Wuttke [129], where a nanofiber with similar dimensions to the one in our experiment is described. We use the same value of I_{eff} for the second torsional mode. This would results in an overestimation of the heating rate since the higher frequency modes should have a higher moment of inertia, which lower the heating rate. With this assumption, and taking literature values for the strain-optical coupling coefficients, we find a heating rate of ~ 0.8 quanta/s, i.e., two orders of magnitude smaller than the measured heating rates.

9.1.5 Brillouin scattering in the fiber

The acoustic motion of the nanofiber can also induce Brillouin scattering of the guided light fields. For this to happen, the optical mode and an acoustic mode of the nanofiber need to be phase matched [130]. For a nanofiber radius of $250\,\text{nm}$ radius and guide light field of $780\,\text{nm}$ wavelength, the first phase matching condition for Brillouin backscattering occurs for an acoustic wave with a frequency of $\sim$11 GHz and spectral width of a few $10\,\text{MHz}$. The next resonance occurs at higher acoustic frequencies. In this subsection, we consider three possible Brillouin scattering induced heating processes: heating from two photon transitions, parametric heating and resonant heating originating from trap potential fluctuation.

Heating from two photon transitions

The Brillouin-scattered (BS) light can in principle drive two-photon transitions between different internal states of the nanofiber-trapped cold atoms together with an additional pump light. When the trapping potential has a dependency on the internal states (as it can be the case for nanofiber-based traps, see [41]), this could lead to heating [97]. The only internal atomic states with a comparable energy separation are the two hyperfine ground-state manifolds at $\sim$9 GHz, which is still $\sim$2 GHz away from the nearest two-photon detuning at $\sim$11 GHz. Furthermore, we estimate that the BS light is at the sub-nW level. Consider the BS light's low power, narrow spectral width, and large detuning, the heating induced by the two-photon transitions is negligible for the nanofiber-trapped atoms. For the standard fiber part, the phase matching condition occurs at $\sim$22.3 GHz, which results in an even larger two-photon detuning. The scattered power in the bulk fiber is found to be in the sub-nW level. Therefore, we consider this heating process to be insignificant in our experimental setup.

Resonant and parametric heating

The BS light fields originate from two red-detuned trapping light fields form an additional standing wave (SW) that has a randomly fluctuating phase with respect to the original trapping SW.

Die approbierte gedruckte Originalversion dieser Dissertation ist an der TU Wien Bibliothek verfügbar.
The approved original version of this doctoral thesis is available in print at TU Wien Bibliothek.
TU Bibliothek Your knowledge hub WIEN

The SW formed from BS results in a stochastic modulation of the trapping potential. In particular, the change in the trapping frequency in the z DOF leads to parametric heating. In comparison, the change of the potential minima along the z-axis leads to resonant heating.

We first consider resonant heating that originates from BS-induced position fluctuations of the trapping potential minimum. The heating rate due to fluctuation of the trap minimum is [128]:

$$\langle \dot{E} \rangle = \frac{\pi}{2} M \omega_{\text{tr}}^4 S_x(\omega_{\text{tr}}), \tag{9.5}$$

where M is the mass of the trapped cesium atom, ω_{tr} is the trap frequency, and S_x is the power spectral density of the position fluctuation.

As seen in equation (9.5), only position fluctuation at the trap frequencies contributes to this heating process. If the forward and backward propagating BS red light have a relative frequency difference of $\Delta\nu$, the combined travels at the speed of $\frac{\pi\nu}{k}$, where k is the wavenumber of the nanofiber-guided light.

Depending on the relative phase between the trap potential formed by red trapping light and the BS fields, we can have a different displacement of the trap minima along the z-direction. Since the BS light is $\sim$10 GHz detuned from the trapping light field, we neglect the mismatch between the periodicity between the SW formed from BS light and the trapping SW. The maximum displacement occurs when the BS light form a SW at $\pi/2$ out of phase relative to the trapping SW:

$$y = (I_1 - I_2)(1 - \cos(kz)) + I_2 \sin(kz), \tag{9.6}$$

where I_1 is the intensity of the red trapping beams, I_2 is the intensity of the BS light. The ratio I_1/I_2 is on the order of 10^6.

To simplify, we expand equation 9.6 in Taylor series up to the first order:

$$I_{\text{total}} = (I_1 - I_2)(kz)^2/2 + I_2 k(z). \tag{9.7}$$

We find the trap displacement ϵ_{max} by differentiating I_{total} with respect to z:

$$dI_{\text{total}}/dz = (I_1 - I_2)(k^2 z) + I_2 k = 0 \rightarrow \epsilon_{max} = \frac{I_2}{k(I_1 - I_2)} = \sim 0.8 \times 10^{-13}\text{m}. \tag{9.8}$$

The one-sided power spectrum is defined as [128]:

$$S_x(\omega) = \frac{2}{\pi} \int_0^\infty d\tau \cos(\omega\tau) \langle \epsilon(t)\epsilon(t+\tau) \rangle \tag{9.9}$$

To have an order of magnitude estimate of the heating rate, we normalize the frequency-integrated PSD of the individual BS light fields to the root-mean square value of the relative intensity noise:

$$\int_0^\infty S_x(\omega) d\omega = \langle \epsilon^2(t) \rangle = \epsilon_0^2, \tag{9.10}$$

Die approbierte gedruckte Originalversion dieser Dissertation ist an der TU Wien Bibliothek verfügbar.
The approved original version of this doctoral thesis is available in print at TU Wien Bibliothek.
TU Bibliothek Your knowledge hub WIEN

where ϵ_0 is the root-mean-square position fluctuation.

We use the maximum displacement $\epsilon_0 = \epsilon_{max}$ as an upper estimate of the heating rate. Furthermore, we approximate $S_x(\omega)$ as a boxcar function with a spectral width of $\Delta\omega$ and is centered on the trap frequency, i.e., $S_x(\omega) = 0$ for $|\omega - \omega_{tr}| > \Delta\omega/2$, and $S_x(\omega) = \epsilon_0^2/\Delta\omega$ for $|\omega - \omega_{tr}| \leq \Delta\omega/2$.

Using this approximation, equation 9.5 becomes:

$$\langle \dot{E} \rangle = \frac{\pi}{2} M \omega_{\text{tr}}^4 \frac{\epsilon_0^2}{\Delta\omega}. \tag{9.11}$$

The heating rate can be expressed in term of motional quanta [128]:

$$\frac{\langle \dot{E} \rangle}{\hbar\omega_{\text{tr}}} = \frac{\pi}{2} M \omega_{\text{tr}}^3 \frac{\epsilon_0^2}{\hbar\Delta\omega}. \tag{9.12}$$

The trap frequency in the z-direction in our setup is $\sim$230 kHz. The spectrum of BS light for an experimental setup comparable to ours has been published [131]. There, a Gaussian spectrum with an FWHM of $\sim$ 25 MHz was found. The PSD of the standing wave formed from the BS light is the (appropriately normalized) convolution of the two PSDs of the two BS fields, which results in a factor of $\sqrt{2}$ increase in the FWHM. Using this FWHM, we find a heating rate of $\sim 3 \times 10^{-7}$ quanta/s, which is 9 orders of magnitude smaller than the one measured in our experiment.

We now consider parametric heating resulting from BS-induced fluctuations of the trap frequency in the z DOF ω_z. When the potential minimum of the trapping SW coincides with a potential minimum(maximum) of the SW formed from BS, the resulting trap frequency in the z DOF is increased(decreased). For heating due to intensity fluctuation, or parametric heating, the heating rate is given by [128]:

$$\langle \dot{E} \rangle = \frac{\pi}{2} \omega_{\text{tr}}^2 S_\epsilon(2\omega_{\text{tr}}) \langle E \rangle \tag{9.13}$$

Again, we assume the PSD of the intensity fluctuations S_ϵ to have the above-mentioned Gaussian spectrum. The spectral density of the intensity fluctuation is inversely proportional to the spectral width:

$$S_\epsilon =\sim \frac{\epsilon_0^2}{\Delta\omega}, \tag{9.14}$$

where ϵ_0 is the root-mean-square fractional intensity fluctuation. For an order of magnitude calculation, we use $\frac{I_1}{I_2}$ as ϵ_0.

Equation (9.14) shows that the average energy increases exponentially, the time for $\langle E \rangle$ to increase by a factor of e is given by [128]:

$$T_e = \frac{1}{\pi^2 \nu_{\text{tr}}^2 S_x(2\nu_{\text{tr}})}$$

.

The maximum heating rate occurs when the spectral width of the intensity fluctuation is twice of the trap frequency, $\Delta\omega = 2\nu_{\text{tr}} \times 2\pi$. We estimate that the motional energy in the z-direction increases by a factor of e in 10^6 second. For atoms prepared close to the motional ground state, this heating rate is negligible compare to the measured value.

Die approbierte gedruckte Originalversion dieser Dissertation ist an der TU Wien Bibliothek verfügbar.
The approved original version of this doctoral thesis is available in print at TU Wien Bibliothek.
TU Bibliothek Your knowledge hub WIEN

Bibliography

[1] Silvia Bergamini, Benoît Darquié, Matthew Jones, Lionel Jacubowiez, Antoine Browaeys, and Philippe Grangier. Holographic generation of microtrap arrays for single atoms by use of a programmable phase modulator. *JOSA B*, 21(11):1889–1894, 2004.

[2] D. Meschede and A. Rauschenbeutel. Manipulating single atoms. *Advances in Atomic, Molecular, and Optical Physics*, 53:75–104, 2006.

[3] Waseem S Bakr, Jonathon I Gillen, Amy Peng, Simon Fölling, and Markus Greiner. A quantum gas microscope for detecting single atoms in a hubbard-regime optical lattice. *Nature*, 462(7269):74–77, 2009.

[4] Christof Weitenberg, Manuel Endres, Jacob F Sherson, Marc Cheneau, Peter Schauß, Takeshi Fukuhara, Immanuel Bloch, and Stefan Kuhr. Single-spin addressing in an atomic mott insulator. *Nature*, 471(7338):319–324, 2011.

[5] Lawrence W Cheuk, Matthew A Nichols, Melih Okan, Thomas Gersdorf, Vinay V Ramasesh, Waseem S Bakr, Thomas Lompe, and Martin W Zwierlein. Quantum-gas microscope for fermionic atoms. *Phys. Rev. Lett.*, 114(19):193001, 2015.

[6] Hannes Bernien, Sylvain Schwartz, Alexander Keesling, Harry Levine, Ahmed Omran, Hannes Pichler, Soonwon Choi, Alexander S Zibrov, Manuel Endres, and Markus Greiner. Probing many-body dynamics on a 51-atom quantum simulator. *Nature*, 551(7682):579, 2017.

[7] Daniel Barredo, Vincent Lienhard, Sylvain De Leseleuc, Thierry Lahaye, and Antoine Browaeys. Synthetic three-dimensional atomic structures assembled atom by atom. *Nature*, 561(7721):79–82, 2018.

[8] Philip Russell. Photonic crystal fibers. *science*, 299(5605):358–362, 2003.

[9] A Femius Koenderink, Andrea Alu, and Albert Polman. Nanophotonics: shrinking light-based technology. *Science*, 348(6234):516–521, 2015.

[10] Isabelle Staude and Jörg Schilling. Metamaterial-inspired silicon nanophotonics. *Nature Photonics*, 11(5):274, 2017.

Die approbierte gedruckte Originalversion dieser Dissertation ist an der TU Wien Bibliothek verfügbar.
The approved original version of this doctoral thesis is available in print at TU Wien Bibliothek.
TU Bibliothek Your knowledge hub WIEN

[11] E Vetsch, D Reitz, G Sagué, R Schmidt, ST Dawkins, and A Rauschenbeutel. Optical interface created by laser-cooled atoms trapped in the evanescent field surrounding an optical nanofiber. *Physical review letters*, 104(20):203603, 2010.

[12] J Lee, JA Grover, JE Hoffman, LA Orozco, and SL Rolston. Inhomogeneous broadening of optical transitions of 87rb atoms in an optical nanofiber trap. *J. Phys. B: At., Mol. and Opt. Phys.*, 48(16):165004, 2015.

[13] J. D. Thompson, T. G. Tiecke, N. P. de Leon, J. Feist, A. V. Akimov, M. Gullans, A. S. Zibrov, V. Vuletic, and M. D. Lukin. Coupling a single trapped atom to a nanoscale optical cavity. *Science*, 340(6137):1202–1205, 2013.

[14] A Goban, C-L Hung, JD Hood, S-P Yu, JA Muniz, O Painter, and HJ Kimble. Superradiance for atoms trapped along a photonic crystal waveguide. *Physical review letters*, 115(6):063601, 2015.

[15] Shinya Kato and Takao Aoki. Strong coupling between a trapped single atom and an all-fiber cavity. *Phys. Rev. Lett.*, 115(9):093603, August 2015.

[16] Kali P Nayak, Jie Wang, and Jameesh Keloth. Real-time observation of single atoms trapped and interfaced to a nanofiber cavity. *Physical Review Letters*, 123(21):213602, 2019.

[17] Andreas Reiserer and Gerhard Rempe. Cavity-based quantum networks with single atoms and optical photons. *Reviews of Modern Physics*, 87(4):1379, 2015.

[18] L-M Duan and HJ Kimble. Scalable photonic quantum computation through cavity-assisted interactions. *Physical review letters*, 92(12):127902, 2004.

[19] TG Tiecke, Jeffrey Douglas Thompson, Nathalie Pulmones de Leon, LR Liu, Vladan Vuletić, and Mikhail D Lukin. Nanophotonic quantum phase switch with a single atom. *Nature*, 508(7495):241–244, 2014.

[20] H-J Briegel, Wolfgang Dür, Juan I Cirac, and Peter Zoller. Quantum repeaters: the role of imperfect local operations in quantum communication. *Physical Review Letters*, 81(26):5932, 1998.

[21] D. E. Chang, J. S. Douglas, A. González-Tudela, C.-L. Hung, and H. J. Kimble. Colloquium: Quantum matter built from nanoscopic lattices of atoms and photons. *Rev. Mod. Phys.*, 90:031002, Aug 2018.

[22] Fam Le Kien, V. I. Balykin, and K. Hakuta. Atom trap and waveguide using a two-color evanescent light field around a subwavelength-diameter optical fiber. *Phys. Rev. A*, 70(6):063403, December 2004.

[23] D Reitz, C Sayrin, R Mitsch, P Schneeweiss, and A Rauschenbeutel. Coherence properties of nanofiber-trapped cesium atoms. *Physical review letters*, 110(24):243603, 2013.

Die approbierte gedruckte Originalversion dieser Dissertation ist an der TU Wien Bibliothek verfügbar.
The approved original version of this doctoral thesis is available in print at TU Wien Bibliothek.
TU Bibliothek Your knowledge hub WIEN

[24] Rudolf Mitsch. *Interaction and manipulation of nanofiber-trapped atoms with spin–orbit coupled light*. PhD thesis, PhD thesis. Vienna Technical University, 2014.

[25] Peter Lodahl, Sahand Mahmoodian, Søren Stobbe, Arno Rauschenbeutel, Philipp Schneeweiss, Jürgen Volz, Hannes Pichler, and Peter Zoller. Chiral quantum optics. *Nature*, 541(7638):473–480, 2017.

[26] Clément Sayrin, Christian Junge, Rudolf Mitsch, Bernhard Albrecht, Danny O'Shea, Philipp Schneeweiss, Jürgen Volz, and Arno Rauschenbeutel. Nanophotonic optical isolator controlled by the internal state of cold atoms. *Physical Review X*, 5(4):041036, 2015.

[27] Neil V Corzo, Jérémy Raskop, Aveek Chandra, Alexandra S Sheremet, Baptiste Gouraud, and Julien Laurat. Waveguide-coupled single collective excitation of atomic arrays. *Nature*, 566(7744):359, 2019.

[28] Neil V Corzo, Baptiste Gouraud, Aveek Chandra, Akihisa Goban, Alexandra S Sheremet, Dmitriy V Kupriyanov, and Julien Laurat. Large bragg reflection from one-dimensional chains of trapped atoms near a nanoscale waveguide. *Physical review letters*, 117(13):133603, 2016.

[29] HL Sørensen, J-B Béguin, KW Kluge, I Iakoupov, AS Sørensen, JH Müller, ES Polzik, and J Appel. Coherent backscattering of light off one-dimensional atomic strings. *Physical review letters*, 117(13):133604, 2016.

[30] Fam Le Kien and Arno Rauschenbeutel. Propagation of nanofiber-guided light through an array of atoms. *Physical Review A*, 90(6):063816, 2014.

[31] C. Sayrin, C. Clausen, B. Albrecht, P. Schneeweiss, and A. Rauschenbeutel. Storage of fiber-guided light in a nanofiber-trapped ensemble of cold atoms. *Optica*, 2(4):353–356, April 2015.

[32] B Gouraud, D Maxein, A Nicolas, O Morin, and J Laurat. Demonstration of a memory for tightly guided light in an optical nanofiber. *Physical review letters*, 114(18):180503, 2015.

[33] KC Kao and George A Hockham. Dielectric-fibre surface waveguides for optical frequencies. In *Proceedings of the Institution of Electrical Engineers*, volume 113, pages 1151–1158. IET, 1966.

[34] Donald Keck. A future full of light. *IEEE Journal of Selected Topics in Quantum Electronics*, 6(6):1254–1258, 2000.

[35] Ariane Stiebeiner, Ruth Garcia-Fernandez, and Arno Rauschenbeutel. Design and optimization of broadband tapered optical fibers with a nanofiber waist. *Optics express*, 18(22):22677–22685, 2010.

Die approbierte gedruckte Originalversion dieser Dissertation ist an der TU Wien Bibliothek verfügbar.
The approved original version of this doctoral thesis is available in print at TU Wien Bibliothek.
TU Bibliothek Your knowledge hub WIEN

[36] Fam Le Kien, JQ Liang, K Hakuta, and VI Balykin. Field intensity distributions and polarization orientations in a vacuum-clad subwavelength-diameter optical fiber. *Optics Communications*, 242(4-6):445–455, 2004.

[37] Fam Le Kien, VI Balykin, and K Hakuta. Angular momentum of light in an optical nanofiber. *Physical Review A*, 73(5):053823, 2006.

[38] Fam Le Kien, Philipp Schneeweiss, and Arno Rauschenbeutel. Dynamical polarizability of atoms in arbitrary light fields: general theory and application to cesium. *The European Physical Journal D*, 67(5):92, 2013.

[39] NP Stern, DJ Alton, and HJ Kimble. Simulations of atomic trajectories near a dielectric surface. *New Journal of Physics*, 13(8):085004, 2011.

[40] Stefan Scheel, Stefan Yoshi Buhmann, Christoph Clausen, and Philipp Schneeweiss. Directional spontaneous emission and lateral casimir-polder force on an atom close to a nanofiber. *Physical Review A*, 92(4):043819, 2015.

[41] Fam Le Kien, Philipp Schneeweiss, and Arno Rauschenbeutel. State-dependent potentials in a nanofiber-based two-color trap for cold atoms. *Physical Review A*, 88(3):033840, 2013.

[42] Poul S Jessen, C Gerz, Paul D Lett, William D Phillips, SL Rolston, RJC Spreeuw, and CI Westbrook. Observation of quantized motion of rb atoms in an optical field. *Physical review letters*, 69(1):49, 1992.

[43] JI Cirac, R Blatt, AS Parkins, and P Zoller. Spectrum of resonance fluorescence from a single trapped ion. *Physical Review A*, 48(3):2169, 1993.

[44] Markus Lindberg. Resonance fluorescence of a laser-cooled trapped ion in the lamb-dicke limit. *Physical Review A*, 34(4):3178, 1986.

[45] PS Jessen. *An investigation ofthe microscopic motion ofatoms in optical molasses using optical heterodyne spectroscopy ofresonance fluorescence*. PhD thesis, (University of Âarhus, Danemark, 1993).

[46] Claude Cohen-Tannoudji, Jacques Dupont-Roc, and Gilbert Grynberg. *Atom-photon interactions: basic processes and applications*. 1998.

[47] Serge Haroche and J-M Raimond. *Exploring the quantum: atoms, cavities, and photons*. Oxford university press, 2006.

[48] Daniel A Steck. Quantum and atom optics, 2007.

[49] J Robert Johansson, Paul D Nation, and Franco Nori. Qutip 2: A python framework for the dynamics of open quantum systems. *Computer Physics Communications*, 184(4):1234–1240, 2013.

Die approbierte gedruckte Originalversion dieser Dissertation ist an der TU Wien Bibliothek verfügbar.
The approved original version of this doctoral thesis is available in print at TU Wien Bibliothek.
TU Bibliothek Your knowledge hub WIEN

[50] Peter Kirton. (private communication).

[51] Daniel A Steck. Cesium d line data, 2003.

[52] Manoj Das, A Shirasaki, KP Nayak, M Morinaga, Fam Le Kien, and K Hakuta. Measurement of fluorescence emission spectrum of few strongly driven atoms using an optical nanofiber. *Optics express*, 18(16):17154–17164, 2010.

[53] William D Phillips. Nobel lecture: Laser cooling and trapping of neutral atoms. *Reviews of Modern Physics*, 70(3):721, 1998.

[54] Wolfgang Ketterle. Nobel lecture: When atoms behave as waves: Bose-einstein condensation and the atom laser. *Reviews of Modern Physics*, 74(4):1131, 2002.

[55] Christian Gross and Immanuel Bloch. Quantum simulations with ultracold atoms in optical lattices. *Science*, 357(6355):995–1001, 2017.

[56] Xibo Zhang and Jun Ye. Precision measurement and frequency metrology with ultracold atoms. *National Science Review*, 3(2):189–200, 2016.

[57] Daniel Hümmer, Philipp Schneeweiss, Arno Rauschenbeutel, and Oriol Romero-Isart. Heating in nanophotonic traps for cold atoms. *Physical Review X*, 9(4):041034, 2019.

[58] B. Albrecht, Y. Meng, C. Clausen, A. Dareau, P. Schneeweiss, and A. Rauschenbeutel. Fictitious magnetic-field gradients in optical microtraps as an experimental tool for interrogating and manipulating cold atoms. *Physical Review A*, 94(6):061401, December 2016.

[59] Christoffer Østfeldt, Jean-Baptiste S Béguin, Freja T Pedersen, Eugene S Polzik, Jörg H Müller, and Jürgen Appel. Dipole force free optical control and cooling of nanofiber trapped atoms. *Optics Letters*, 42(21):4315–4318, 2017.

[60] Y Meng, A Dareau, P Schneeweiss, and A Rauschenbeutel. Near-ground-state cooling of atoms optically trapped 300 nm away from a hot surface. *Physical Review X*, 8(3):031054, 2018.

[61] Hyun-Gue Hong, Wontaek Seo, Moonjoo Lee, Wonshik Choi, Jai-Hyung Lee, and Kyungwon An. Spectral line-shape measurement of an extremely weak amplitude-fluctuating light source by photon-counting-based second-order correlation spectroscopy. *Optics letters*, 31(21):3182–3184, 2006.

[62] Ch Monroe, DM Meekhof, BE King, Steven R Jefferts, Wayne M Itano, David J Wineland, and P Gould. Resolved-sideband raman cooling of a bound atom to the 3d zero-point energy. *Physical review letters*, 75(22):4011, 1995.

[63] Xiaodong Qi, Ben Q Baragiola, Poul S Jessen, and Ivan H Deutsch. Dispersive response of atoms trapped near the surface of an optical nanofiber with applications to quantum nondemolition measurement and spin squeezing. *Physical Review A*, 93(2):023817, 2016.

Die approbierte gedruckte Originalversion dieser Dissertation ist an der TU Wien Bibliothek verfügbar.
The approved original version of this doctoral thesis is available in print at TU Wien Bibliothek.
TU Bibliothek Your knowledge hub WIEN

[64] Sergey Sukhov, Veerachart Kajorndejnukul, Roxana Rezvani Naraghi, and Aristide Dogariu. Dynamic consequences of optical spin–orbit interaction. *Nature Photonics*, 9(12):809–812, 2015.

[65] Francisco J Rodríguez-Fortuño, Nader Engheta, Alejandro Martínez, and Anatoly V Zayats. Lateral forces on circularly polarizable particles near a surface. *Nature communications*, 6, 2015.

[66] Farid Kalhor, Thomas Thundat, and Zubin Jacob. Universal spin-momentum locked optical forces. *Applied Physics Letters*, 108(6):061102, 2016.

[67] Francesco Intravaia, Vanik E Mkrtchian, Stefan Yoshi Buhmann, Stefan Scheel, Diego AR Dalvit, and Carsten Henkel. Friction forces on atoms after acceleration. *Journal of Physics: Condensed Matter*, 27(21):214020, 2015.

[68] Aji A Anappara, Simone De Liberato, Alessandro Tredicucci, Cristiano Ciuti, Giorgio Biasiol, Lucia Sorba, and Fabio Beltram. Signatures of the ultrastrong light-matter coupling regime. *Physical Review B*, 79(20):201303, 2009.

[69] G Günter, Aji A Anappara, J Hees, Alexander Sell, Giorgio Biasiol, Lucia Sorba, S De Liberato, Cristiano Ciuti, Alessandro Tredicucci, Alfred Leitenstorfer, et al. Sub-cycle switch-on of ultrastrong light–matter interaction. *Nature*, 458(7235):178–181, 2009.

[70] Thomas Niemczyk, F Deppe, H Huebl, EP Menzel, F Hocke, MJ Schwarz, JJ Garcia-Ripoll, D Zueco, T Hümmer, E Solano, et al. Circuit quantum electrodynamics in the ultrastrong-coupling regime. *Nature Physics*, 6(10):772–776, 2010.

[71] Pol Forn-Díaz, Jürgen Lisenfeld, David Marcos, Juan José Garcia-Ripoll, Enrique Solano, CJPM Harmans, and JE Mooij. Observation of the bloch-siegert shift in a qubit-oscillator system in the ultrastrong coupling regime. *Physical review letters*, 105(23):237001, 2010.

[72] Daniel Z Rossatto, Celso J Villas-Bôas, Mikel Sanz, and Enrique Solano. Spectral classification of coupling regimes in the quantum rabi model. *Physical Review A*, 96(1):013849, 2017.

[73] P Forn-Díaz, J José García-Ripoll, Borja Peropadre, J-L Orgiazzi, MA Yurtalan, R Belyansky, Christopher M Wilson, and A Lupascu. Ultrastrong coupling of a single artificial atom to an electromagnetic continuum in the nonperturbative regime. *Nature Physics*, 13(1):39–43, 2017.

[74] Fumiki Yoshihara, Tomoko Fuse, Sahel Ashhab, Kosuke Kakuyanagi, Shiro Saito, and Kouichi Semba. Superconducting qubit–oscillator circuit beyond the ultrastrong-coupling regime. *Nature Physics*, 13(1):44–47, 2017.

[75] Andreas Bayer, Marcel Pozimski, Simon Schambeck, Dieter Schuh, Rupert Huber, Dominique Bougeard, and Christoph Lange. Terahertz light–matter interaction beyond unity coupling strength. *Nano letters*, 17(10):6340–6344, 2017.

Die approbierte gedruckte Originalversion dieser Dissertation ist an der TU Wien Bibliothek verfügbar.
The approved original version of this doctoral thesis is available in print at TU Wien Bibliothek.
TU Bibliothek Your knowledge hub WIEN

[76] Anton Frisk Kockum, Adam Miranowicz, Simone De Liberato, Salvatore Savasta, and Franco Nori. Ultrastrong coupling between light and matter. *Nature Reviews Physics*, 1(1):19–40, 2019.

[77] Pierre Nataf and Cristiano Ciuti. Protected quantum computation with multiple resonators in ultrastrong coupling circuit qed. *Physical review letters*, 107(19):190402, 2011.

[78] G Romero, D Ballester, YM Wang, V Scarani, and E Solano. Ultrafast quantum gates in circuit qed. *Physical Review Letters*, 108(12):120501, 2012.

[79] Thi Ha Kyaw, Simone Felicetti, Guillermo Romero, Enrique Solano, and L-C Kwek. Scalable quantum memory in the ultrastrong coupling regime. *Scientific reports*, 5(1):1–5, 2015.

[80] Klaus Hepp and Elliott H Lieb. On the superradiant phase transition for molecules in a quantized radiation field: the dicke maser model. *Annals of Physics*, 76(2):360–404, 1973.

[81] Yo K Wang and FT Hioe. Phase transition in the dicke model of superradiance. *Physical Review A*, 7(3):831, 1973.

[82] Clive Emary and Tobias Brandes. Chaos and the quantum phase transition in the dicke model. *Physical Review E*, 67(6):066203, 2003.

[83] D Ballester, Guillermo Romero, Juan José García-Ripoll, F Deppe, and Enrique Solano. Quantum simulation of the ultrastrong-coupling dynamics in circuit quantum electrodynamics. *Physical Review X*, 2(2):021007, 2012.

[84] JS Pedernales, I Lizuain, S Felicetti, G Romero, L Lamata, and E Solano. Quantum rabi model with trapped ions. *Scientific reports*, 5(1):1–7, 2015.

[85] Jochen Braumüller, Michael Marthaler, Andre Schneider, Alexander Stehli, Hannes Rotzinger, Martin Weides, and Alexey V Ustinov. Analog quantum simulation of the rabi model in the ultra-strong coupling regime. *Nature communications*, 8(1):1–8, 2017.

[86] NK Langford, R Sagastizabal, M Kounalakis, C Dickel, A Bruno, F Luthi, DJ Thoen, A Endo, and L DiCarlo. Experimentally simulating the dynamics of quantum light and matter at deep-strong coupling. *Nature communications*, 8(1):1–10, 2017.

[87] Dingshun Lv, Shuoming An, Zhenyu Liu, Jing-Ning Zhang, Julen S Pedernales, Lucas Lamata, Enrique Solano, and Kihwan Kim. Quantum simulation of the quantum rabi model in a trapped ion. *Physical Review X*, 8(2):021027, 2018.

[88] P Schneeweiss, A Dareau, and C Sayrin. Cold-atom-based implementation of the quantum rabi model. *Physical Review A*, 98(2):021801, 2018.

[89] A Dareau, Y Meng, P Schneeweiss, and A Rauschenbeutel. Observation of ultrastrong spin-motion coupling for cold atoms in optical microtraps. *Physical review letters*, 121(25):253603, 2018.

Die approbierte gedruckte Originalversion dieser Dissertation ist an der TU Wien Bibliothek verfügbar.
The approved original version of this doctoral thesis is available in print at TU Wien Bibliothek.
TU Bibliothek Your knowledge hub WIEN

[90] II Rabi. On the process of space quantization. *Physical Review*, 49(4):324, 1936.

[91] Robert H Dicke. Coherence in spontaneous radiation processes. *Physical review*, 93(1):99, 1954.

[92] Y. Meng, A. Dareau, P. Schneeweiss, and A. Rauschenbeutel. Near-Ground-State Cooling of Atoms Optically Trapped 300 nm Away from a Hot Surface. *Physical Review X*, 8(3):031054, September 2018.

[93] Immanuel Bloch. Ultracold quantum gases in optical lattices. *Nature physics*, 1(1):23–30, 2005.

[94] Adam M Kaufman, Brian J Lester, and Cindy A Regal. Cooling a single atom in an optical tweezer to its quantum ground state. *Physical Review X*, 2(4):041014, 2012.

[95] Jeffrey Douglas Thompson, TG Tiecke, Alexander S Zibrov, V Vuletić, and Mikhail D Lukin. Coherence and raman sideband cooling of a single atom in an optical tweezer. *Physical Review Letters*, 110(13):133001, 2013.

[96] M Morinaga, I Bouchoule, J-C Karam, and C Salomon. Manipulation of motional quantum states of neutral atoms. *Physical review letters*, 83(20):4037, 1999.

[97] Noomen Belmechri, Leonid Förster, Wolfgang Alt, Artur Widera, Dieter Meschede, and Andrea Alberti. Microwave control of atomic motional states in a spin-dependent optical lattice. *Journal of Physics B: Atomic, Molecular and Optical Physics*, 46(10):104006, 2013.

[98] Frank Vewinger, Manfred Heinz, Ruth Garcia Fernandez, Nikolay V Vitanov, and Klaas Bergmann. Creation and measurement of a coherent superposition of quantum states. *Physical review letters*, 91(21):213001, 2003.

[99] A Smith, CA Riofrío, BE Anderson, H Sosa-Martinez, IH Deutsch, and Poul S Jessen. Quantum state tomography by continuous measurement and compressed sensing. *Physical Review A*, 87(3):030102, 2013.

[100] Simone De Liberato, Cristiano Ciuti, and Iacopo Carusotto. Quantum vacuum radiation spectra from a semiconductor microcavity with a time-modulated vacuum rabi frequency. *Physical review letters*, 98(10):103602, 2007.

[101] Félix Beaudoin, Jay M Gambetta, and A Blais. Dissipation and ultrastrong coupling in circuit qed. *Physical Review A*, 84(4):043832, 2011.

[102] Peter Kirton, Mor M Roses, Jonathan Keeling, and Emanuele G Dalla Torre. Introduction to the dicke model: From equilibrium to nonequilibrium, and vice versa (adv. quantum technol. 1-2/2019). *Advanced Quantum Technologies*, 2(1-2):1970013, 2019.

[103] R Mitsch, C Sayrin, B Albrecht, P Schneeweiss, and A Rauschenbeutel. Exploiting the local polarization of strongly confined light for sub-micrometer-resolution internal state preparation and manipulation of cold atoms. *Physical Review A*, 89(6):063829, 2014.

Die approbierte gedruckte Originalversion dieser Dissertation ist an der TU Wien Bibliothek verfügbar.
The approved original version of this doctoral thesis is available in print at TU Wien Bibliothek.
TU Bibliothek Your knowledge hub WIEN

[104] Silvia Bergamini, Benoît Darquié, Matthew Jones, Lionel Jacubowiez, Antoine Browaeys, and Philippe Grangier. Holographic generation of microtrap arrays for single atoms by use of a programmable phase modulator. *JOSA B*, 21(11):1889–1894, 2004.

[105] Dieter Meschede and Arno Rauschenbeutel. Manipulating single atoms. *Advances in Atomic, Molecular, and Optical Physics*, 53:75–104, 2006.

[106] Waseem S Bakr, Jonathon I Gillen, Amy Peng, Simon Fölling, and Markus Greiner. A quantum gas microscope for detecting single atoms in a hubbard-regime optical lattice. *Nature*, 462(7269):74–77, 2009.

[107] Christof Weitenberg, Manuel Endres, Jacob F Sherson, Marc Cheneau, Peter Schauß, Takeshi Fukuhara, Immanuel Bloch, and Stefan Kuhr. Single-spin addressing in an atomic mott insulator. *Nature*, 471(7338):319–324, 2011.

[108] Hannes Bernien, Sylvain Schwartz, Alexander Keesling, Harry Levine, Ahmed Omran, Hannes Pichler, Soonwon Choi, Alexander S Zibrov, Manuel Endres, Markus Greiner, et al. Probing many-body dynamics on a 51-atom quantum simulator. *Nature*, 551(7682):579, 2017.

[109] Daniel Barredo, Vincent Lienhard, Sylvain De Leseleuc, Thierry Lahaye, and Antoine Browaeys. Synthetic three-dimensional atomic structures assembled atom by atom. *Nature*, 561(7721):79–82, 2018.

[110] May E Kim, Tzu-Han Chang, Brian M Fields, Cheng-An Chen, and Chen-Lung Hung. Trapping single atoms on a nanophotonic circuit with configurable tweezer lattices. *Nature communications*, 10(1):1647, 2019.

[111] Yijian Meng, Christian Liedl, Sebastian Pucher, Arno Rauschenbeutel, and Philipp Schneeweiss. Imaging and localizing individual atoms interfaced with a nanophotonic waveguide. *Physical Review Letters*, 125(5):053603, 2020.

[112] Wolfgang Alt. An objective lens for efficient fluorescence detection of single atoms. *Optik*, 113(3):142–144, 2002.

[113] Andrea Alberti, Carsten Robens, Wolfgang Alt, Stefan Brakhane, Michał Karski, René Reimann, Artur Widera, and Dieter Meschede. Super-resolution microscopy of single atoms in optical lattices. *New Journal of Physics*, 18(5):053010, 2016.

[114] R Mitsch, C Sayrin, B Albrecht, P Schneeweiss, and A Rauschenbeutel. Quantum state-controlled directional spontaneous emission of photons into a nanophotonic waveguide. *Nature communications*, 5(1):1–5, 2014.

[115] Carsten Robens, Stefan Brakhane, Wolfgang Alt, Felix Kleißler, Dieter Meschede, Geol Moon, Gautam Ramola, and Andrea Alberti. High numerical aperture (na= 0.92) objective lens for imaging and addressing of cold atoms. *Optics letters*, 42(6):1043–1046, 2017.

Die approbierte gedruckte Originalversion dieser Dissertation ist an der TU Wien Bibliothek verfügbar.
The approved original version of this doctoral thesis is available in print at TU Wien Bibliothek.
TU Bibliothek Your knowledge hub WIEN

[116] G Sagué, A Baade, and A Rauschenbeutel. Blue-detuned evanescent field surface traps for neutral atoms based on mode interference in ultrathin optical fibres. *New Journal of Physics*, 10(11):113008, 2008.

[117] Tomás Ramos, Hannes Pichler, Andrew J. Daley, and Peter Zoller. Quantum spin dimers from chiral dissipation in cold-atom chains. *Phys. Rev. Lett.*, 113:237203, Dec 2014.

[118] A. González-Tudela, V. Paulisch, D. E. Chang, H. J. Kimble, and J. I. Cirac. Deterministic generation of arbitrary photonic states assisted by dissipation. *Phys. Rev. Lett.*, 115:163603, Oct 2015.

[119] Ephraim Shahmoon, Pjotrs Grišins, Hans Peter Stimming, Igor Mazets, and Gershon Kurizki. Highly nonlocal optical nonlinearities in atoms trapped near a waveguide. *Optica*, 3(7):725–733, 2016.

[120] D. E. Chang, J. S. Douglas, A. González-Tudela, C.-L. Hung, and H. J. Kimble. Colloquium: Quantum matter built from nanoscopic lattices of atoms and photons. *Rev. Mod. Phys.*, 90(3):031002, August 2018.

[121] D. E. Chang, J. I. Cirac, and H. J. Kimble. Self-organization of atoms along a nanophotonic waveguide. *Phys. Rev. Lett.*, 110:113606, Mar 2013.

[122] Tobias Grießer and Helmut Ritsch. Light-induced crystallization of cold atoms in a 1d optical trap. *Phys. Rev. Lett.*, 111:055702, Aug 2013.

[123] Daniela Holzmann, Matthias Sonnleitner, and Helmut Ritsch. Self-ordering and collective dynamics of transversely illuminated point-scatterers in a 1d trap. *The European Physical Journal D*, 68(11):1–11, 2014.

[124] Zachary Eldredge, Pablo Solano, Darrick Chang, and Alexey V Gorshkov. Self-organization of atoms coupled to a chiral reservoir. *Physical Review A*, 94(5):053855, 2016.

[125] Akihisa Goban. *Strong atom-light interactions along nanostructures: Transition from free-space to nanophotonic interfaces*. PhD thesis, 2015.

[126] Baptiste Gouraud. *Optical Nanofibers Interfacing Cold Atoms-A Tool for Quantum Optics*. PhD thesis, 2016.

[127] Carsten Henkel, Sierk Pötting, and Martin Wilkens. Loss and heating of particles in small and noisy traps. *Applied Physics B*, 69(5-6):379–387, 1999.

[128] T. A. Savard, K. M. O'Hara, and J. E. Thomas. Laser-noise-induced heating in far-off resonance optical traps. *Physical Review A*, 56(2):R1095–R1098, August 1997.

[129] Christian Wuttke. *Thermal excitations of optical nanofibers measured with a cavity*. PhD thesis, Ph. D. thesis, University of Mainz, 2014.

Die approbierte gedruckte Originalversion dieser Dissertation ist an der TU Wien Bibliothek verfügbar.
The approved original version of this doctoral thesis is available in print at TU Wien Bibliothek.
TU Bibliothek Your knowledge hub WIEN

[130] Omar Florez, Paulo F Jarschel, Yovanny AV Espinel, CMB Cordeiro, TP Mayer Alegre, Gustavo S Wiederhecker, and Paulo Dainese. Brillouin scattering self-cancellation. *Nature communications*, 7(1):1–8, 2016.

[131] Jean-Charles Beugnot, Sylvie Lebrun, Gilles Pauliat, Hervé Maillotte, Vincent Laude, and Thibaut Sylvestre. Brillouin light scattering from surface acoustic waves in a subwavelength-diameter optical fibre. *Nature communications*, 5(1):1–6, 2014.

Die approbierte gedruckte Originalversion dieser Dissertation ist an der TU Wien Bibliothek verfügbar.
The approved original version of this doctoral thesis is available in print at TU Wien Bibliothek.

Die approbierte gedruckte Originalversion dieser Dissertation ist an der TU Wien Bibliothek verfügbar.
The approved original version of this doctoral thesis is available in print at TU Wien Bibliothek.

Acknowledgements

Research in experimental physics is a highly collaborative process. I have been very fortunate to work in the nanofiber group during my doctoral study. To start, I would like to express my gratitude toward my supervisor Prof. Arno Rauschenbeutel for accepting me into this wonderful group, for his support and physics insights. It's a gift to have a group leader who can tackle seemingly difficult problems with elegant and often practical solutions.

I would like to thank Dr. Philipp Schneeweiss, who has been the leader and the driving force of the cold-atoms subgroup. Throughout my study, he has always been a positive presence, and his enthusiasm has made the day-to-day work a pleasant experience even during the more difficult times. I would also like to thank him for his feedback during the revision of this thesis.

I would like to thank my first lab mate Bernhard Albrecht. He has helped me to ease into the new group and introduced me to the ins and outs of the experimental setup. I would like to offer my special thanks to Dr. Alexandre Dareau with whom I spent the most time in the cold-atoms subgroup. His analysis and experience have been instrumental in many research projects. I am always impressed with his textbook-like research reports which are produced at the speed of an unladen swallow. Outside of research, his photoshop skills and football knowledge are also highly appreciated. I would like to thank Dr. Christoph Clausen, who could always offer great advice and a calming presence in the lab. I would like to extend my thanks to Sebastian Pucher and Christian Liedl for the fruitful collaboration in the last year. It has been a pleasure working with them.

I would like to thank Dr. Jürgen Volz, Dr. Michael Scheucher, Yuri Minoguchi, and Dr. Peter Kirton for the many stimulating discussions in research. I am thankful to my second thesis supervisor Prof. Peter Rabl for his encouragement and advice. I would like to thank the group of Prof. Jeff Thompson for the invaluable experience during my secondment at Princeton. I also wish to thank CoQuS for many great memories, and for the opportunities to meet amazing people both in research and personal life.

Finally, I would like to express my deepest gratitude to my family for their support.

Die approbierte gedruckte Originalversion dieser Dissertation ist an der TU Wien Bibliothek verfügbar.
The approved original version of this doctoral thesis is available in print at TU Wien Bibliothek.
TU Bibliothek Your knowledge hub WIEN

Die approbierte gedruckte Originalversion dieser Dissertation ist an der TU Wien Bibliothek verfügbar.
The approved original version of this doctoral thesis is available in print at TU Wien Bibliothek.

LEBENSLAUF

Yijian Meng

Persönliche Daten

Geburtsdatum:	2. Juli 1990
Geburtsort:	Peking
Staatsangehörigkeit:	Kanadisch

Ausbildung

seit 9/2015	Technische Universität Wien Doktorand in Technischer Physik
10/2012 – 03/2015	University of Ottawa Master of Science in Physics
09/2008 – 09/2012	University of Toronto Engineering Science with Physics Option
08/2006 – 06/2008	Waterloo Collegiate Institution (Gymnasium)

Die approbierte gedruckte Originalversion dieser Dissertation ist an der TU Wien Bibliothek verfügbar.
The approved original version of this doctoral thesis is available in print at TU Wien Bibliothek.